Max-Planck-Institut für Metallforschung
Stuttgart

Thermal Fatigue of Cu Thin Films

Reiner Mönig

Dissertation
an der
Universität Stuttgart

Bericht Nr. 159
Januar 2005

Thermal Fatigue of Cu Thin Films

Von der Fakultät Chemie der Universität Stuttgart
zur Erlangung der Würde eines Doktors der Naturwissenschaften
(Dr. rer. nat.) genehmigte Abhandlung

vorgelegt von

Reiner Mönig

aus Bruchsal

Hauptberichter: Prof. Dr. phil. E. Arzt
Mitberichter: Prof. Dr. rer. nat. O. Kraft
Tag der mündlichen Prüfung: 18. Juni 2004

Max-Planck-Institut für Metallforschung und
Institut für Metallkunde der Universität Stuttgart

2004

Reiner Mönig

Thermal Fatigue of Thin Copper Films

118 pages, 59 figures, 1 table

Abstract

Fatigue is a process in which materials are damaged by the effect of cyclic mechanical loads. This phenomenon has been extensively studied in bulk metals, but up to now only little is known about fatigue of metals with small length scales. In this work the behaviour of small Cu structures under alternating thermal and mechanical loads has been investigated. It was found that the small structures exhibited different fatigue damage evolution mechanisms and were far more resistant to failure than bulk materials. Structures with a thickness of 300 nm developed regions of severe surface damage that were similar in some respects to the damage formed in bulk metals. Just as in bulk metals, the damage was caused by dislocation activity. However, a number of new damage processes were observed in the 300 nm thick structures, including twin dissolution, and facetted grain growth. The strong dependence of this new damage on grain orientation revealed that the detailed dislocation interactions and reaction products play a crucial role in damage formation. The structures with a thickness of 100 nm exhibited a completely different damage morphology, in that the damage appeared to be formed by extensive surface and boundary diffusion rather than by dislocation activity. This is believed to be the result of the suppression of dislocation activity at small length scales. The 100 nm thick structures also exhibited longer fatigue lives than the 300 nm thick structures, and both were more reliable than fine-grained and large-grained bulk Cu. The enhanced reliability is partly due to larger yield stresses in the thin films, but is also due to a second size effect in the mechanical behaviour, namely that thin films can accommodate higher plastic strains before failure.

Max-Planck-Institut für Metallforschung und Institut für Metallkunde der Universität Stuttgart, 2004

Reiner Mönig

Thermomechanische Ermüdung von dünnen Kupferschichten

118 Seiten, 59 Abbildungen, eine Tabelle

Kurzzusammenfassung

Die mechanische Ermüdung ist ein Prozess, bei dem Werkstoffe durch die Einwirkung wechselnder mechanischer Belastungen geschädigt werden. Ermüdung wurde in der Vergangenheit intensiv an Massivmaterialien untersucht, jedoch bis heute ist nur wenig bekannt über die Ermüdung von Mikromaterialien. In der vorliegenden Arbeit wurde das Verhalten von kleinen Cu Strukturen unter wechselnder thermischer und mechanischer Belastung untersucht. Dabei zeigte sich, dass in kleinen Materialien andere Schädigungsmechanismen als in Massivmaterialien auftreten, und dass diese Materialien weitaus widerstandsfähiger gegenüber mechanischer Ermüdung sind. In Teststrukturen mit Schichtdicken von 300 nm wurden Veränderungen der Oberfläche gefunden, die wahrscheinlich auf Versetzungsaktivität zurückzuführen sind. Neben einigen von Massivproben bekannten Phänomenen konnten auch neue Schädigungsprozesse identifiziert werden. So wurde beispielsweise die Auflösung von Zwillingen und ein facettiertes Kornwachstum beobachtet. Die starke Abhängigkeit dieser neuartigen Schädigung von der Kornorientierung weist darauf hin, dass Versetzungswechselwirkung und die entstehenden Reaktionsprodukte eine entscheidende Rolle für die Schadensbildung einnehmen. Strukturen mit einer Dicke von 100 nm wiesen ein gegenüber dickeren Filmen ein unterschiedliches Schädigungsverhalten auf. Die Schädigung dieser Filme beruht anscheinend auf Oberflächen- und Korngrenzdiffusion und nicht wie die der dickeren Filme auf Versetzungsaktivität. Dies ist möglicherweise ein Ergebnis der Unterdrückung der Versetzungsaktivität in kleinen Abmessungen. Im Vergleich zu 300 nm dicken Proben wiesen Proben mit 100 nm Dicke, vermutlich durch den anderen Schädigungsmechanismus, deutlich höhere Lebensdauern auf. Die gegenüber Massivmaterial erhöhte Lebensdauer beider Filmdicken liegt einerseits an der höheren Festigkeit der dünnen Filme, aber auch daran, dass dünne Filme höhere kumulative plastische Dehnungen aufnehmen können.

Danksagung

Die vorliegende Doktorarbeit wurde zwischen April 2000 und Januar 2004 am Max-Planck-Institut für Metallforschung in Stuttgart angefertigt. Den Personen, die für den Fortgang dieser Arbeit von besonderer Bedeutung waren möchte ich hier danken:

Herrn Prof. Dr. E. Arzt für die Aufnahme in seine Abteilung, sein Interesse an der Arbeit, viele wichtige und hilfreiche Ideen sowie die Übernahme des Hauptberichts.

Herrn Prof. Dr. O. Kraft für das von seinen Arbeiten ausgelöste Interesse an der Ermüdung dünner Schichten, seine Unterstützung der Arbeit und die Übernahme des Mitberichts.

Frau Dr. C.A. Volkert für die fördernde Unterstützung, viele wichtige Anregungen und Vorschläge sowie Hilfen bei der Verbesserung meiner englischen Sprache.

Herrn Dr. R.R. Keller für die gute Zusammenarbeit bei der Suche nach einer Erklärung für die in Aluminiumproben beobachtete Schädigung, die den Anstoß zu dieser Arbeit gegeben hat. Außerdem für die Einladung zum National Institute of Standards and Technology nach Boulder/USA.

Herrn Prof. Dr. G.P. Zhang für viele Gespräche und Informationen zum Thema Ermüdung und die Untersuchung von Proben im Transmissionselektronenmikroskop.

Herrn Prof. Dr. Y.B. Park für die gute Zusammenarbeit bei der Anwendung der in dieser Arbeit beschriebenen Methode bei höheren Frequenzen und für die Beobachtung einer Frequenzabhängigkeit der Schädigung.

Herrn S. Orso für die gute Zusammenarbeit bei der Messung von Lebensdauern und der Entdeckung von rechteckigen Körner.

Allen Mitgliedern der Abteilung Arzt für die angenehme und kooperative Arbeitsatmosphäre.

Contents

1 Introduction

Thin metal films and metal structures are important components in modern microtechnology. Highly integrated microelectronic (ME) circuits as well as micro-electro-mechanical systems (MEMS) make use of metal lines and structures with dimensions on the micrometer and submicrometer scale. Today's complex microelectronic devices contain a large number of such submicrometer metal lines that can have combined lengths of many kilometers. Therefore the reliability of these metal structures is of utmost importance for the reliability of the whole electronic device. The performance of the metal films and lines is strongly affected by mechanical stresses. Stresses are inherent in composite structures and are already present in microelectronic devices during fabrication due to differences in the coefficients of thermal expansion. For example, in a thin Cu film that is attached to a thick Si wafer, a temperature change of only 30 K leads to a stress change of 100 MPa. Bulk metals typically cannot withstand such high stresses, but thin films of the same metals can. It has been discovered that for static or monotonic loads, the yield strength of small metal structures is many times higher than the yield strength of their bulk counterparts. However during the life of a ME or MEMS device, temperature variations and stress variations occur repeatedly and the structures experience cyclic loading rather than monotonic loading. Therefore results obtained from investigations using fatigue loading are necessary for describing the reliability of the metal structures in these devices.

Fatigue is a phenomenon in which cyclic loads far below the yield strength of a material lead to damage formation and failure. Fatigue was discovered in the first half of the 19^{th} century and since then has been extensively investigated in bulk metals. The pure metal that has received the most attention in these studies is Cu. During fatigue of Cu, periodic dislocation structures form with characteristic spacings of about one micrometer. These dislocation structures are believed to control the evolution of damage and eventual failure of the components. Today it is still not clear how components with dimensions smaller than these characteristic spacings respond to cyclic loads. A few fatigue studies have recently been performed on fine-grained metals and on thin films. These observations indicate that some of the small scale metal samples, in particular the thin films, are more reliable than coarse-grained bulk metals under fatigue conditions. This may be associated with the well known increased strength of thin films, or it may be due to differences in the mechanism for plastic

strain accumulation in small dimensions. To gain a fundamental understanding of fatigue, including how plastic strains are accumulated in small scale structures, detailed observations of the fatigue process are necessary. For technological reasons it is also important to clarify the reliability of these small scale structures.

In this work a new method has been developed that allows high cycle thermal fatigue experiments on small metal structures and the simultaneous observation of fatigue damage in a scanning electron microscope. Chapter 2 briefly introduces fatigue in bulk metals and stresses in thin films, and summarizes the extant literature on fatigue of fine-grained and thin film metals. The main observations and conclusions of the work performed here are detailed in Chapters 3, 4, and 5. Chapter 3 describes the method that has been used and presents some proof-of-concept results. Chapter 4 addresses the microscopic fatigue damage evolution in thin Cu films. Some completely new fatigue damage mechanisms are observed which are explained with a model involving dislocation interaction with twin and grain boundaries. Chapter 5 concentrates on the observed influence of film thickness and grain size on damage morphology and the number of cycles to failure. The enhancement of fatigue life relative to bulk samples and with decreasing film thickness is discussed in terms of increased yield strength as well as a new size effect in small dimensions, namely that the thin films can accommodate higher plastic strains before failure.

2 Background

Small metal structures such as thin films are used as components of highly integrated microelectronic circuits and micro-electro-mechanical systems. In these applications, the metals often experience severe cyclic mechanical and thermomechanical loads and fatigue has been identified as an important factor influencing their reliability [Philofsky et al. 1971, Subramanian et al. 2001, Keller et al. 2002, Huang et al. 2002]. Besides technological reasons for the investigation of fatigue in small metal structures, there are also fundamental materials science issues. For instance, it has been observed that the mechanical behaviour of metals with dimensions on the micrometer scale differs significantly from bulk metals and it is still not clear to what extent and how fatigue proceeds in such small structures.

The first two sections of this chapter provide brief summaries of fatigue in bulk metals and of the mechanical properties of metals with small length scales, such as ultra-fine-grained material and thin films. More details on these subjects can be found in the literature [Klesnil and Lukáš 1980, Basinski and Basinski 1992, Arzt 1998, Suresh 1998, Baker 2001]. The third section contains an overview of the existing literature in the field of fatigue of fine-grained metals and thin films. In the fourth and final section, the current understanding of fatigue in small scale structures is summarized and used to motivate the work presented in this thesis.

2.1 Fatigue of Ductile Bulk Metals

Fatigue of metals is a complicated process which today is still not fully understood. It involves the motion and interaction of dislocations, formation of surface extrusions, crack nucleation, and crack growth which causes the eventual failure of the component. The loads that are needed to instigate fatigue failure can be far below the ones that cause failure in monotonic tests.

In the early stages of fatigue, cyclic plastic straining causes dislocation motion and interaction which leads to the formation of stable dislocation structures. These structures can be divided into different types, depending on the number of active slip systems, the plastic strain amplitude, and the ease of cross-slip in the sample material. A semi-quantitative diagram of the expected dislocation structures as a function of stacking fault energy (measure of ease of cross slip) and plastic strain range is given in Fig. 2.1(a). In an easy cross-slip

material such as Cu oriented for single slip, there are three types of dislocation structures depending on the strain amplitude. For plastic strain amplitudes below 10^{-4}, the stable dislocation structure is the vein structure. It consists of bunches of dislocation dipoles on the active glide plane with dislocation free regions in between. According to the literature, this structure leads to hardening of the crystal and the distance between the veins shrinks with increasing cumulative plastic strain [Basinski and Basinski 1992]. On increasing the strain amplitude, the material reacts with an increase in the stress amplitude. This is illustrated by region A in the cyclic stress-strain curve in Fig. 2.1(b). Such a plot shows the stable or saturated stress amplitude for a given plastic strain amplitude.

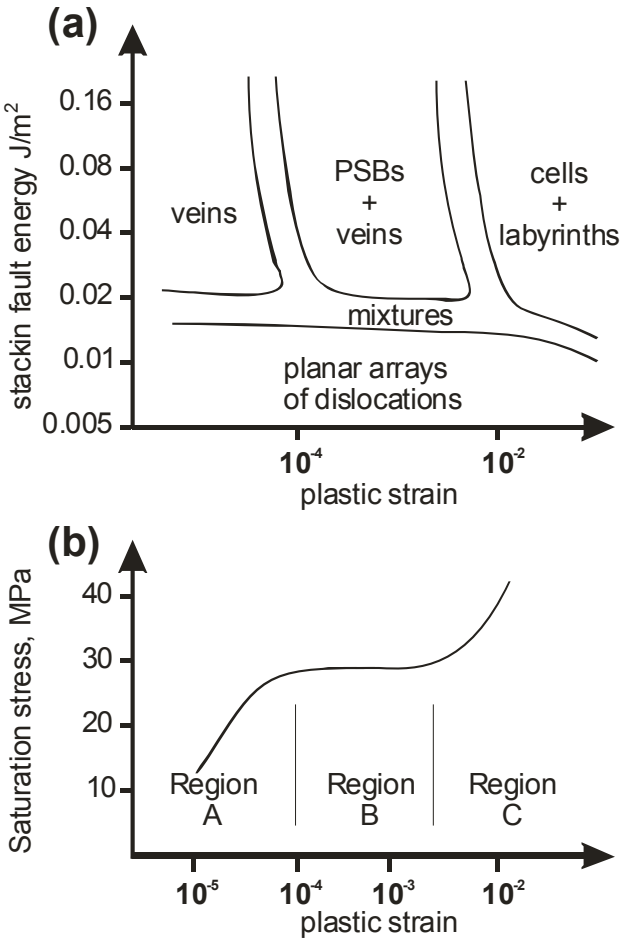

Fig. 2.1
(a) Summary of dislocation structures as a function of plastic strain amplitude. (b) Cyclic stress-strain curve of a Cu single crystal [Basinski and Basinski 1992, Klesnil and Lukáš 1980]

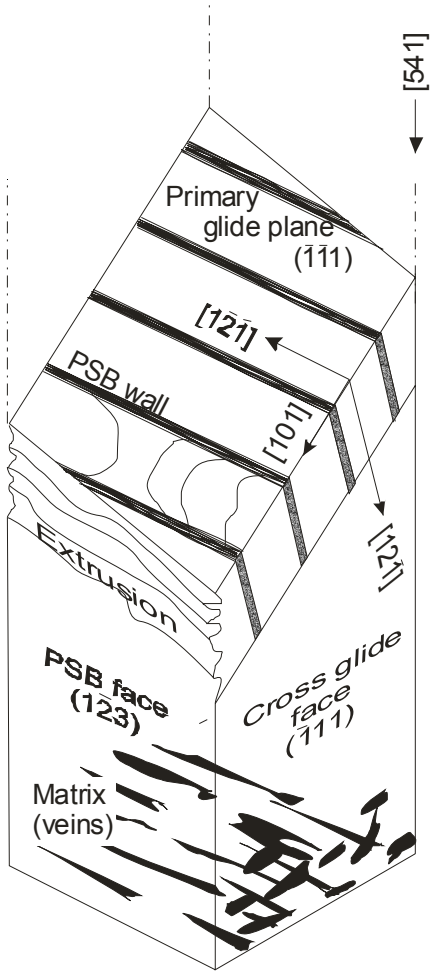

Fig. 2.2
Schematic representation of a persistent slip band in a crystal after [Basinski and Basinski 1992].

Increasing the plastic strain amplitude above 10^{-4} (region B) leads to formation of so-called persistent slip bands (PSBs) which are lamellar structures that are oriented parallel to the active slip system. In region B, the volume fraction of PSBs is quite small. Typically about 90% of the volume is occupied by the vein structure which exists between the PSB lamellae (Fig. 2.2). The PSB lamellae consist of a wall or ladder structure of edge dislocations. In the channels, that is the region between the edge dislocation walls, screw dislocations bow out between walls and accomplish dislocation multiplication. This is an essential process for the plastic deformation of the soft PSB regions during cycling. The distance between neighboring walls is about 1.5 μm for Cu [Mughrabi 1980]. In the strain amplitude regime where PSBs form, the saturation stress exhibits a plateau and increasing plastic strain amplitude does not lead to an increase in the stress amplitude (Fig. 2.1(b)). PSB formation is reversible. When the strain is decreased below 10^{-4}, the PSBs vanish and only the vein structure remains. In Region B, extrusions and intrusions can be found at sites where PSBs intersect the surface. They can be best described as valleys and hills which lie along the intersection of the slip plane with the sample surface (Fig. 2.2). Numerous models have been proposed for the formation of such extrusions. A model from Essmann et al. considers vacancies created by dislocation annihilation as the origin of slip irreversibilities that lead to surface extrusions [Essmann et al. 1981].

For shear strains higher than $2x10^{-3}$ additional slip systems are activated and a gradual change from PSBs to labyrinth structures and later to cell structures occurs. The labyrinth structure originates from the PSB-matrix interface, spreads out and fills the PSB [Ackermann et al. 1984]. The cell and labyrinth structures contain walls that are oriented parallel to the <100> direction, which contain dislocations with two perpendicular Burgers' vectors. Cell or labyrinth formation is irreversible and reducing the strain does not bring back the PSBs or veins. When crystals are oriented for multiple slip, labyrinth and cell structures can also be found for lower amplitudes. Fatigue of polycrystals leads very often to cell formation, because most of the grains are usually not oriented for single slip.

Extrusions have been observed in particular in region B and have also been found in region C. Generally the extrusions can be divided in two types: Fine slip, which occurs during fatigue hardening and consists of fine slip traces on the surface, and coarse slip which occurs after PSB or cell formation and consists of severe surface extrusions and intrusions. The surface extrusions, as well as the intersection of PSBs with grain boundaries and PSB/matrix interfaces, are the preferred sites for crack nucleation [Basinski and Basinski 1992]. Once

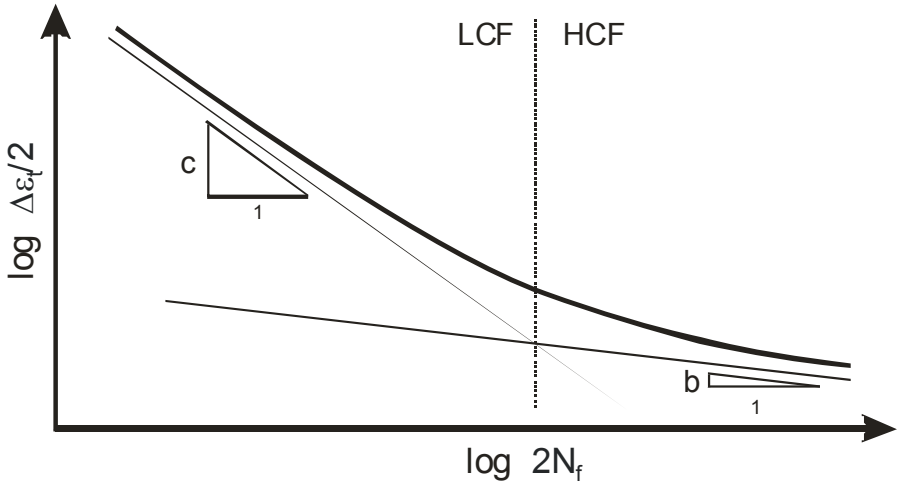

Fig. 2.3 Relationship between strain amplitude and cycles to failure.

cracks are nucleated, they typically propagate and cause failure of the component [Ma and Laird 1989].

All of the processes that have been described here also take place during thermal fatigue as long as the temperature stays below roughly half the melting point of the sample material. For temperatures higher than half the melting point, time-dependent processes like creep become increasingly important and the lifetimes are typically found to decrease with increasing temperature. This is particularly noticeable for fatigue in the presence of an oxidising environment.

Failure of a component occurs by damage formation, crack nucleation, and crack propagation. A schematic plot of the number of load cycles that cause failure and the strain amplitude of the cycles is shown in Fig. 2.3.

The failure behaviour can be divided into two regions, a low cycle fatigue (*LCF*) region and a high cycle fatigue (*HCF*) region. In *LCF*, crack nucleation and growth consume a considerable amount of the lifetime of the metal. This is in contrast to *HCF*, where most of the lifetime of the metal is spent for damage formation. Crack nucleation and growth typically occur only shortly before failure under *HCF*.

The failure behaviour illustrated in Fig. 2.3 can be expressed by a phenomenological power law relationship,

$$\frac{\Delta\varepsilon_t}{2} = \frac{\Delta\varepsilon_{pl}}{2} + \frac{\Delta\varepsilon_{el}}{2} = \varepsilon_f^{'}(2N_f)^c + \frac{\sigma_f^{'}}{E}(2N_f)^b \ , \qquad (1)$$

where $\Delta\varepsilon_t$ is the total strain range, $\Delta\varepsilon_{pl}$ is the plastic strain range, $\Delta\varepsilon_{el}$ is the elastic strain range, and N_f is the number of cycles to failure. The first term in Eq. (1) is the Coffin-Manson Law for *LCF* [Coffin 1954, Manson 1954],

$$\frac{\Delta\varepsilon_{pl}}{2} = \varepsilon_f^{'}(2N_f)^c \ . \qquad (2)$$

It is expressed in terms of the plastic strain range $\Delta\varepsilon_{pl}$, because in *LCF* the strain amplitudes are high and a significant amount of plasticity occurs during each cycle. $\varepsilon_f^{'}$ is called the fatigue ductility coefficient and c is the fatigue ductility exponent. The second term in Eq. (1) is the Basquin law and applies to *HCF* [Basquin 1910],

$$\frac{\Delta\varepsilon_{el}}{2} = \frac{\sigma_f^{'}}{E}(2N_f)^b \ . \qquad (3)$$

$\sigma_f^{'}$ denotes the fatigue strength coefficient and *b* the fatigue strength exponent. E is the appropriate elastic modulus of the material. In *HCF*, the total strain amplitudes are low and plasticity occurs only locally. Although plastic strain is the parameter that drives fatigue, the small plastic strains cannot be measured easily. Therefore stress or elastic strain range $\Delta\varepsilon_{el}$ is often used as a measure of load in the Basquin equation.

2.2 Mechanical properties of thin metal films and fine-grained bulk metals

Thin films, as used in technological applications, experience large stresses due to constraints by the surrounding materials. In typical devices, the metal films or structures are attached firmly to thick wafers. These devices experience temperature cycles during fabrication and operation, and the mismatch between the coefficients of the thermal expansion between substrate and film gives rise to large strains and stresses.

Experiments have shown that thin metal films with thicknesses in the micrometer range have yield strengths that can be an order of magnitude higher than the yield strength of bulk materials [for a review, see e.g. Arzt 1998]. It has been found that the yield strength of thin films increases with the inverse film thickness [Kuan and Murakami 1982, Nix 1989, Venkatraman and Bravman 1992] and with the inverse grain size [Venkatraman and Bravman 1992]. These increases have been attributed to the fact that dislocation motion is constrained by interfaces and grain boundaries. Several dislocation-based models have been developed to calculate the effect of constraints on the yield strength [Chaudari 1979, Nix 1989, Thompson 1993]. One of the models [Nix 1989] considers the motion of a threading dislocation segment through the film which leaves a misfit dislocation segment behind in the film/substrate interface. Since this misfit segment costs energy, the dislocation can only move for stresses

above a certain threshold stress. With this consideration, the increase in yield strength can only account for roughly one third of the stress measured for polycrystalline films [Keller et al. 1999] and additional mechanisms have been considered to account for the high strengths. Among them are dislocation pile-ups at grain boundaries (Hall-Petch effect) and strain hardening. The sum of all of these effects leads to a reasonable agreement with experiments [Baker 2001].

A more recent model considers the nucleation and multiplication of dislocations [v. Blanckenhagen 2002]. For plasticity to occur, dislocation sources have to be activated. It is found that sources with sizes of roughly one third the film thickness or the grain size are the ones that are most easily activated. With further plasticity, the back stress from dislocation pile-ups at interfaces and grain boundaries hinder the further activation of the source and lead to marked strain hardening. This model can also account for the high yield strengths observed in small scale metal structures.

The yield strength of fine-grained bulk metals is also found to increase with decreasing grain size down to grain sizes as small as roughly 20 nm [Weertman 1993, Legros et al. 2000, Baker 2001, Schiøtz and Jacobsen 2003]. Exact explanations for this phenomenon are controversial although it is widely believed to have its origins in either the classic Hall-Petch pile-up argument for strengthening or in the same phenomenon leading to strengthening in thin films, namely dimensional constraint on dislocation nucleation and motion.

At very small length scales, there is some evidence that the yield strength ceases to increase with decreasing dimension. For small film thicknesses (≤ 200 nm), a clear plateau in the yield strength of Cu is observed [Balk et al. 2003]. For very small grain sizes in bulk materials (≤ 20 nm), the yield strength dependence is controversial [Weertman 1993, Baker 2001] but there is some experimental evidence supporting softening [Chokshi et al. 1989]. These effects have been attributed to the onset of new deformation mechanisms, such as the glide of dislocations parallel to the film/substrate interface [Balk et al. 2003] or grain boundary diffusion at room temperature [Chokshi et al. 1989].

2.3 Size effects in fatigue

The fact that constraints on dislocation nucleation and motion cause an increase in yield strength under monotonic loading, leads to the question of whether fatigue is also influenced by geometrical and microstructural constraints. This consideration is further complicated by the formation of fatigue dislocation structures which typically mask interactions of

dislocations with grain boundaries and surfaces. These characteristic dislocation structures (Fig. 2.2) can be several hundred micrometers long and contain sub-structures with a periodicity of the order of 1 μm. It is therefore reasonable to ask what happens in small scale metal structures, where the grain size or film thickness may be smaller than this characteristic distance of about one micrometer.

2.3.1 Fine-grained metals

It has long been known that grain size can play an important role in the fatigue behaviour of certain metals. In one study [Thompson and Backofen 1971], the grain size dependence of fatigue in bulk Al, Cu and α-brass has been investigated. Minimum grain sizes were 20 μm for the Al and Cu and 3.4 μm for the α-brass. It was observed that a small improvement in lifetime occurred in the *LCF* regime with decreasing grain size in all materials. For *HCF*, only α-brass showed an enhancement in the fatigue life with decreasing grain size. Depending on the stacking fault energy the probability of cross slip, and with it the ability to form a cell structure, decreases from Al to Cu to α-brass (Fig. 2.1(a)). The authors argued that the cell structure can hinder dislocation motion and therefore the grain size effect in Al and Cu is masked by cells. Since in a planar slip material like α-brass the formation of cell structures is suppressed, grain boundaries can serve as obstacles to dislocation motion. In a separate study on grain size effects [Lukáš and Kunz 1987], experiments were performed on Cu with two different grain sizes of 70 μm and 1200 μm and shorter fatigue lives for the coarse-grained material were observed. It was argued that the coarser grained Cu formed longer PSBs, resulting in larger stresses and easier crack formation at the intersection of the PSBs with grain boundaries.

Recently, fatigue studies have been extended to fine-grained bulk metals. A good overview can be found in [Mughrabi 2000]. In particular, the production of ultra-fine-grained (UFG) specimens by severe plastic deformation [Valiev et al. 1991], has allowed experiments in a very small grain size regime. Typical grain sizes of these materials are of the order of a few hundred nanometers and large increases in the monotonic yield strength have been measured in these materials. These UFG Cu samples have recently been fatigue tested [Agnew and Weertman 1998, Agnew et al. 1999, Höppel et al. 2000, Höppel and Valiev 2002]. In the *LCF* regime, the UFG Cu seems to have a shorter fatigue life than conventional Cu, which is related to grain coarsening and the extensive formation of shear bands over length scales that are larger than the initial grain size [Agnew et al. 1999], as well as to decreased ductility [Höppel and Valiev 2002]. In contrast in *HCF*, the experiments show a

significant enhancement of the fatigue life of UFG Cu over coarse-grained Cu when the data is plotted as a function of elastic strain or stress (Basquin equation) [Agnew et al. 1999, Höppel and Valiev 2002]. This has been attributed to the increased yield strength in the UFG material. The data was not plotted in terms of the plastic strain amplitude, so it is not clear if there are additional contributions from differences in plastic strain accumulation due to the small grain size. In any case, the observed shear banding and the observation of microstructural instabilities like grain growth during the tests with UFG material show that determination of size effects in these samples may be difficult.

2.3.2 Fatigue of thin films

A number of publications are available in the literature on fatigue of easy cross-slip metals with film dimensions of several micrometers and above [Judlewicz 1993, Judlewicz et al. 1994, Hong and Weil 1996, Merchant et al. 1999, Hadrboletz et al. 2001]. There are some differences in the results of these studies, but most of the studies reveal an increase in fatigue life with decreasing dimension. Since microstructural studies show that typical fatigue dislocation structures have formed in these samples [Judlewicz et al. 1994], the origin of the fatigue life improvement is presumably similar to that observed in studies on the effect of grain size on fatigue in bulk metals [Thompson and Backofen 1971, Lukáš and Kunz 1987], and is due to effects of the sample dimensions on crack nucleation and propagation.

In the literature there is only limited data for films with thicknesses of the order of a few micrometers or less. Nonetheless, the studies that have been performed clearly show that the formation of characteristic fatigue dislocation structures is inhibited in films with thicknesses of roughly 1 μm or less [Read 1998, Schwaiger et al. 2003, Zhang et al. 2003]. Thus, length scale effects are expected to play an important role in these films. In a series of recent experiments [Hommel and Kraft 1999, Kraft et al. 2002, Schwaiger et al. 2003], *LCF* experiments of Cu films on elastic polyimide substrates have been performed. X-ray measurements were used to determine the stresses in the films [Hommel and Kraft 1999]. Films with four thicknesses between 0.4 μm and 3.1 μm were tested and the use of the elastic substrate allowed tensile-compressive tests of the films. It was observed that the number of cycles to form damage in the thicker films was similar to the behaviour of bulk Cu. Extrusions at the surface and voids at the substrate interface as well as intergranular cracks were found in these films. Failure was associated with crack nucleation at voids that were argued to have formed by condensation of fatigue-generated vacancies. In contrast, the two experiments performed on 0.4 μm thick films showed a significantly increased resistance to

damage formation (both in terms of total strain and plastic strain [Kraft et al. 2002]) and did not contain voids. The enhanced life has been attributed to the rapid annihilation of vacancies at grain boundaries so that void formation and crack nucleation is suppressed. Based on these results it appears that for dimensions less than roughly 1 μm, the formation of characteristic dislocation structures is hindered and that, at least under *LCF* conditions, the fatigue life is enhanced.

2.4 Objectives of this work

Sub-micrometer metal structures with high fatigue reliability are of great technological importance and provide a challenge to the fundamental understanding of the fatigue process. Despite this, only limited data is available in the literature on fatigue size effects in the sub-micrometer range. The results of the existing literature studies, which are described above, show that there are a number of important differences in the fatigue damage morphology of small scale materials, which include the fact that characteristic dislocation structures do not form in the sub-micrometer thin films. The studies also show that, as expected, the fatigue life is enhanced due to an increased yield strength.

The aim of this work is to investigate high cycle fatigue in Cu films with sub-micrometer thicknesses. Cu has been chosen for these studies because it is frequently used in modern microelectronic devices and because there are extensive studies on mechanical properties and fatigue of bulk Cu available in the literature. The intent is to look for length scale effects on fatigue damage evolution as well as fatigue life. In the following chapters, a new method for thermal fatigue of thin metal films is presented (Chapter 3) and used to perform *in-situ* studies of fatigue damage evolution (Chapter 4) and lifetime determination (Chapter 5). These studies reveal that entirely new fatigue damage mechanisms are active on small length scales and that the fatigue life is enhanced partly due to an increase in yield strength and partly due to different mechanisms for plastic strain accumulation at small length scales.

3 Thermal Fatigue Testing of Thin Metal Films by AC Loading

3.1 Introduction

Thermal fatigue is a threat in any composite system that experiences thermal cycles during use. Historically, this has been a major reliability concern in systems used in structural applications. Concerns have more recently been raised about thermal fatigue in much smaller structures [Philofsky et al. 1971, Subramanian et al. 2001, Huang et al. 2002, Keller et al. 2002]. For instance, extensive work has been performed on predicting failure due to thermal fatigue of the components of electronic packages with dimensions of the order of 10 to 100 μm [Subramanian et al. 2001]. These concerns even extend to the thin metal films and interconnects found in small-scale systems such as microelectronic circuits and micro-electro-mechanical systems [Philofsky et al. 1971, Keller et al. 2002].

It is well known that dislocation nucleation and motion are constrained by the small dimensions in thin films with fine grains [Nix 1989, Arzt 1998, Keller et al. 1998, Hommel and Kraft 2001]. The process of fatigue damage formation and eventual failure in bulk materials is based on the formation of stable dislocation structures with length scales of the order of a micrometer. Therefore, it is reasonable to question whether fatigue in sub-micrometer structures proceeds in the same fashion as in bulk materials. This question is even more relevant for thermal fatigue, where diffusion-controlled processes which are promoted by the elevated temperatures may proceed differently in small scale structures containing a high density of interfaces. Several observations of fatigue in thin metal structures show that although some of the characteristic features of fatigue are still present, the samples show significantly different fatigue behaviour than their bulk counterparts [Philofsky et al. 1971, Hong and Weil 1996, Read 1998, Schwaiger and Kraft 1999, Kraft et al. 2001, Keller et al. 2002, Kraft et al. 2002, Thiele et al. 2002, Schwaiger et al. 2003, Zhang et al. 2003]. Both the fundamental issues and the potential threat to various applications provide strong reasons to study thermal fatigue in small scale structures.

This chapter describes a method and an apparatus for thermal fatigue testing of thin films on substrates and presents first results of *in-situ* SEM observations of thermal fatigue

damage in Cu interconnects. The basic concept underlying the method is the use of controlled Joule heating, by means of alternating currents to introduce temperature cycles in the interconnects [Philofsky et al. 1971, Keller et al. 2002]. The temperature cycles, in combination with the unavoidable mismatch in coefficients of thermal expansion, lead to cyclic straining of the interconnects and eventually to damage formation. The method is well suited for *in-situ* adaptation and has been implemented in an SEM, where the initial tests on Cu interconnects were performed. This chapter will address the experimental setup and the cyclic temperatures generated in the metal. Some first observations of fatigue damage in Cu lines will be presented and the role of the electrical currents in damage formation will be addressed. Finally, advantages and disadvantages of the method in comparison to conventional fatigue experiments will be discussed.

3.2 Temperature in a Current-Carrying Metal Interconnect

For a typical interconnect in a microelectronic circuit, such as illustrated in Fig. 3.1(a), large current densities used during operation can lead to significant Joule heating in the interconnect. For the conditions found in typical devices, as well as for the thermal fatigue method described in this chapter, most of the heat generated in the interconnect is conducted away by the metal line and the underlying substrate. The temperature of the interconnect is determined by its geometry, the thermal conductivities of the surrounding materials, and the presence of a heat sink or reservoir. In many integrated circuits, this heat sink is provided by a fan-cooled metal block.

Despite the straight-forward concepts behind heating in current-carrying interconnects, solutions to the temperature distributions are generally quite complicated. For example, no simple analytic expression is available for the geometry shown in Fig. 3.1(a), or even for the simpler 2-dimensional case of an infinitely long line on a substrate. However, finite element analysis (FEA) is well suited to modeling such problems. A steady state temperature distribution is shown in Fig. 3.1(b), which was calculated using temperature-independent thermal and electrical properties and applying a DC voltage of 8 V to an 800 μm long Cu line directly on Si (1.41 A, 5.9×10^7 A/m^2). The temperature of the lower side of the 100 μm thick wafer was held at a constant temperature of 100°C, providing a heat reservoir for the sample. Fig. 3.1(b) shows that there is a large temperature gradient through the Si which results in significant heating of the interconnect. As expected, the steady state temperature difference between the interconnect and the reservoir is found to be proportional to the power dissipated

in the line and is determined by the thermal properties of the materials lying between the interconnect and the reservoir.

When an alternating voltage rather than a constant voltage is used, the sample experiences temperature oscillations. The magnitude of these oscillations depends not only on the sample geometry and materials, but also on the frequency. For very low frequency signals in samples that are in good thermal contact with a heat reservoir, the sample remains in steady state during the power cycles and the temperature difference between the interconnect and the reservoir remains proportional to the instantaneous power dissipated throughout such a cycle. For instance, if a sinusoidal voltage $V_o \sin\omega t$ is applied to the line, the instantaneous dissipated power is $V_o^2 \sin^2\omega t/R = V_o^2(1-\cos 2\omega t)/2R$, where t is the time, $\omega/2\pi$ is the frequency, and R is the interconnect resistance. Thus the temperature difference between the interconnect and the reservoir will swing between zero and a maximum value proportional to V_o^2/R at twice the frequency of the electrical signal.

Fig. 3.1

(a) Schematic of interconnect structure used for testing. The line is 800μm long, 8 μm wide and 0.3 μm thick. The region that is modelled by FEA is outlined with a line.

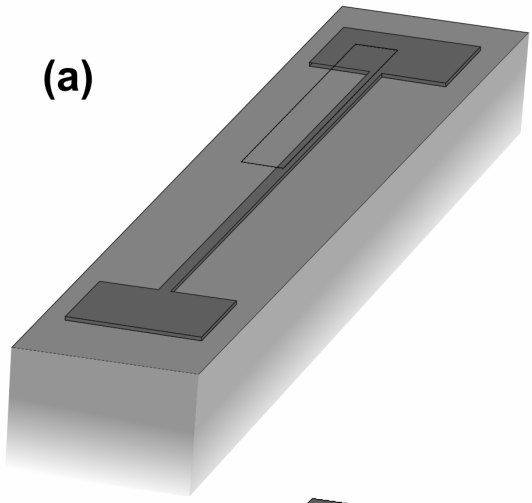

(b) FEA contour plot of temperatures (in °C) due to Joule heating in the interconnect.

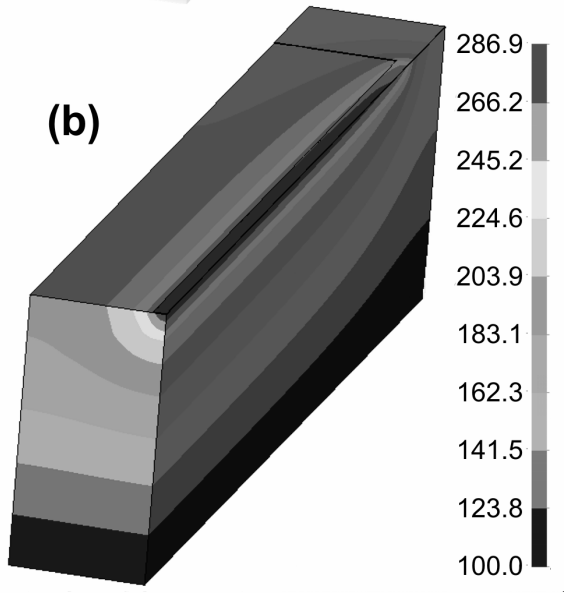

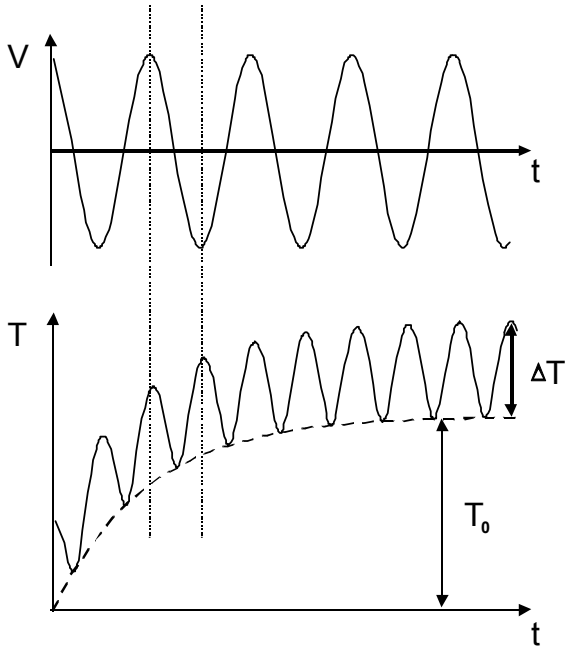

Fig. 3.2 Schematic illustration of voltage and temperature as a function of time during AC testing, including the transient (dashed line) and periodic component. The temperature oscillations occur at twice the frequency of the voltage oscillations.

At higher frequencies there is not enough time for steady state to be reached and the temperature difference is no longer proportional to the instantaneous power. For example, for frequencies higher than roughly 15 Hz, the thermal wavelength $(D/2\omega)^{1/2}$ of Si is of the order of or below a typical substrate thickness of 525 µm. The temperature in the interconnect will still have a periodic component at twice the frequency of the electrical signal, but it will be superimposed on a slower transient. The transient is caused by heating of the substrate and the underlying sample holder due to the time-averaged power. After a characteristic time, which depends on the thermal conductivity and thermal capacitance of the sample, the transient will have saturated, but steady, periodic temperature oscillations will continue to occur. This situation is illustrated schematically in Fig. 3.2, where the transient results in a temperature increase T_o and the periodic component causes cycles with a total temperature range ΔT (two times the temperature amplitude).

An infinitely long and infinitely narrow line on a semi-infinite substrate can serve as a model to study the frequency behaviour of the temperature oscillations. This problem has been solved analytically for the case of a periodically heated line source [Carslaw and Jaeger 1959b, Cahill 1990]. After the transient has saturated and caused a temperature increase of the line and its surrounding materials, the steady periodic temperature oscillations of range ΔT can be calculated. In the immediate vicinity of the line (at a distance from the line, much smaller than the thermal wavelength $(D/2\omega)^{1/2}$ where D is the thermal diffusivity of the substrate), the solution for the temperature range ΔT can be approximated as,

$$\Delta T = \frac{Q}{\pi \cdot k}(-\ln(2\omega)/2 + \text{const}), \qquad (4)$$

where Q is the amplitude of the power per unit length in the line, $\omega/2\pi$ is the electrical signal frequency, and k is the thermal conductivity of the substrate. Thus, the amplitude of the periodic component of the temperature is expected to be proportional to the power and to fall off as the logarithm of the signal frequency. For very high frequencies, the amplitude of the periodic component becomes very small, because most of the power is dissipated in heating the thermal mass of the line and its immediate surroundings and less power remains for the heat flow which causes the temperature gradients.

3.3 Experimental Details

3.3.1 General Setup

Copper lines fabricated on silicon chips, such as the one shown in Fig. 3.1, were used to test and optimize the thermal fatigue setup. The chips were mounted on a temperature-controlled heater block in the chamber of an SEM and electrical connections were made to the contact pads of the Cu line structure using a motorized needle probe station. Temperature cycles were generated by applying a sinusoidally alternating electrical voltage to the interconnects. The temperature ranges of the cycles were determined from 4 point resistance measurements and, due to the mismatch in thermal expansion coefficients between the metal and the substrate, resulted in strain and stress cycles, which caused thermal fatigue in the interconnects. The evolution of the fatigue damage during testing was monitored using SEM imaging. In order to obtain good quality images, the alternating voltage was turned off while the sample was imaged to avoid deflection of electrons by the magnetic fields set up by the alternating current in the samples.

Voltage control rather than current control was used for the experiments to minimize "run away" local heating in damaged regions due to resistance increases. Performing the experiments with fixed voltage amplitude also allowed better control of the sample temperature, since as the sample temperature increases at the beginning of each experiment, the resistance also increases and the average power ($\sim V_o^2/R$) decreases. However voltage control makes the use of established methods for temperature measurement (e.g. the 3ω method [Cahill 1990]) very complicated.

The sinusoidal voltage signal was applied to the test structures using a signal generator and an amplifier as illustrated schematically in Fig. 3.3. A frequency of 100 Hz was used in the tests presented here, but could be varied from DC to roughly 20 kHz. The voltage amplitude was adjusted to reach the desired temperature range ΔT in the line. For the

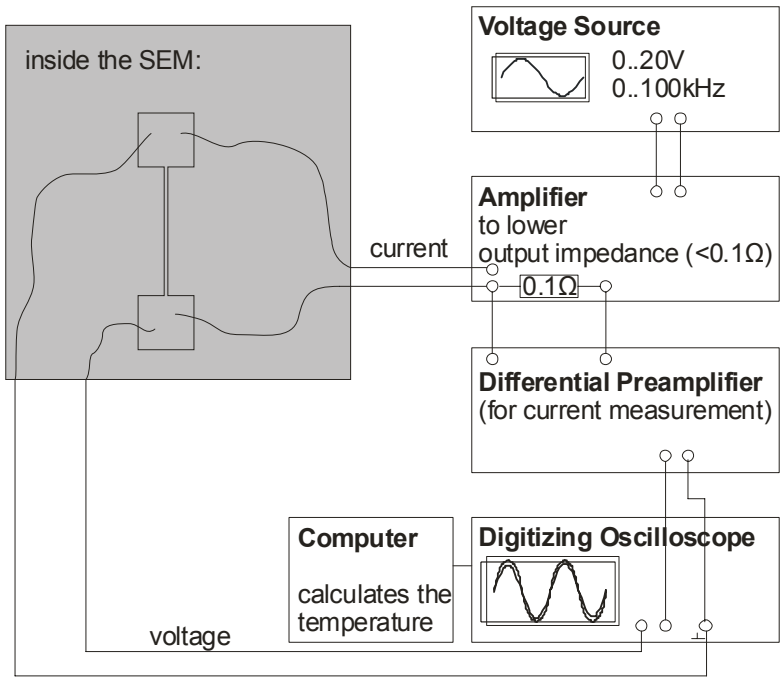

Fig. 3.3
Schematic illustration of the testing set-up.

geometries and structures used here, the voltage amplitudes were between 3 and 8 V which resulted in current amplitudes between roughly 0.6 and 1.0 A (current densities of 1.4 to 2.4 x 10^7 A/m^2), and maximum powers between 2 and 8 W. The DC component was minimized and typically below 5 mA.

With a digital oscilloscope, the time-resolved voltage V(t) and the resultant current I(t) in the test structure were monitored. Due to the temperature variation during the cycles, the current signal is not sinusoidal as can be seen by comparing voltage and current in Fig. 3.4(a). The noise in these time-resolved measurements was reduced by averaging over several cycles and the time resolved resistance was calculated from the voltage and current signals. A typical resistance trace is shown in Fig. 3.4(b) for a signal frequency of 100 Hz. As expected, the resistance varied periodically at twice the frequency of the applied voltage due to the temperature variations created by Joule heating. The scatter in the smallest values of resistance comes from the fact that the voltage and current both pass through zero at this point in the cycle. The temperature of the Si chip was measured using a fine gauge wire thermocouple cemented to a corner of the chip. This thermocouple was used to measure the transient temperature increase at the beginning of each test due to overall heating of the sample and the underlying sample holder. The thermocouple temperature rose for a period of roughly 1 to 2 hours and then saturated at a value of T_o between 70 and 130°C depending on the voltage signal amplitude. To bring the chip more quickly to this temperature, a temperature-controlled heater installed in the block underneath the sample was used to heat up the sample and its surrounding before the tests were started, and then turned off during the test.

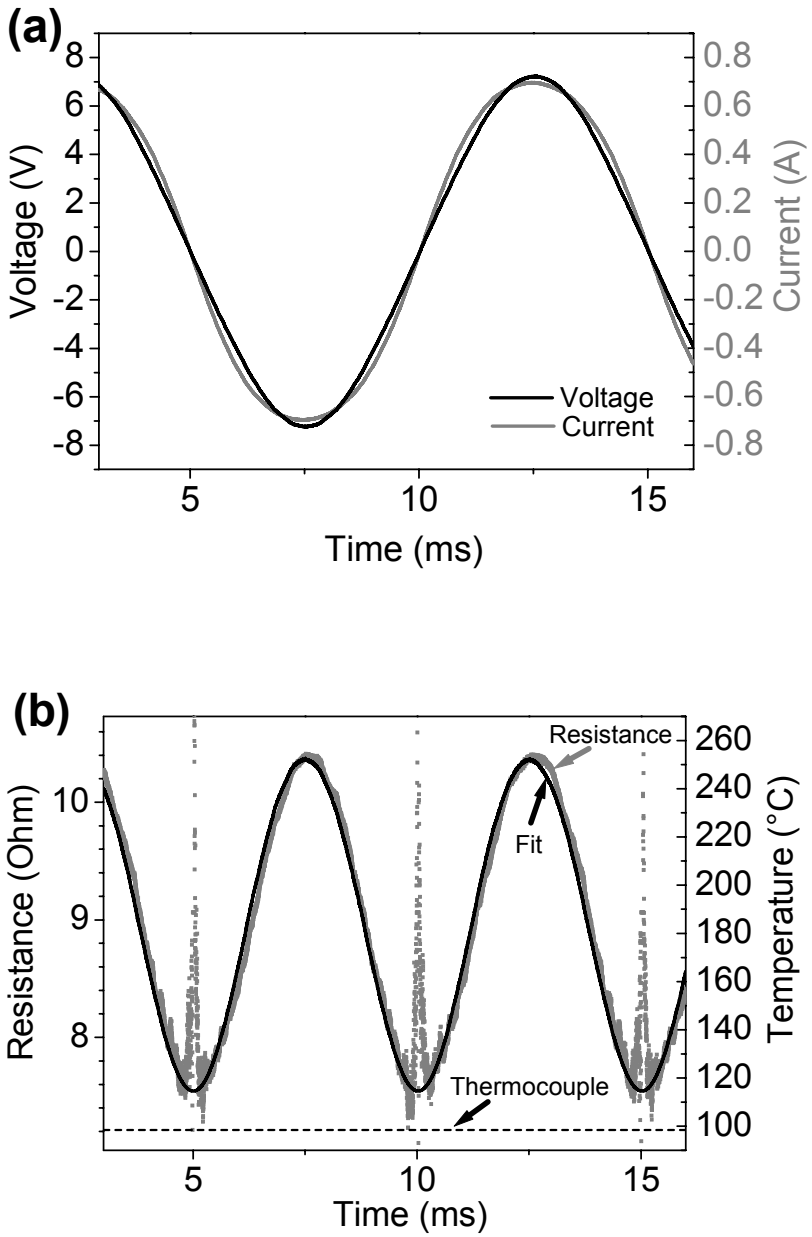

Fig. 3.4
(a) Voltage (—) and current (—) as a function of time.
(b) Resistance (····) and temperature determined using an instantaneous power fit (—). Dashed line (- - - -) corresponds to the temperature measured by the thermocouple cemented to the edge of a 1 cm by 1 cm Si chip.

With this method, a steady value of T_o could be reached within 15 minutes of starting the test. This heater was also used in order to have independent control of the average sample temperature during a test. This allowed additional heating of the sample up to a maximum temperature of 400°C. Limited cooling of the sample was achieved using a Peltier element cemented between the Si chip and the heater block, which provided up to roughly 40 K of cooling during a typical experiment.

3.3.2 Sample Description

The Cu interconnect structures used for the tests were prepared using electron beam lithography, sputter deposition, and a lift-off step. Small pieces (1 cm by 1 cm) of oxidized Si,

525 μm thick with 50 nm of SiO_2 on the top and bottom surfaces, were coated on one side with photoresist and exposed in an SEM. After development, 5 nm of Ta and 100 or 300 nm of Cu were deposited without a vacuum break onto the substrates using magnetron sputtering. 8 to 15 μm wide, 100 or 300 nm thick, and roughly 800 μm long lines were formed by dissolving the photoresist. The 5 nm Ta layer was necessary for adhesion of the Cu to the substrate during the lift-off step. After fabrication, the samples were annealed in a vacuum oven at 400°C for 15 hours in order to allow for grain growth and to stabilize the microstructure. Focused ion beam (FIB) microscopy revealed a heavily twinned columnar grain structure with grain sizes of roughly 0.3 and 1.5 μm in the annealed 100 and 300 nm thick films, respectively. θ-2θ x-ray diffraction measurements revealed that the films had a predominately <111> out-of-plane texture with a small <100> component.

3.3.3 Temperature Measurements

The temperature dependence of the resistivity of the interconnect samples was determined by heating the sample in the vacuum chamber of the SEM using the heater block. The interconnect resistance and temperature of a thermocouple cemented to the Si chip were recorded during cooling back down to room temperature. Since the loss of heat by radiation is negligible [Cahill 1990], the metal line, the thermocouple, and the heater block are at the same temperature. Therefore the thermocouple gives an accurate measure of the interconnect temperature during slow cooling. It was found that the resistance increased linearly with temperature and that the temperature coefficient, $(dR/dT)/R_o = 3.6x10^{-3}/K$ for the 300 nm thick lines agreed well with values in the literature for bulk Cu. There was some variation in the absolute value of the room temperature resistance from structure to structure, presumably due to small differences in line dimensions from structure to structure. However, the temperature coefficient of the resistivity remained constant to within 1% for all of the structures measured.

The time-resolved resistance can be used to determine the temperature in the interconnect from the measured temperature dependence of the resistivity. However, in practice, this process is complicated by two effects. First, there will be temperature non-uniformities along the line. As shown in the FEA calculated temperature distribution in Fig. 3.1(b), the temperatures at the ends of the interconnect line are lower than those in the middle of the line due to the flow of heat into the contact pads. The interconnect temperature increases rapidly with distance from the pad, reaching 90 % of the peak temperature (which occurs at the middle of the line) at a distance of 25 μm from the pad and reaching 99 % at a

distance of 140 μm from the pad. Using the FEA predictions of the temperature distribution along the line, a correction factor (1.031) was obtained to account for the smaller resistance contribution from the cool ends of the interconnect and to accurately predict the temperature in the central uniformly heated region of the 800 μm long interconnects studied here. FEA was further used to estimate the effect of resistance inhomogeneities in the line. These are expected after severe damage has formed, such as a crack that partially spans the line. For example, the calculations show that a temperature increase of only a few degrees is caused by a crack that spans one third of the line width. Thus, the heat is effectively distributed by the Cu line and the Si substrate and local heating due to defects can be neglected.

The second effect that complicates the determination of the temperature from the time-resolved resistance, is the noise in the data when the current and voltage signals pass through zero. This makes it difficult to accurately determine the minimum temperature T_o. One method to compensate for this effect is to assume that the temperature in the interconnect is proportional to the instantaneous dissipated power, V(t)I(t). Such an assumption ignores the effects of temperature dependent material properties, heat losses by radiation, and phase shifts between the temperature and the power signals. A fit to the resistance data using this assumption is included in Fig. 3.4(b) and fits the data very well. Also included in the plot is the temperature measured by a thermocouple cemented to a corner of the Si chip. For frequencies as low as 100 Hz, the thermocouple temperature lies somewhat below the minimum temperature in the interconnect.

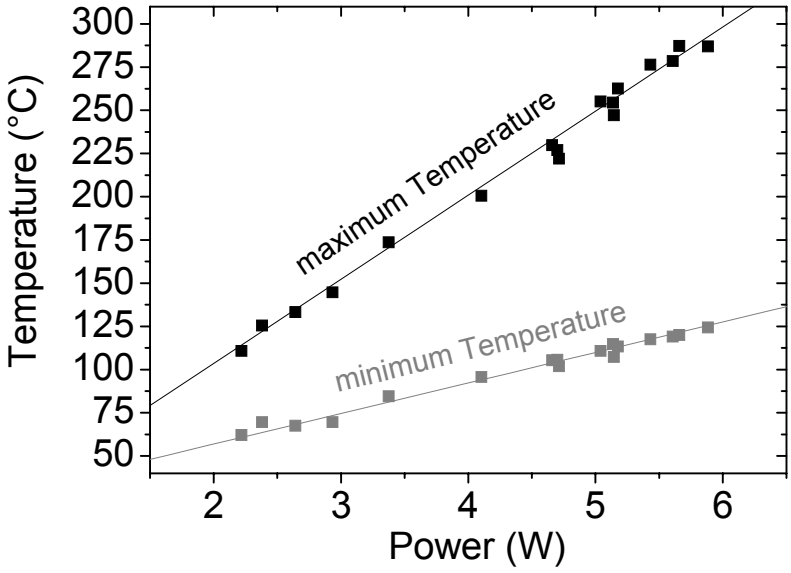

Fig. 3.5 Maximum (■) and minimum (■) temperature in 8 test structures (300 nm thick, 8 μm wide, 800 μm long) plotted against the applied peak power. The lines show linear fits to the data.

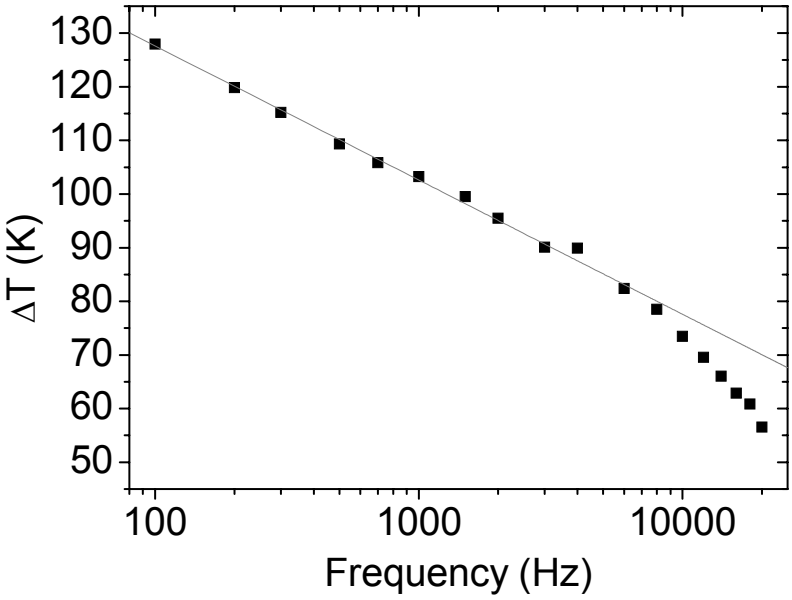

Fig. 3.6 Temperature range ΔT as a function of applied frequency for constant applied peak power of 4.5 W (sample dimensions: 300 nm thick, 8 μm wide, 800 μm long). The solid line is a fit to the data using the solution for a line heat source at the surface of a semi-infinite solid (Eq. 4).

Plots of the minimum temperature T_o and the maximum temperature $T_o+\Delta T$ are shown as a function of the applied peak power in Fig. 3.5. Both temperatures could be determined with a precision of roughly ±3 K with the method described. The fact that both T_o and ΔT scale linearly with the power supports the idea that radiative heat losses from the sample are negligible in comparison with the heat conducted away through the Si [Cahill 1990] and that the temperature dependence of the material properties (other than the resistance) can be ignored. The relatively small scatter in the data means that the desired temperature range can be accurately selected by choosing the appropriate peak power.

A plot of the temperature range ΔT as a function of the signal frequency for constant applied peak power is shown in Fig. 3.6. A constant maximum power of 4.5 W was applied and the minimum and maximum temperature in the line were recorded at different frequencies. The temperature of the thermocouple attached to the corner of the Si stayed nearly constant between 102 and 105°C for all of the frequencies. As expected from Eq. (4), ΔT falls off with increasing frequency, so that larger and larger powers are needed to reach a desired temperature range. This increases the average temperature T_o and eventually makes the tests impractical. With a linear fit to the data at lower frequencies using Eq. (4), a value of the thermal conductivity of 82 W/mK was obtained. This agrees well with literature data for Si at 500 K. However, above 6 kHz, ΔT falls off more rapidly with frequency. This can be

understood by considering the sample geometry in conjunction with the thermal wavelength $(D/2\omega)^{1/2}$. At 100 Hz, the thermal wavelength is of the order of 200 μm, but for a frequency of 6 kHz, the thermal wavelength is only two or three times larger than the line width. The observed behaviour at high frequencies can presumably be understood as the transition from a regime where the interconnect acts as a line heat source to a regime where the interconnect acts as a planar heat source. For a planar heat source, ΔT is proportional to the inverse of the square root of the frequency [Carslaw and Jaeger 1959a, Gui et al. 1998] and falls off more quickly with frequency than for a line source (Eq. (4)), explaining the behaviour shown in Fig. 3.6.

3.3.4 Thermal stresses

Due to the difference $\Delta\alpha$ between the thermal expansion coefficients of Cu and Si, the temperature variations cause strain cycles in the interconnect. Assuming $\Delta\alpha$ is temperature-independent, the total biaxial strain amplitude due to the temperature cycles is given by $\Delta\varepsilon = \Delta\alpha\Delta T$. For example, using $\alpha = 1.7\text{x}10^{-5}$/K for Cu and $\alpha = 3\text{x}10^{-6}$/K for Si, a change in temperature of 100 K would lead to a change in strain of 0.14%. However, in writing this equation, several approximations have been made: Strain relaxation at the line edges has been ignored, which is reasonable in lines which are much wider than they are thick. In addition, the fact that the Si underneath the interconnect is somewhat cooler than the interconnect itself (Fig. 3.1(b)) has been ignored since it has only a small effect on the strain amplitude in the interconnect.

The imposed strains result in both elastic and plastic responses in the interconnects. These can be estimated from the measured stress in a continuous film prepared by the same deposition process as the interconnect structures. Fig. 3.7 shows wafer curvature measurements [Keller et al. 1998] of the stress from such a film during thermal cycling in a controlled atmosphere oven. On heating from room temperature, the initial biaxial tensile stress in the film decreases and becomes compressive, roughly following the thermal-elastic slope for a <111> out-of-plane oriented Cu polycrystal (solid line in Fig. 3.7)). Contributions from the 5 nm thick Ta film to the stress curves were assumed to be negligible. At around 200°C, the stress deviates significantly from the elastic slope, indicating the onset of macroscopic plasticity. Plasticity continues to determine the stress behaviour up to the maximum temperature. On cooling, the stress first increases elastically, and then begins to deform plastically below 250°C. Based on the cycles shown in Fig. 3.7, a thermal cycle between 50°C and 400°C results in a total stress amplitude of 800 MPa and considerable

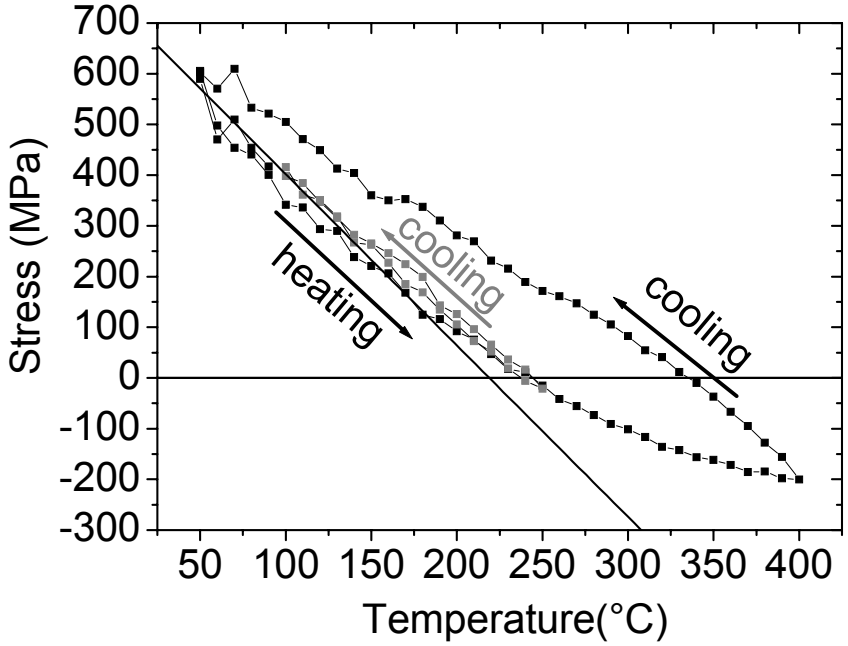

Fig. 3.7 Stress during temperature cycling ( ) in a 300 nm thick Cu film. The grey points ( ) show a thermal cycle over a typical temperature range of a fatigue test. The thermal-elastic slope for a <111> out-of-plane oriented film is shown as a solid line. Arrows indicate the direction of heating and cooling.

plasticity, while a cycle between 100 and 250°C gives a completely tensile cycle with a total amplitude of 400 MPa and only little macroscopic plasticity.

The difference between the stress state in the film, determined using wafer curvature measurements, and in the finite width line used in the thermal fatigue tests can be ignored to first order since the substrate is relatively stiff and the line width is much greater than the line thickness. However, a number of important differences are expected due to issues such as cycle frequency (one hour was typically required for a single wafer curvature cycle) and number of cycles. Most importantly, the stress-strain curves are expected to change and evolve during fatigue testing due to fatigue hardening or softening of the metal [Suresh 1998, pp.63-67]. Thus, the wafer curvature measurements provide only an estimate of the stress in the samples during thermal fatigue.

3.4 Fatigue Damage in Copper Interconnects

Fatigue tests were performed for several different temperature ranges ΔT from 120 to 190 K and for up to $2x10^8$ cycles. The minimum temperature T_o was between 70 and 130°C during these tests and the voltage signal frequency was 100 Hz. In all cases except the smallest temperature ranges, damage patches were observed to form during testing along the length of the interconnect. In general, the patches were evenly distributed along the length of the interconnect except in regions close to the contact pads where no patches were observed, presumably because the temperature amplitudes are smaller in these regions. Fig. 3.8 shows several damage patches in a region of a 300 nm thick interconnect after $3.3x10^5$ cycles at a temperature range of 170 K. In the damaged region at left of Fig. 3.8, parallel surface wrinkles can be seen. These surface wrinkles are similar to the parallel extrusions and intrusions observed at the surface of mechanically fatigued bulk metals [Suresh 1998, p.103]. A cross-section of one of the wrinkled regions made using a FIB microscope revealed that the intrusions extended almost to the substrate.

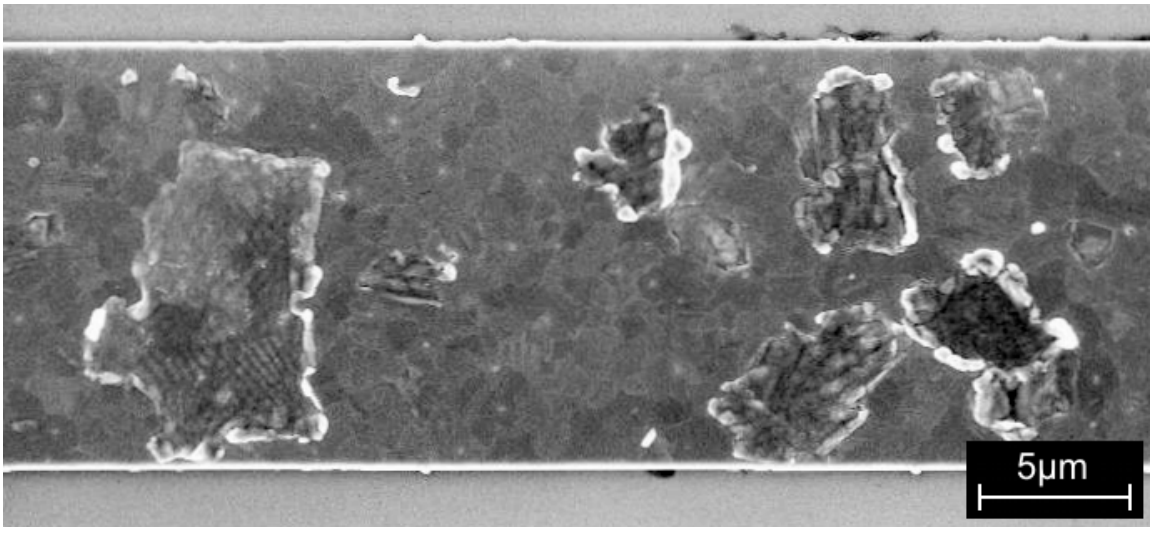

Fig. 3.8 Damage patches in a Cu interconnect (300 nm thick, 15 μm wide, 740 μm long) after testing at ΔT=170 K (Δε = 0.24%) for $3.3x10^5$ cycles.

As the number of cycles was increased, the damage in the 300 nm thick interconnects became more severe and eventually the interconnects failed by an electrical open. A typical failure site is shown in Fig. 3.9. The edges next to the failure site look as though they may have melted during the failure process. This presumably occurs because a decrease in the line cross-section, possibly near an intrusion, results in current crowding and local heating which eventually causes local melting and failure. A series of experiments to determine the number

of cycles to failure revealed a strong dependence on the temperature amplitude. For ΔT of 120 K, no failure could be found even after $5x10^7$ cycles. For larger ΔT, failure happened more quickly and at the highest ΔT of 190 K failure occurred within as few as $1x10^5$ cycles. The fact that the number of cycles to failure decreases with increasing ΔT, or strain amplitude, is consistent with general fatigue behaviour.

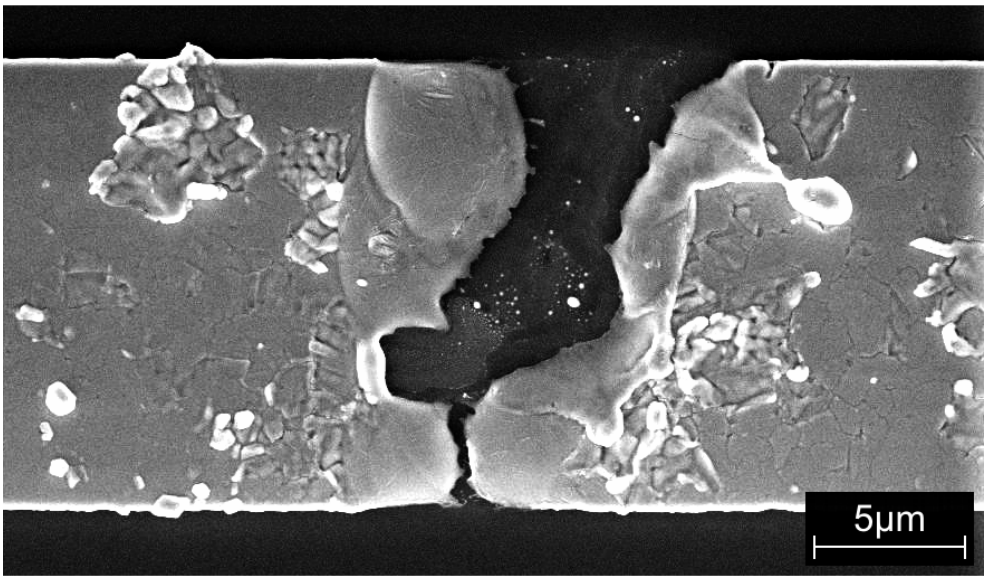

Fig. 3.9 Failure site in a Cu interconnect (300 nm thick, 15 μm wide, 740 μm long) after testing at ΔT =180 K (Δε = 0.25%) for $2.0x10^5$ cycles.

Fatigue damage was also observed in the 100 nm thick films. In these films, the damage appeared as thinned grains, hillocks, and grain boundary grooves all along the length of the interconnect. There was no evidence for the wrinkled damage patches observed in the thinner films. In addition, the number of cycles to failure of the 100 nm thick films was up to two orders of magnitude higher than that of the 300 nm films for a given temperature amplitude. This increase in the number of cycles to failure with decreasing film thickness agrees with previous observations on mechanically fatigued Cu films [Kraft et al. 2002]. The change in the damage morphology reveals that with decreasing grain size and film thickness, fatigue appears to be more and more controlled by diffusive mechanisms and interface properties rather than by dislocation glide.

Although the AC densities used here are large in comparison with those used in DC electromigration experiments, the damage observed here does not look like typical electromigration damage. Typical electromigration damage usually appears as depletion at one end of the interconnect and hillock formation at the other [e.g. Blech and Herring 1976; Kraft and Arzt 1996] and is caused by a current-induced atom motion in the direction of the

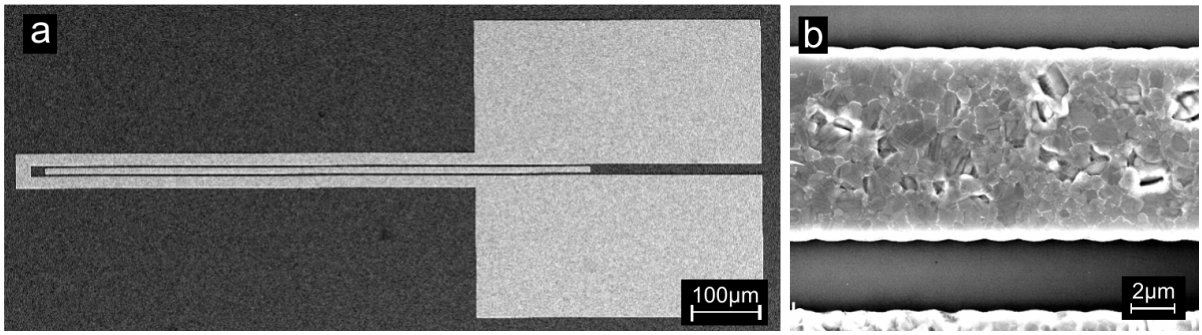

Fig. 3.10 SEM image of structure used to test for electromigration-induced damage (sample geometry: 300 nm thick, inner line 8.5 µm wide, outer line 16 µm wide). The inner line is electrically isolated from the outer line and carries no current. (b) Damage in the middle interconnect has formed without a current.

electron flow. Early stage electromigration damage can be "healed" by reversing the current, which explains why it is not observed under high frequency AC tests [Hu 1998]. Nonetheless, to rule out significant contributions from electromigration-induced atom transport, tests were performed with a special test structure in which temperature oscillations could be introduced without current. The test structure is illustrated in Fig. 3.10(a). A sinusoidal voltage signal was applied to the outer, wider interconnect using the contact pads. The middle, narrower interconnect experienced temperature oscillations due to the current in the neighboring wider lines, but it carried no current. The magnitude of the temperature amplitude in the middle interconnect was estimated from two-dimensional FEA calculations as being roughly 0.93 of the temperature amplitudes in the outer interconnects. Following ~10^5 cycles at a temperature range of ~250 K in the outer interconnects, damage patches were observed to have formed in both the outer and middle interconnects. An image of the damage formed in the middle interconnect is shown in Fig. 3.10(b). The damage looks different from that in Fig. 3.8 due to the finer grain size in these structures. Nonetheless, it provides unequivocal evidence that the damage observed in the experiments presented here is predominately due to thermal fatigue and not to electromigration-induced atom transport.

3.5 Discussion

This chapter describes a method for performing thermal fatigue tests in total strain control on small structures and presents first results of fatigue in Cu lines as an illustration of the method. Compared to conventional fatigue experiments, this method has several advantages. The most obvious advantage is the ease of use. In typical fatigue experiments tensile/compressive tests are performed by precise mechanical equipment. Therefore the frequency of the experiments is limited and experiments are difficult to perform when the size of the specimens is in the micrometer range. The AC induced fatigue testing presented here does not rely on any mechanical parts or specimen clamping and therefore very small samples can be examined. In fact even much smaller structures than the ones shown here can be investigated. Instead of complicated equipment for applying and measuring force and displacement, only electrical contacts are needed to supply the power and to apply the strains. This offers the possibility of performing the experiments *in-situ*, to investigate the damage locally during testing as shown here in an SEM. The frequency of the tests is only limited by the thermal diffusivities, therefore experiments over a wide range of frequencies from DC conditions to 10^4 Hz (and presumably higher depending on materials) can be run. Further application of this method for example to *in-situ* TEM is certainly possible although the appropriate electrical power and frequencies will need to be carefully considered in a geometry where thermal contact to the sample is difficult.

One major limitation of this method is that the strain and the temperature cannot be varied independently. A second major limitation is that the stresses cannot be measured during testing. This is an important issue, because most metals undergo cyclic hardening or softening during fatigue tests. Thus, when experiments are performed under strain control, the stresses during testing may deviate significantly from the stresses measured at the beginning of the tests limiting the utility of using wafer-curvature measurements to determine stress-strain curves. Also, fatigue-induced damage formation is driven by plastic strain which cannot be directly determined in these total strain-controlled tests.

Due to the high current densities and temperatures, electromigration, thermomigration and other diffusive processes could be expected to play a role. However, experiments presented here reveal that to first order the damage is generated by cyclic loading and is not caused by electromigration. There may still be small effects from electromigration and thermomigration once damage has formed and current crowding and thermal gradients are present [Bastawros and Kim 1998]. Since these effects are all strongly temperature dependent, they can be minimized by keeping the average temperature in the sample sufficiently low.

3.6 Summary

A simple and effective method has been developed to perform total strain–controlled thermal fatigue tests on small scale structures:

1. The method relies on using alternating currents to periodically heat metal structures on top of thick substrates. Because of the difference in thermal expansion coefficients between the metal and the underlying substrate, the temperature cycles impose strain cycles in the metal at twice the frequency of the electrical current.
2. The strain range that can be applied to the metal structures is determined by the difference between the thermal expansion coefficients of the metal and the substrate and by the applied temperature range. Typical maximum values of the total strain range are 0.4%.
3. There are no fundamental limits of the dimensions of the samples that can be tested using this method. In the experiments presented here, samples with cross-sectional dimensions between 100 nm and 20 μm and lengths of approximately 1 mm were tested.
4. There is no lower limit on the frequency that can be applied with this method. The highest allowable frequency is determined by the dimensions and thermal diffusivities of the sample materials. For the case of thin Cu structures on Si substrates, significant temperature amplitudes were achieved at frequencies as high as 40 kHz.
5. The method is ideally suited to *in-situ* use. In the experiments presented here, thermal fatigue experiments were performed *in-situ* in an SEM to allow direct observation of the fatigue-induced surface damage.

Preliminary observations of fatigue damage and failure have been obtained using this method from 100 and 300 nm thick Cu lines and the nature of the damage was observed to depend strongly on the film thickness. Future results from studies of this kind may help to further reveal the effect of length scale on mechanical properties and to help assess the reliability threat from thermal fatigue in small metal structures used in many applications.

4 Evolution of Thermal Fatigue Damage in Cu Thin Films

4.1 Introduction

Mechanical fatigue in macroscopic metal components has received considerable attention because of its complexity and great technological relevance. Many of these studies on large-grained bulk metals have concentrated on understanding the damage evolution during fatigue. Generally, fatigue damage formation starts with localized dislocation glide on specific slip systems. These dislocations interact to form complex, extended dislocation structures, such as veins, persistent slip bands (PSBs), cells, and labyrinths. Exactly which of these characteristic structures are formed depends on the nature of slip in the sample material, the stress state, the plastic strain amplitude, and the accumulated plastic strain [Mughrabi 1979, Laird 1983]. Where these dislocations structures intersect surfaces or boundaries, cracks are often nucleated. These cracks propagate and eventually lead to macroscopic failure of the component.

Recently, fatigue studies have been extended to fine-grained metals [Agnew and Weertman 1998, Vinogradov and Hashimoto 2001, Höppel and Valiev 2002, Höppel et al. 2002] and to small scale metal structures and films [Read 1998, Kraft et al. 2001, Kraft et al. 2002] with dimensions and grain sizes of a micrometer or less. These studies have been partly motivated by a number of important technological applications. For instance, fine-grained metals are being considered for use in many components – including those demanding high fatigue reliability – because of their high strength. Similarly, reliable small scale metal structures are needed to survive the often extreme mechanical and thermal conditions in microelectronic and micro-electro-mechanical devices during use. A second important motivation for these studies on fine-grained and small scale metals has been interest in length scale effects in fatigue behaviour. The refinement of grain size has long been recognized as a means to improve fatigue properties of bulk metals. In planar-slip metals (low stacking fault energy), a clear improvement in fatigue behaviour with decreasing grain size is observed in both high cycle fatigue (*HCF*) and low cycle fatigue (*LCF*) regimes. It has been argued that the dislocations interact with the grain boundaries, which are not masked by the planar

dislocation structures that are generated in planar slip metals during fatigue, explaining the strong dependence of fatigue performance on grain size [Thompson and Backofen 1971]. In wavy-slip metals (high stacking fault energy), the fatigue performance is moderately improved by grain refinement in the *LCF* regime but is only very slightly improved in the *HCF* regime [Thompson and Backofen 1971, Lukáš and Kunz 1987, Mughrabi 2000]. It has been argued that the formation of dislocation cell structures in wavy-slip metals blocks dislocation glide and masks the grain size effect. The fact that a grain size effect is observed at all in the wavy-slip metals has been explained by the fact that cracks nucleate and propagate more easily in coarser grained metals [Lukáš and Kunz 1987]. For grain sizes of the order of or below the characteristic spacing of the fatigue dislocation structures of about one micrometer in wavy-slip metals, grain size effects should become important, because dislocations can easily interact with grain boundaries. Not surprisingly, various studies have shown that these structures cease to form in grains smaller and films thinner than around a micrometer [Read 1998, Thiele et al. 2002, Schwaiger et al. 2003, Zhang et al. 2003]. In addition, it is well known that dislocation nucleation and motion are hindered in small dimensions [Nix 1989, Thompson 1993, Arzt 1998, Keller et al. 1999, Baker 2001, Baker et al. 2001, Hommel and Kraft 2001, v. Blanckenhagen 2002, Balk et al. 2003]. This means that there should be fundamental differences in fatigue behaviour in small scale and fine-grained metals relative to their large-grained bulk counterparts.

This chapter and the next chapter deal with fatigue in sub-micrometer thick Cu films with micrometer-sized grains. The next chapter (Chapter 5) concentrates on the effects of microstructure and film thickness on the number of cycles to failure . This chapter focuses on the microscopic evolution of fatigue damage in Cu films deposited on either oxidized Si or sapphire substrates. A new method has been used for performing the tests which consists of straining the specimens thermomechanically (Chapter 3) and allows *in-situ* scanning electron microscopy (SEM) observations of the damage evolution. The observations show that the fatigue damage in the thin Cu films evolves fundamentally differently from that in large-grained, bulk Cu. The results will be discussed in terms of the inhibition of the formation of extended dislocation structures, constrained dislocation motion, and enhanced interface diffusion in the small scale structures.

4.2 Experimental details

4.2.1 Testing method

A recently developed method (Chapter 3) has been used to perform thermal fatigue tests *in-situ* in an SEM on Cu line structures on oxidized Si and sapphire substrates. The basic concept underlying the method is the use of Joule heating from alternating currents to introduce temperature cycles in the lines. Due to the thermal mismatch between the metal line and the substrate, the temperature cycles lead to cyclical straining of the lines. The cyclic strains cause fatigue damage formation in the lines and eventually lead to electrical failure. The method provides a way to perform total strain controlled thermal fatigue testing on very small structures, while monitoring the damage evolution using SEM imaging.

The samples for testing were mounted in an SEM with the lower side of the sample substrate attached with thermal paste to the sample stage. The contact pads of the Cu line structures were then electrically contacted using a motorized needle probe station in the SEM. An alternating voltage with a frequency of 100 Hz was applied to the lines to generate temperature excursions. The voltage amplitude (3 to 10 V) was adjusted to reach the desired temperature range ΔT (130 to 220 K) in the line. The temperature range ΔT is twice the temperature amplitude. The minimum temperatures depended on the electrical power and were between 70 to 130°C for all tests. The alternating voltage resulted in currents with amplitudes ranging between 0.45 and 0.80 A (1.5 to 2.7 x 10^7 A/m^2), and maximum powers between 2 and 8 W. The DC component of the current was typically below 5 mA. 4-point resistance measurements (time resolution <1 μs) were used to determine the temperature in the line during testing. From this measurement of the temperature cycles, the corresponding total strain range $\Delta\varepsilon$ was determined by using temperature independent values of coefficients of thermal expansion (Cu: 1.7×10^{-5}/K, Si: 3×10^{-6}/K, sapphire: 5×10^{-6}/K). The evolution of the fatigue damage during testing was monitored using SEM imaging of the interconnect. In order to obtain good quality images, the alternating voltage was turned off while the sample was imaged to avoid a distortion of the electron beam by the magnetic fields set up by the alternating current in the samples. Further details about the testing method can be found in Chapter 3.

4.2.2 Sample preparation

Cu line structures with contact pads suitable for electrical connections were fabricated on oxidized Si and on sapphire substrates. The lines had widths between 8 and 14 μm, thicknesses of 200 and 300 nm, and lengths of about 800 μm.

The Cu line structures on oxidized Si chips were produced by electron beam lithography, sputter deposition and subsequent lift-off. The Si wafers that were used for the substrates were either coated with 50 nm thick layers of thermal oxide and SiN, or with only the native oxide. The Si wafer was cleaved into rectangular shaped pieces with dimensions of roughly 1 cm by 1 cm. These were first spin coated with positive photoresist and then exposed in an SEM to define the electrical test structures. After resist development, Ta and Cu metal films were deposited onto the wafers by long throw magnetron sputtering. Long throw sputtering was used (30 cm from target to sample) to create a parallel flux of atoms at the substrate and avoid deposition of metal on the side walls of the patterned photoresist. This ensured that the resist could be dissolved during the lift-off process, leaving the desired metal structures behind. The sputter deposition occurred at a base pressure of ~$7x10^{-5}$ Pa and the substrates were cleaned by Ar ion bombardment before sputtering. A continuous, 10 nm thick Ta layer was first deposited (to improve the Cu texture and adhesion) and then Cu films with thicknesses of 200 nm or 300 nm were deposited at a rate of 9 nm/min. Afterwards, the resist was dissolved in acetone to perform the lift-off process. Several blanket film samples on Si chips to be used for film characterization were produced in the same sputter deposition runs with the line structures. The films and the structures were annealed in high vacuum at 400°C for 15 h and then stored in vacuum to prevent oxidation of the sample surface.

The Cu line structures on sapphire were produced by a different process. First, blanket films of 300 nm of Cu were sputter deposited onto sapphire wafers in ultra high vacuum with a base pressure in the low 10^{-8} Pa range. Before deposition the substrates were cleaned by Ar ion bombardment. The wafers were heated to about 200°C during deposition to improve the quality of the epitaxy. After deposition, the film was annealed for 20 minutes at 600°C in ultra high vacuum in the deposition chamber. The wafer was then removed from the deposition chamber and cut into chips. Negative photoresist was then spun onto some of the chips and conventional optical lithography was performed to define structures with the same dimensions as the Cu on Si structures. After resist development, the uncovered Cu was etched away (Seno 3207). Finally, the photoresist was removed from the structures using acetone.

4.2.3 Microstructure and fatigue damage characterization

Microstructure and fatigue damage were characterized using backscattered electron (BSE) and secondary electron (SE) imaging in an SEM, electron backscatter diffraction (EBSD) in an SEM, focused ion beam (FIB) microscopy and cross-sectioning, and X-ray diffraction. X-ray θ-2θ scans of the blanket Cu films on Si showed strong <111> and weaker <100> out-of-

plane texture components in the Cu as well as a peak from β-Ta. An X-ray diffraction pole figure from a Cu on sapphire sample showed that the films had a very sharp <111> out-of-plane texture (Full-width-half-maximum of 1°) with two different in-plane orientations. The in-plane orientations were separated from each other by 30° and had fairly wide in-plane texture distributions (Full-width-half-maximum of 13°).

Channeling contrast images were obtained using FIB, SE, and BSE imaging. The images showed that the Cu on Si films were heavily twinned and that the mean grain sizes (excluding twin boundaries) were roughly 1.0 μm for the 200 nm thick films and 1.5 μm for the 300 nm thick films (Fig. 4.1(a)). The angles between the twin lamellae within a single grain were used to roughly estimate the out-of-plane orientation of the grain: 3-fold symmetry

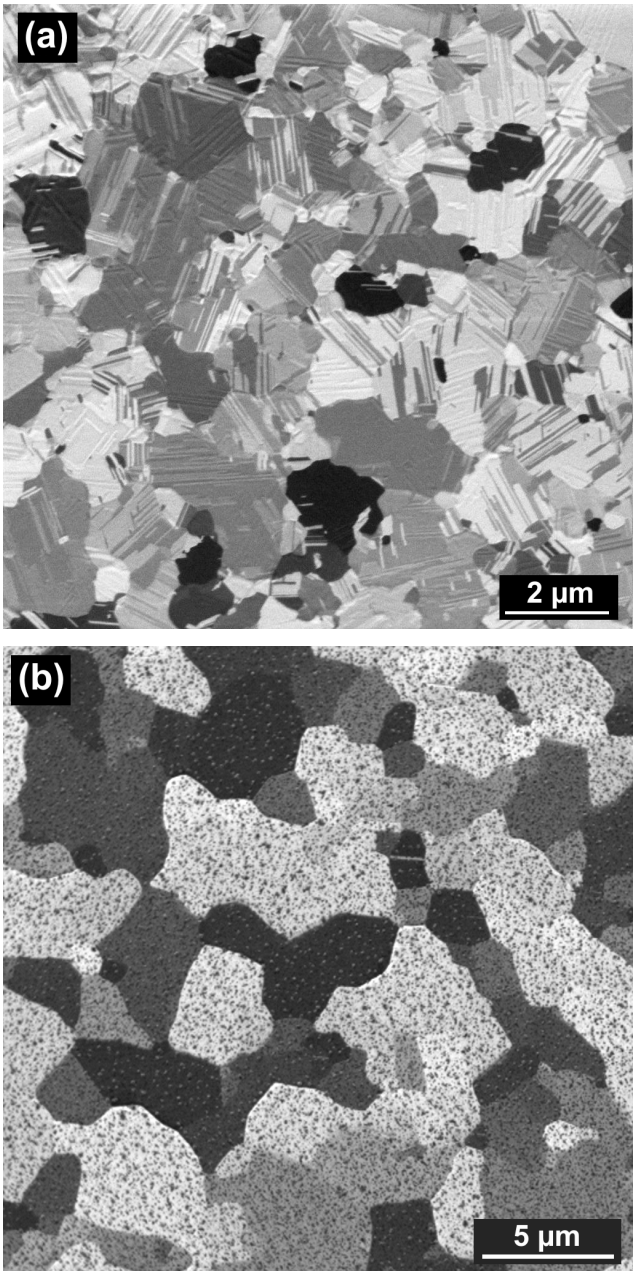

Fig. 4.1 FIB images (taken at an angle of 30° to the sample normal, corrected for tilt) from the 300 nm thick Cu films on Si (a) and on sapphire (b). Image (a) has twice the magnification of image (b). Unidentified dark spots on the surface of (b) are artefacts from the film deposition process.

indicated a <111> out-of-plane oriented grain and 4-fold symmetry a <100> out-of-plane oriented grain. In-plane orientations could be estimated from the twin orientations assuming that the twin boundaries were the <111> twinning planes. FIB imaging of the Cu on sapphire samples revealed typical grain sizes between 2 and 7 micrometers (Fig. 4.1 (b)). In contrast to the Cu on Si samples, the grains in the Cu on sapphire samples were almost twin-free.

Crystallographic orientations of individual grains could be more precisely determined using EBSD. However, due to imprecision in sample mounting, the in-plane and out-of-plane orientations could only be determined to within roughly ±2°. On the occasions when they were compared, the EBSD results were in agreement with the less precise determination of orientations from the twins in the images.

The damaged regions that were created in the lines by fatigue testing were investigated during and after testing. Both BSE and SE imaging were applied *in-situ* in the SEM. These methods provided information about surface topography, and through the use of channelling contrast, about grain sizes, grain orientations, and twin structure. The tests were also interrupted at various stages of testing to perform EBSD analysis. EBSD was used to determine grain size and orientation when the surface became too rough to use channelling contrast images. At the end of the tests, the samples were examined using FIB imaging and cross-sectioning. This allowed the surface topography to be examined more carefully and made it possible to look for subsurface damage. All images of the damage were taken at normal incidence.

4.3 Results

During thermal fatigue testing, localized damaged regions formed along the length of the Cu lines. Two such regions are shown in Fig. 4.2 for a 200 nm thick line before and after testing using a temperature range of $\Delta T \sim 220$ K for 3.8×10^5 cycles (1886 s). The damage patches were typically a micrometer or less in size when they were first discerned in the SEM. As the number of cycles increased, the damage patches grew in extent, sometimes reaching sizes as large as 20 μm along the line length. They eventually caused electrical failure of the lines. Details about the number of cycles to failure and the distribution of damage patches as a function of the temperature range can be found in Chapter 3.

Channeling contrast and EBSD showed that the damage patches were almost always confined to single grains and that the damage morphology and evolution depended strongly on the out-of-plane grain orientation. For example, the large faceted damage patch at the left

in Fig. 4.2(b) is typical for a <100> oriented grain and the smaller non-faceted region at the right is typical for a <111> oriented grain. In addition, damage in <100> grains was observed to form at lower temperature amplitudes and after fewer cycles, indicating that the <100> grains were more susceptible to damage formation. Because of these differences, the damage evolution in the <100> and <111> grains are described separately.

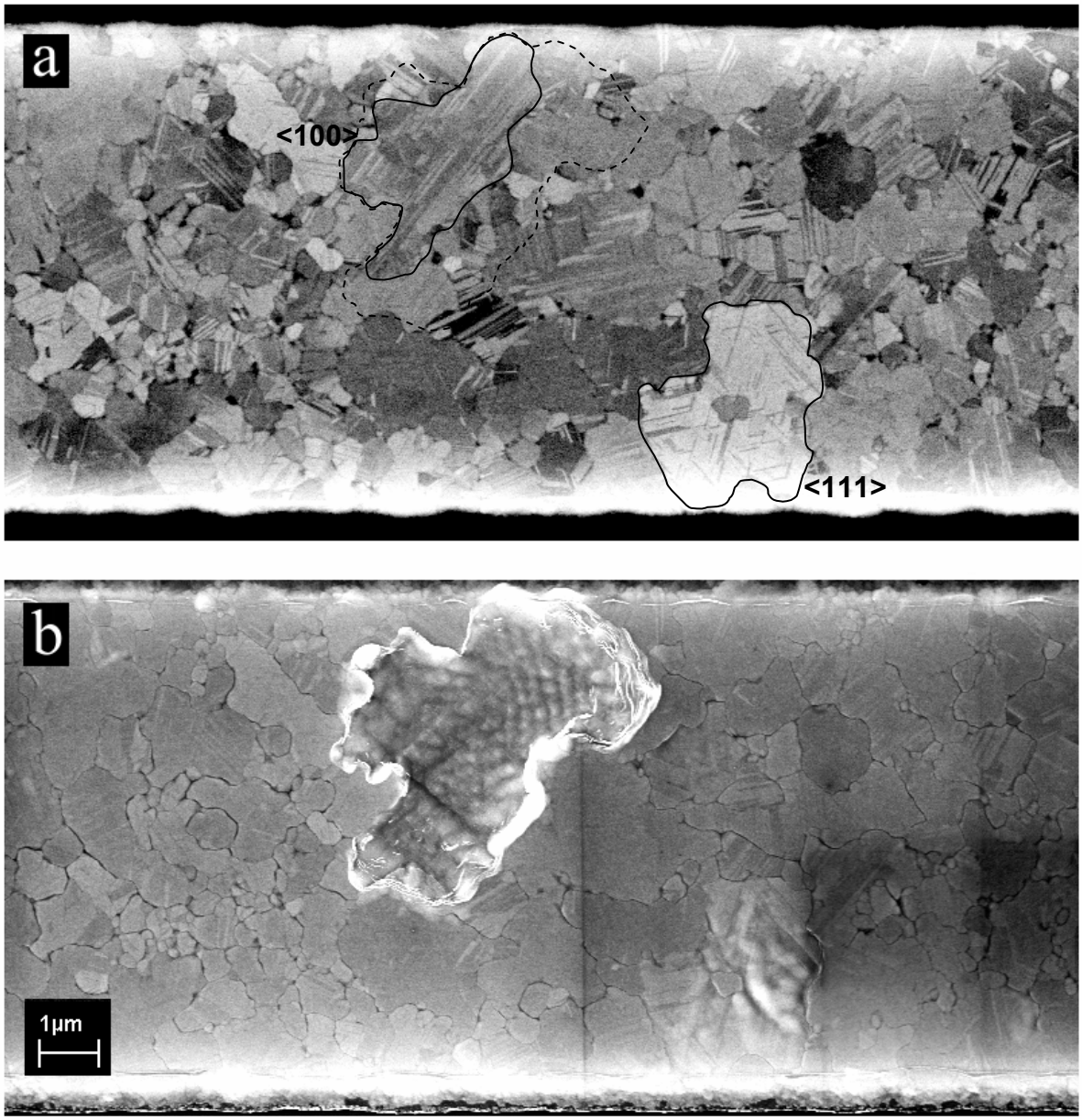

Fig. 4.2 Example of damage evolution in a 200 nm thick film on Si during fatigue testing at $\Delta T = 220$ K ($\Delta\varepsilon = 0.31\%$). (a) BSE image showing the microstructure before testing. A <100> grain (solid line) and the shape of the associated final damaged region (dashed line) are marked at the left of the image and a <111> grain is outlined at the right, (b) SE image of the damaged regions after 3.8×10^5 cycles.

4.3.1 Fatigue damage in <111> out-of-plane oriented grains

Fig. 4.3 shows a typical example of damage evolution in a <111> grain during fatigue testing. The microstructure of the relevant region is shown in Fig. 4.3(a) before testing. The first evidence of damage are some small valleys and ridges (indicated by an arrow in Fig. 4.3(b)) at the boundary to a neighboring <111> grain. During further testing, new valleys and ridges formed at the grain boundaries and next to one of the twin boundaries (indicated by the arrow in Fig. 4.3(c)). These wrinkles then spread out through the grain, while growing in amplitude. The grain boundaries were almost always effective in containing the spread of damage, but only some of the twin boundaries were effective, such as the one indicated by the arrow in

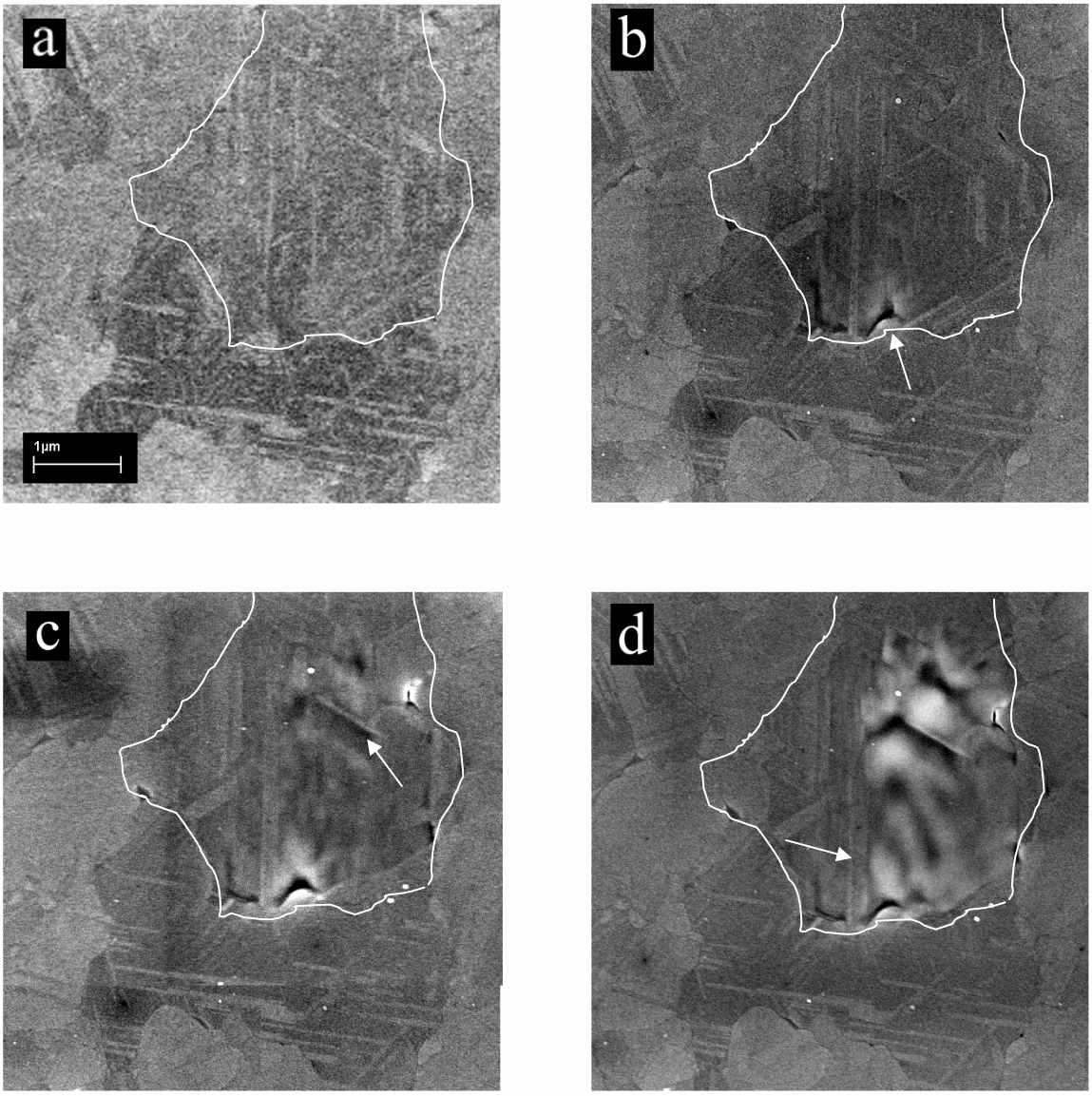

Fig. 4.3 Example of damage evolution in a <111> grain of a 200 nm thick film on Si during fatigue testing at $\Delta T = 170$ K ($\Delta\varepsilon = 0.24\%$). (a) The <111> grain is outlined, 0 cycles, (b) 2.4×10^5 cycles, (c) 3.8×10^5 cycles, (d) 5.0×10^5 cycles.

Fig. 4.3(d). Thus, throughout the tests the damage typically remained localized within a single grain, or within a part of a single grain. In a few rare cases, a neighboring grain was "infected" by the damaged grain and wrinkles spread into the new grain.

FIB cross-sections of several wrinkled regions showed that the ridge height was comparable to the film thickness and that the valleys often extended to the substrate. Typical spacings of the wrinkles were between 0.5 and 1.0 μm. The FIB cross-sections also revealed that there were no voids in the interface between the <111> grains and the Ta interlayer and that the Ta film remained intact.

The twins in the <111> grains were observed to play an important role in damage evolution. In addition to the formation of wrinkles next to twins, local thinning of the grains in the region of the twin lamellae was often observed. In a very few instances, the twin lamellae grew in width and consumed some of the matrix grain. Such a case was found for the twin lamella indicated by the arrow in Fig. 4.3(d), which grew somewhat during the test. Also, the density of twin boundaries within individual <111> oriented grains was important in damage development: lightly twinned grains required fewer temperature cycles to form damage than their heavily twinned counterparts. The lightly twinned grains often developed arrays of surface wrinkles parallel to one of the twin boundaries, whereas the heavily twinned grains exhibited a more disordered surface morphology.

Motivated by the influence of twins on the damage evolution in <111> grains, studies were also performed on Cu lines deposited on sapphire. These films were composed of twin-free, <111> out-of-plane oriented grains. A typical example of several damaged regions in a Cu line on sapphire is shown in Fig. 4.4. Damage was observed to form much more quickly (after fewer cycles) and at smaller temperature amplitudes than in the heavily twinned Cu samples fabricated on Si. For example, damage first appeared after $1x10^5$ cycles in the Cu on sapphire samples with a ΔT of 90 K, whereas a ΔT of 180 K was required to produce the same effect in the Cu on Si samples. In addition, the damage patches were more densely spaced on the sapphire substrates than on the Si substrates. The damage was confined within single grains and consisted of well-defined, parallel surface wrinkles with spacings of either 0.4 or 0.8 μm. The coarser wrinkles look very similar to the wrinkles observed in the low twin density grains in the Cu on Si samples. EBSD analysis of regions containing the finer wrinkles, showed that the wrinkles lay roughly parallel to <110> directions, consistent with them being generated at the intersection of {111} slip planes with the sample surface.

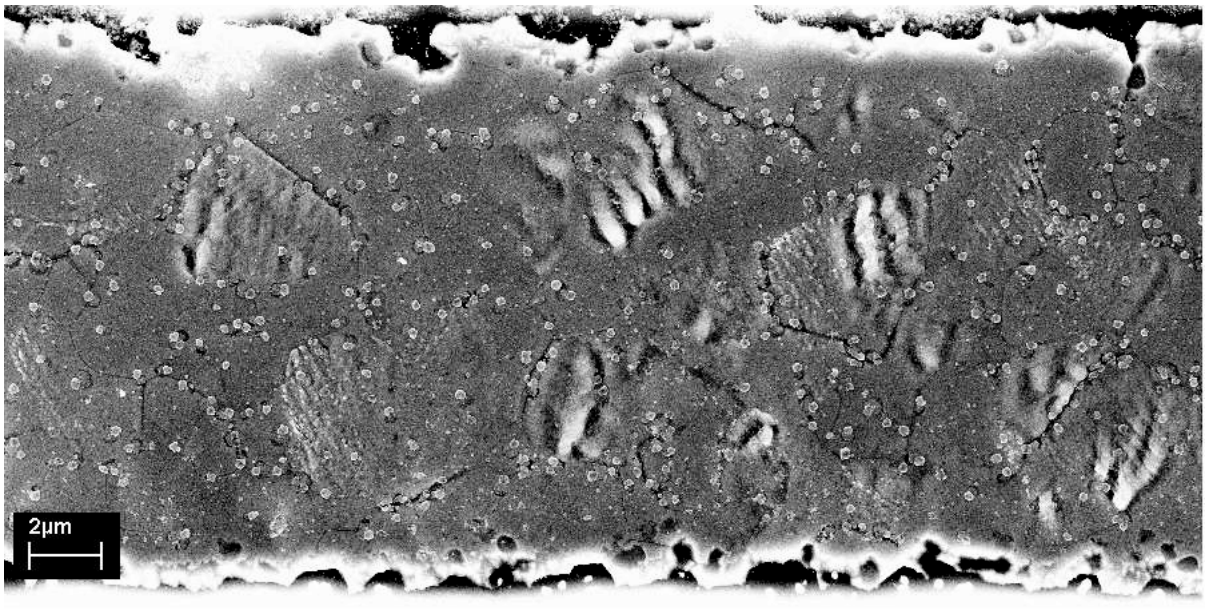

Fig. 4.4 Damage patches in a 300 nm thick Cu on sapphire sample after 1.1×10^5 cycles at $\Delta T = 90$ K ($\Delta\varepsilon = 0.11\%$). The rough line edges and the particles at the surface are artefacts of the sample preparation process.

4.3.2 Fatigue damage in <100> out-of-plane oriented grains

The first sign of damage in the <100> grains was the shrinkage of twins. An example of this is illustrated in Fig. 4.5. A number of the twin lamellae, including the twins indicated with arrows in Fig. 4.5(a) either partially or completely dissolved during the early stages of testing, as can be seen by comparing Fig. 4.5(a) with Fig. 4.5(c). In Fig. 4.5(c), the first evidence of wrinkles near the grain boundaries appeared (indicated by arrows).

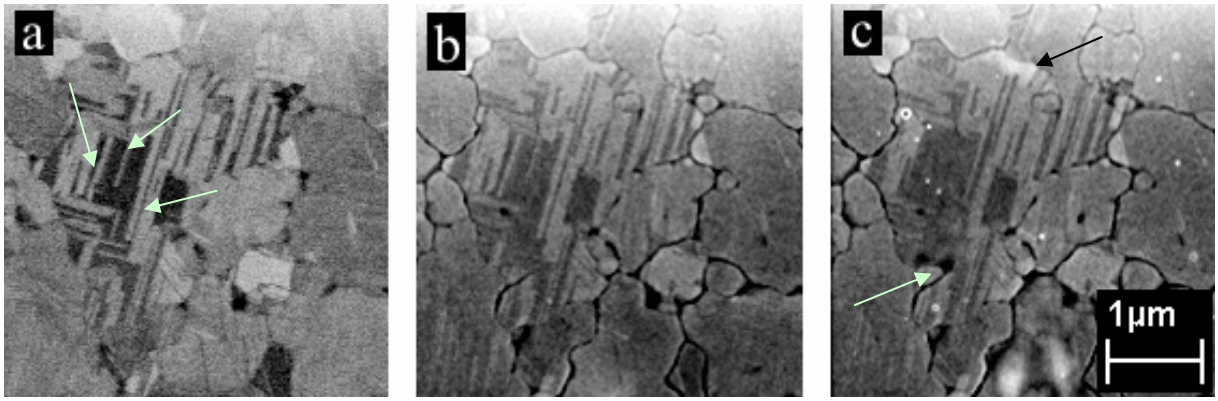

Fig. 4.5 Evidence for twin shrinkage in a <100> oriented grain of a 200 nm thick Cu film on Si during fatigue testing at $\Delta T = 210$ K ($\Delta\varepsilon = 0.29\%$). (a) 0 cycles, (b) 8.1×10^5 cycles, (c) 1.4×10^6 cycles.

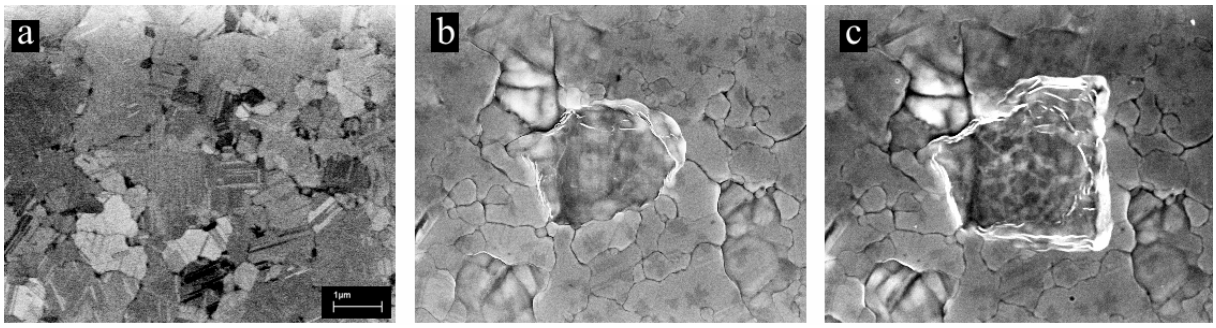

Fig. 4.6 Grain growth in a <100> oriented grain of a 200 nm thick film during fatigue testing at $\Delta T = 190$ K ($\Delta\varepsilon = 0.27\%$). (a) 0 cycles, (b) 3.23×10^6 cycles, (c) 3.58×10^6 cycles.

From this point on, twin dissolution was accompanied by the spread of small amplitude surface wrinkles throughout the grain and by grain thinning. Once the twins had partially or completely dissolved, the damaged grain started to grow by consuming the neighboring grains. The early stages of grain growth are illustrated in Fig. 4.6. The damaged grain, which exhibited large ridges at the grain boundaries and thinning in the interior of the grain, grew rapidly during fatigue testing and took on a faceted shape at the early stages of growth (Fig. 4.6(c)). A similar example is also seen in Fig. 4.2 where the faceted damaged region (Fig.4.2(b)) extends beyond the original boundaries of the <100> grain (Fig. 4.2(a)). As the grains continued to grow, the facets also evolved, typically becoming longer and sharper, with angles meeting at 90°. Eventually they attained a rectangular shape and often reached a size comparable to or somewhat larger than the line width (Fig. 4.7(a) and Fig. 4.8(a)). In some cases, the damaged regions even grew extrusions out beyond the side of the line. In the late stages of damage evolution, the wrinkles grew in amplitude while new

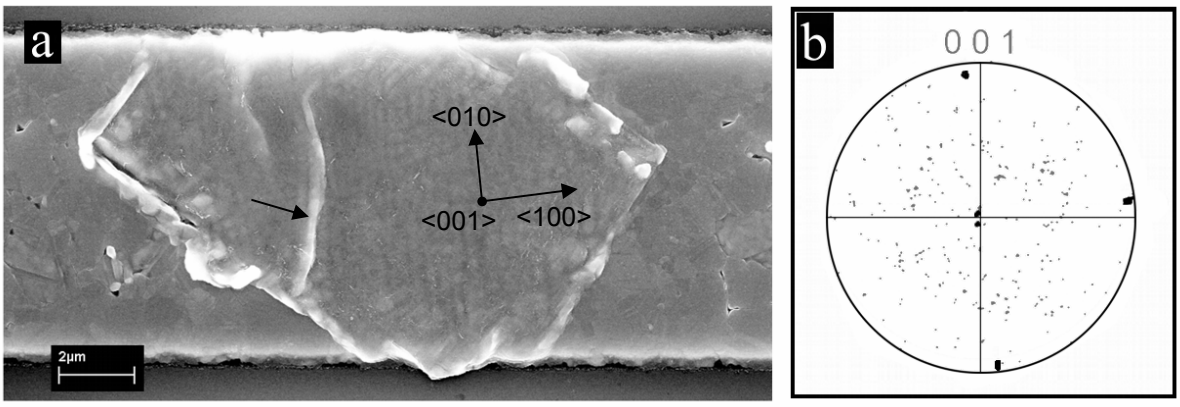

Fig. 4.7 (a) Rectangular shaped <100> oriented damaged region in a 300nm thick film after 8.4×10^5 cycles at $\Delta T = 180$ K ($\Delta\varepsilon = 0.25\%$). A low angle grain boundary in the damaged region is marked with an arrow. (b) Pole plot obtained from EBSD mapping of this area showing the orientations of the two sub-grains composing the damaged region (large black dots). The small grey dots correspond to the orientations of the grains surrounding the damaged region.

wrinkles formed, leading to a highly structured, complex surface (Fig. 4.8(b)).

EBSD investigations of these large faceted damage regions revealed important crystallographic information:

- The damaged regions are composed of single, twin-free grains (or several twin-free sub-grains) and have maintained their <100> out-of-plane orientation. For example, the damage patch shown in Fig. 4.7(a) is composed of two large <100> out-of-plane oriented grains separated by a low angle grain boundary.
- Investigations of the in-plane orientations of the damaged <100> grains show that they often have a <100> crystallographic direction lying roughly between 5° and 10° of the line direction. This is illustrated, for example, by the pole plot in Fig. 4.7(b) showing the orientations of the two sub-grains from Fig. 4.7(a).
- The grain boundary facets lie parallel to <110> directions of the damaged grains and have a preferred orientation relative to the line direction. Fig. 4.9 shows a summary of the angles between the facets of the rectangular grains and the line direction for all of the rectangular-shaped damaged regions that were observed. The most frequent orientation lies between 35° and 40°.
- The damaged <100> grains often contain parallel surface wrinkles as illustrated in Fig. 4.8. Except in the late stages of damage, these wrinkles lie roughly parallel to <100> directions in the grain and also perpendicular to the line direction (Fig. 4.8(a)). During further testing, the large region of parallel wrinkles is replaced by smaller regions with wrinkles of different orientations (Fig. 4.8(b)). EBSD measurements show that this process is accompanied by the break up of the large <100> grains into a number of smaller sub-grains.

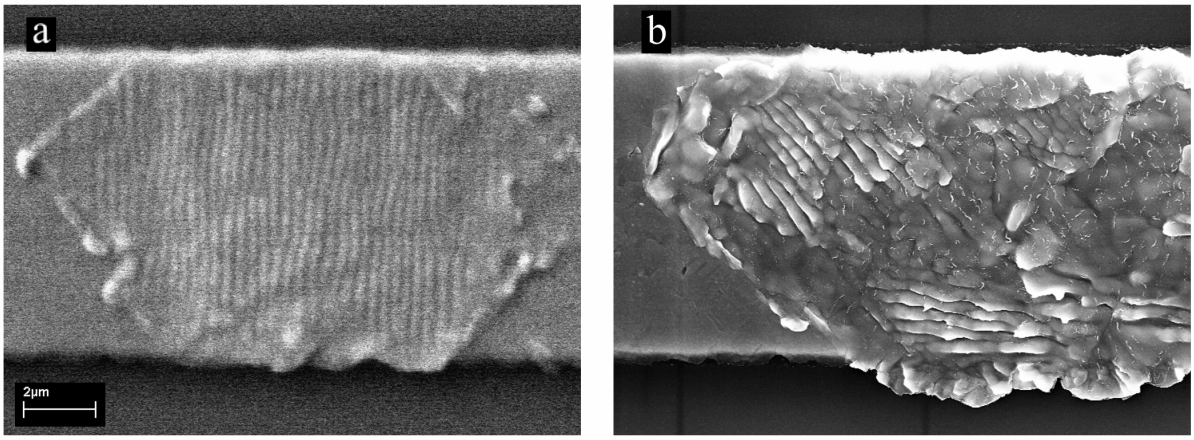

Fig. 4.8 Rectangular shaped <100> oriented damaged region in a 300 nm thick film after (a) 3.1×10^5 cycles at $\Delta T = 170$ K ($\Delta\varepsilon = 0.24\%$) followed by 3.9×10^5 cycles at $\Delta T = 145$ K ($\Delta\varepsilon = 0.20\%$), (b) with an additional 17.6×10^5 cycles at $\Delta T = 145$ K ($\Delta\varepsilon = 0.20\%$).

Several damaged regions were investigated using FIB cross-sections and the wrinkle spacings and amplitudes were observed to lie between 200 and 400 nm, which are somewhat smaller than those observed in the <111> grains. The large ridges at the grain boundaries had heights of roughly 500 nm. The FIB cross-sections also revealed that there were no voids in the interface between the <100> grains and the Ta interlayer.

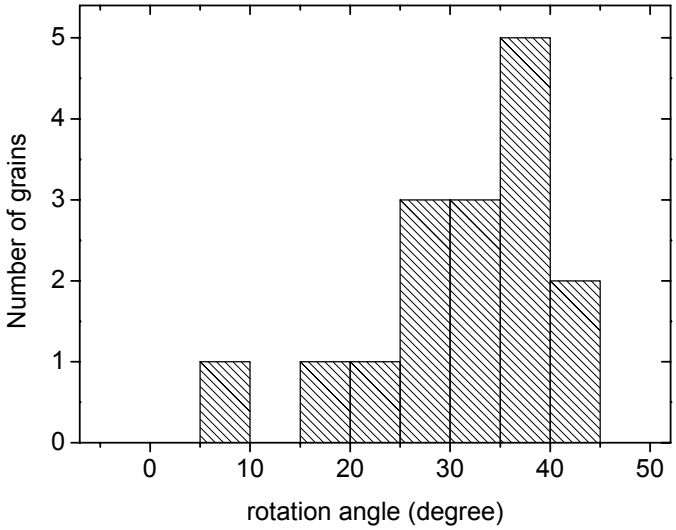

Fig. 4.9 Number of rectangular shaped <100> grains versus angle of the grain boundary facets relative to the line direction.

4.4 Discussion

Fatigue of bulk Cu at room temperature is usually attributed to dislocation glide processes. As the testing temperature is increased, diffusion processes play a more important role and noticeable time-dependent phenomena are observed at temperatures in excess of half the melting temperature. The experiments presented here were all performed at less than half the melting temperature of Cu ($T_m/2$ = 679 K), where dislocation glide and dislocation interactions are still expected to dominate the fatigue process. However, in the case of small scale structures, diffusion may play a more important role than in bulk materials for two reasons. First, dislocation nucleation and motion are hindered in crystals with small dimensions [Nix 1989, Thompson 1993, Arzt 1998, Keller et al. 1999, Baker 2001, Baker et al. 2001, Hommel and Kraft 2001, v. Blanckenhagen 2002, Balk et al. 2003]. Second, boundary diffusion processes are expected to play a much larger role in small structures since the boundary area per unit volume (including free surfaces, interfaces, and grain and twin boundaries) is much larger than in large-grained, bulk specimens. These two effects increase the role of boundaries in fatigue of fine-grained, thin film samples relative to their coarse-grained counterparts.

In the following, the stress state in the Cu lines and various features of the damage evolution will be discussed in detail. Emphasis will be placed on possible contributions from dislocation glide and interface diffusion.

4.4.1 Mechanical stresses and strains in the samples

During fatigue testing, the thermal cycles in the line generate cyclic strains due to the difference between the thermal expansion coefficients of the film and substrate, $\Delta\alpha$. For a continuous film on a thick substrate, a temperature change ΔT produces an equibiaxial in-plane strain in the film of $\Delta\varepsilon = \Delta\alpha\Delta T$. For example, a temperature range of $\Delta T = 100$ K produces a strain range of 0.14% in the Cu on Si samples and a strain range of 0.12% in the Cu on sapphire samples. If the total strain range is large enough, large stresses are generated in the grains of the film which may lead to dislocation motion and/or atom transport. For example, at sufficiently large strains, the resolved shear stresses on the slip systems in the film exceed a critical stress and dislocation motion occurs, which under cyclic conditions can cause the formation of fatigue damage.

The local stresses that occur in the individual grains of a film are determined by the grain orientation as well as by grain-grain interactions. Large interaction stresses can be expected in samples where the grain size is small relative to the film thickness [Baker et al. 2001]. In samples such as the ones studied here, where the grain size is large compared to the film thickness, the contribution from grain-grain interaction stresses is small and the stress in each grain is predominately determined by its orientation. Because of elastic anisotropy, the stresses generated by equibiaxial in-plane strains are expected to differ with grain orientation.

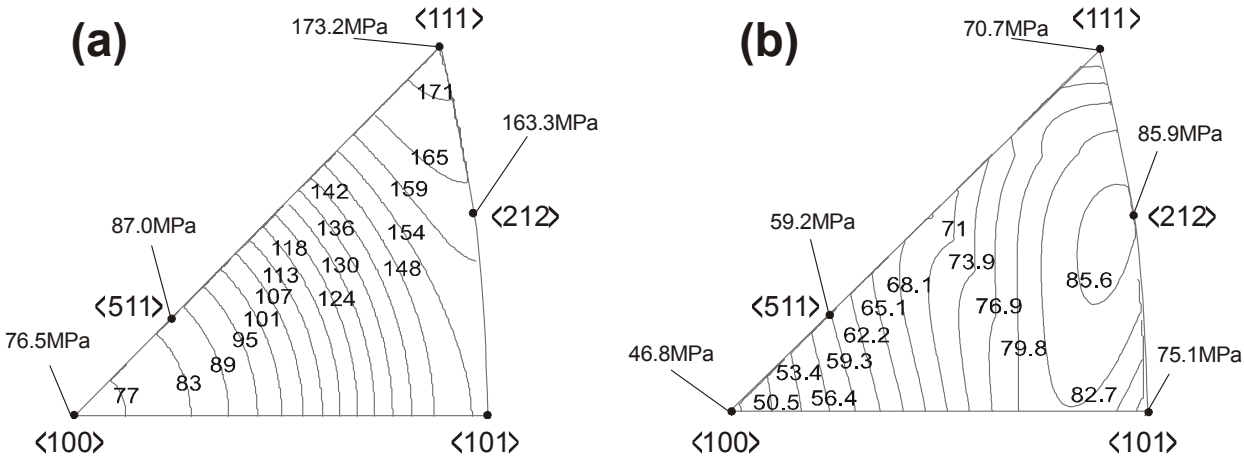

Fig. 4.10 (a) Hydrostatic stress as a function of out-of-plane grain orientation in Cu due to an equibiaxial in-plane strain of 0.1% and zero out-of-plane stress and (b) maximum resolved shear stress for dislocation glide under these conditions. The values for the <100> and <111> orientations and their respective twins, <212> and <511>, are indicated.

For example, the in-plane stresses generated by a temperature change in <100> grains of Cu thin films are significantly smaller than in <111> grains due to the differences in the biaxial modulus [Baker et al. 2001, Hommel and Kraft 2001]. The <100> and <111> orientations are special in that an equibiaxial in-plane strain creates an equibiaxial in-plane stress. For other grain orientations, an equibiaxial strain creates anisotropic in-plane stresses.

The determination of the stress state in a grain of any given orientation on a substrate is not available in the literature and requires a complex algebraic calculation. Such a calculation has been performed using the code Mathematica, for the case of a Cu film under an applied biaxial in-plane strain and zero out-of-plane stress (an annotated Mathematica notebook for the calculations can be found in Appendix A). The calculated hydrostatic stresses in a Cu film are shown in Fig. 4.10(a) as a function of the out-of-plane grain orientation. Since there are no out-of-plane stresses in a thin film, for a given applied strain the hydrostatic stress is proportional to the average in-plane stress, and to the biaxial modulus for the special cases of the <100> and <111> orientations. The hydrostatic stresses are minimum in <100> out-of-plane oriented grains and maximum in the <111> grains, consistent with the fact that the biaxial modulus for the <100> orientation is smaller than for the <111> orientation.

The resolved shear stresses for dislocation glide in Cu under an applied biaxial in-plane strain (and zero out-of-plane stress) were also calculated using the algebraic model (Appendix A). The maximum resolved shear stresses are plotted in Fig. 4.10(b) as a function of the out-of-plane grain orientation. The smallest resolved shear stresses occur in grains with a <100> out-of-plane orientation and the largest resolved shear stresses occur at an orientation near the <212> out-of-plane orientation (which is the first generation twin of <100>). The fact that the resolved shear stresses are larger in the <111> grains than the <100> grains for a given applied strain means that the <100> grains can be exposed to larger strains than the <111> grains, before a critical resolved shear stress is reached and dislocation glide is possible. Nonetheless, even though the strains in the <100> grains are larger when plasticity sets in, they will have smaller hydrostatic stresses under both elastic and plastic loading conditions.

A continuous Cu film on an isotropic substrate experiences equibiaxial strains during temperature cycling, but this is not the case in lines with finite width. In order to estimate the deviation from a purely equibiaxial strain state, a two-dimensional, plane strain, finite element simulation of the line cross-section (10 μm wide, 300 nm thick) on a thick substrate was performed under the assumption of perfect isotropic elasticity (Appendix B). The analysis

showed that the stress state induced in the line by a temperature change was close to equibiaxial near the line center but that both in-plane stress components were reduced very near the line edges, particularly the component lying across the width of the line. At the center of the lines, the ratio of the stress along the line to the stress across the width was 0.94 for Cu on Si and 0.98 for Cu on sapphire (compared to a ratio of 1.0 for a homogeneous, isotropic film). The effect of the finite line width on the anisotropy of the stress state was smaller for the Cu on sapphire case, presumably due to the higher elastic constants of the sapphire in comparison with Si. Although the deviation from a pure biaxial stress state is sufficiently small to justify using continuous film data to understand qualitative features of the stress behaviour in the lines, it may still be large enough to have a significant effect on the active systems for dislocation glide.

4.4.2 Fatigue damage

4.4.2.1 Higher Damage Susceptibility of <100> Grains

The results have shown that <100> grains form damage more easily (i.e. lower cycle numbers and lower temperature ranges) than <111> grains. This suggests that the accumulated plastic strain is larger in the <100> grains than in the <111> grains for the same total strain. However according to Fig. 4.10, the resolved shear stresses are smallest in the <100> grains and they should experience the smallest plastic strains for a given applied total strain. Therefore, straightforward considerations of the ease of dislocation glide for different grain orientations cannot explain the observations. One could argue that the effect is due to a difference in grain size or twin boundary density in the two different texture components [Thompson and Backofen 1971, Keller et al. 1999, Baker et al. 2001, Hommel and Kraft 2001], but microstructural studies do not support this. Instead, it will be argued in Section 4.4.2.3 that the twin boundaries play completely different roles in the two different texture components. Namely, the twin boundaries in <111> grains are believed to block dislocation motion, whereas the twins in <100> grains are not so effective at blocking dislocation motion. This reduces the constraint on dislocation motion in <100> grains resulting in more plastic strain and faster damage formation.

A further possible explanation for the difference in damage susceptibility in the texture components comes from a consideration of the resolved shear stresses in the twinned regions of the grains. The calculation of the resolved shear stresses in Fig. 4.10(b) shows that the largest stresses occur in grains with an out-of-plane orientation close to <212>, which is the

orientation of the first generation twin of the <100> grains. Thus, although the <100> grains have the smallest resolved shear stresses, their twins experience very large resolved shear stresses – larger than any of the stresses present in <111> grains and their twins – and may therefore be the first to develop damage under fatigue testing.

A clear preference for damage formation in <100> grains relative to <111> grains has also been observed in fatigued Ag films [Schwaiger and Kraft 2003] and to a lesser extent in fatigued Cu films on polyimide substrates [Kraft et al. 2002]. These tests were performed at room temperature under approximately uniaxial loading conditions with larger strain amplitudes than used here. Damage appeared as extrusions and intrusions at the grain surfaces and as voids at the film/substrate interface. Just as for the case presented here, calculations of the resolved shear stresses could not explain the increased susceptibility to fatigue damage of <100> grains relative to <111> grains. Instead, an argument was proposed based on the fact that the Burgers' vectors of the active glide systems of the <111> grains lie in the plane of the film, in contrast to the <100> grains. Under uniaxial loading conditions, the dislocations with the largest resolved shear stresses in the <111> grains leave pure screw misfit segments at the film/substrate interface. The interaction of these segments cannot generate the vacancies necessary for voids and fatigue damage in the <111> grains. However, in the samples tested here under biaxial loading, the stress calculations (Appendix A) reveal that the slip systems with the largest resolved shear stresses in both the <100> and <111> grains have Burgers' vectors with out-of-plane components (Appendix A), so this explanation is not applicable here.

The stresses measured in <100> grains during monotonic plastic straining of Cu thin films are also lower than expected, based on the biaxial modulii and Schmidt factors in these grains. Both thermally cycled Cu films on Si [Baker et al. 2001] and uniaxially strained Cu films on polyimide [Hommel and Kraft 2001] exhibit this difference. Several explanations have been proposed for the discrepancy, such as differences in grain size distributions of the two texture components or grain-grain interactions, but none of them can account for all of the experimental observations. It is possible that the explanations proposed here, based on resolved shear stresses in the twins and the effectiveness of twins in blocking dislocation motion, could account for the observed behaviour in these studies.

The importance of twin boundaries in affecting fatigue damage formation may also account for the much higher susceptibility of the Cu films on sapphire to damage formation than the Cu films on Si. The <111> grains on sapphire are twin-free whereas the <111> grains on Si are heavily twinned. However, there are other important differences between the Si and

sapphire samples that may contribute to the observed differences in fatigue behaviour. In particular, heteroepitaxial interfaces (Cu on sapphire) and crystal/amorphous interfaces (Cu on oxidized Si) are known to have very different interactions with dislocations [Dehm and Arzt 2000, Dehm et al. 2002].

4.4.2.2 Surface wrinkles

Thermomechanical loading of the Cu thin films led to the formation of wrinkles at the surface of the damaged grains. The formation of surface features is a general phenomenon in cyclically deformed metals. In bulk Cu, extrusions and intrusions form where slip bands and vein structures intersect the specimen surface and typically lie parallel to the primary glide plane [Basinski and Basinski 1992]. In Cu thin films mechanically fatigued at room temperature [Kraft et al. 2002], similar extrusions and intrusions also form, but there is no evidence for dislocation structures such as slip bands and veins [Schwaiger et al. 2003, Zhang et al. 2003]. A model has been proposed for the formation of extrusions and intrusions based on the motion and interaction of individual dislocations in thin films [Schwaiger and Kraft 1999, Kraft et al. 2002]. The wrinkles observed here in the thermally fatigued Cu thin films are smoother and more periodic than the extrusions and intrusions in bulk Cu and thin Cu films fatigued at room temperature. In addition, the wrinkles do not always lie parallel to {111} planes. Therefore it is possible that they are formed by a different mechanism than the extrusions and intrusions.

During the early stages of damage formation, wrinkles form close to grain and twin boundaries in both the <100> and <111> oriented grains. Grain boundaries [Baker et al. 2001] and twin boundaries [Sekiguchi et al. 2001] are known to be regions of high stress in Cu thin films, because of anisotropic elastic properties. Local stress concentrations near these boundaries may promote the formation of surface wrinkles either by dislocation glide or surface and boundary diffusion. Numerous TEM observations show that grain and twin boundaries are often sources for dislocations, making it more likely that the first evidence of dislocation motion would appear in the neighborhood of these boundaries. Similarly, due to the fact that grain boundaries and incoherent twin boundaries are good diffusion paths, the boundary regions are expected to show the strongest evidence of diffusional motion. For instance, the fact that the grain boundaries are good diffusion paths is supported by the grain boundary grooves observed on the surface of the samples during testing (see for example, Fig. 4.2, Fig. 4.6, and Fig. 4.7).

During further testing, the wrinkles spread out through the grains. In <111> grains with low twin densities or no twins (Cu on sapphire), the wrinkles form at the surface along

<110> directions. These directions lie parallel to slip planes. It is possible that these wrinkles form by the interaction of dislocations on a single slip plane by the same mechanism proposed for the formation of extrusions and intrusions in thin films at room temperature [Schwaiger and Kraft 1999, Kraft et al. 2002]. The fact that the features are smoother at elevated temperatures is possibly due to enhanced surface diffusion. In contrast, in the <100> grains, periodic surface wrinkles are formed parallel to <100> directions. To our knowledge, there is nothing reported in the fatigue literature about the formation of surface structures parallel to <100> directions. However, labyrinth dislocation structures often form in bulk materials with multiple active slip systems and have walls parallel to <100> planes [Jin and Winter 1984]. It is conceivable that the <100> surface wrinkles in the thin films might be the result of dislocation structures which have similar origins as the labyrinths of bulk specimens. Although their exact evolution in bulk materials is not known, labyrinths presumably are the result of dislocation reaction products formed by multiple slip. No extended dislocation structures like walls or PSBs were observed in the Cu films and preliminary plan-view TEM results [Zhang 2003] confirm the absence of any extended dislocation structures but show localized dislocation debris lying along <100> in-plane directions. This debris may consist of dislocation interaction products, such as sessile jogs and Lomer-Cotrell locks [Cheng and Laird 1981, Jin and Winter 1984]. Arrays of such dislocation interaction products might give rise to the periodic surface wrinkles either by repetitive emission of dislocations that leave steps at the surface of the film or by the generation of point defects such as vacancies which cause local thinning. Within this scenario, the fact that the wrinkles lie preferentially along the <100> direction closest to perpendicular to the line direction, might be explained by the fact that the strains imposed on the line are not purely equibiaxial.

4.4.2.3 Influence of twins

A number of observations point out the importance of twins in the development of damage. One of the most intriguing of these is that the formation of the first wrinkles is accompanied by twin shrinkage in the <100> oriented grains, whereas twins mainly serve to block the spread of damage in the <111> oriented grains. A possible explanation for this can be found by considering the dislocation-twin boundary interactions in the two different grain orientations. Dislocations can be *directly* transmitted across twin boundaries only if the active slip planes of the matrix and the twin crystals intersect in a line at the twin boundary. If in addition, the slip systems have the same Burgers' vectors, the only barrier to this process is the necessity of cross-slip at the boundary. If the Burgers' vectors in the matrix and the twin are different, residual dislocations must be deposited at the boundary but transmission is still

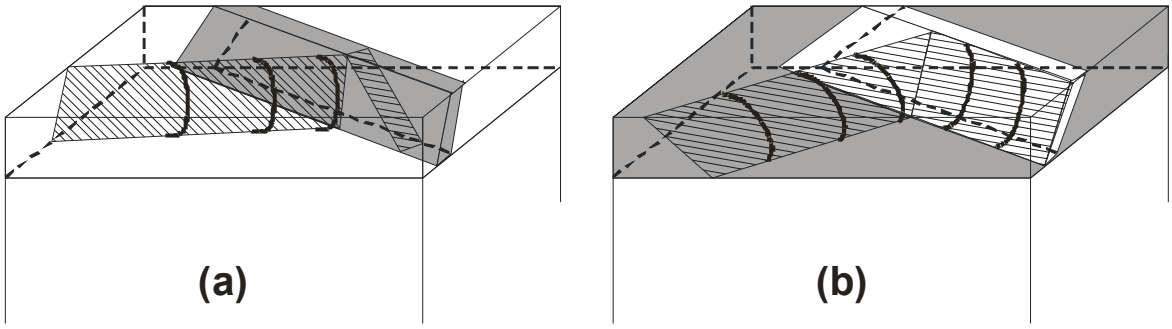

Fig. 4.11 Schematic drawing of the active glide systems in Cu films on a substrate, showing that (a) indirect transmission is required between a <111> grain and its twin, and (b) direct transmission is possible between a <100> and its twin.

possible. If the residual dislocation can split into Shockley partial dislocations, they can move along the twin boundary and result in twin growth or shrinkage. Matrix and twin slip systems that do not intersect along a common line in the twin boundary require *indirect* transmission and generally have much larger energy barriers. Such boundaries are expected to block further motion of dislocations in most cases.

In considering the details of dislocation-twin boundary interactions in the <100> and <111> out-of-plane oriented grains, it is assumed that the twin boundaries are coherent {111} boundaries. This assumption certainly affects any details of dislocation-twin boundary interactions, but since the exact crystallography of the twin boundaries in these samples is not known, this is a reasonable assumption in an initial approach to the problem. The approach consists of looking at the ease of transmission of dislocations through the twin boundaries on the slip systems with highest resolved shear stresses. The calculation of the resolved shear stresses summarized in Fig. 4.10(b) (Appendix A), reveals that there are 8 active slip systems in a <100> out-of-plane oriented grain, 6 in a <111> grain, and 2 in each of the twin orientations. In comparing the slip systems in the matrix and twins it is found that *direct* transmission between some of the active slip systems of the <100> matrix and the <212> twin is possible whereas only *indirect* transmission is possible between <111> and <115>. This means that twins in <111> grains will be more effective in blocking dislocation motion than in <100> grains (Fig. 4.11).

Interestingly, the slip systems with the highest resolved shear stresses in the <212> twins lie parallel to the twin boundary. This fact, combined with observations that twin boundaries are a major source for dislocations in plastically deformed Cu [Flinn et al. 2001] suggests that it might be energetically feasible for the twin boundaries to act as nonregenerative sources for dislocations (nonregenerative sources are changed by the emission of dislocations and can eventually be “used up”; regenerative sources – such as Frank-Read sources – can continue to emit dislocations indefinitely): It is possible that a

nucleation event at the twin boundary could create a loop composed of a dislocation on one of the active slip systems in the matrix material and a dislocation lying in the twin boundary. If the dislocation in the boundary then splits into two Shockley partials, their motion can result in twin shrinkage. Accumulated plastic strain in <100> grains would then lead to the disappearance of twins.

4.4.2.4 Grain growth and faceting

One of the most curious aspects of the fatigue damage process is the growth of large, twin-free, facetted <100> grains. This selective grain growth is likely caused by the deformation introduced by fatigue loading, since it occurs in microstructures that had previously been stabilized by annealing at elevated temperatures. Grain growth as a result of deformation is a fairly general phenomenon in metals and is driven by the stored energy of deformation. For example, grain coarsening of unannealed Cu with an initial grain size of 250 nm has been observed due to fatigue testing [Höppel et al. 2002]. Both growth of individual grains in a stagnant matrix and uniform grain coarsening were observed. In neither case was faceting of the grains observed. Grain growth has also been observed during fatigue experiments at elevated temperatures in a number of different polycrystalline bulk metals and has even been observed to lead to rectangular-shaped grains [Williams and Corti 1968, Wigmore and Smith 1971, Snowden et al. 1976, Snowden 1981]. However, in contrast to the results obtained here where only the damaged grains grew, the bulk samples exhibited fairly uniform grain growth during cyclic loading and only at higher homologous temperatures than used here. In addition, the facets observed in the rectangular-shaped grains of the bulk fatigued samples lie along the directions of maximum shear stress and were not specific crystallographic directions.

The grain growth that has been observed during thermal fatigue of the Cu thin films differs significantly from the literature. The distinct features of the phenomenon are:

- grain growth occurs in a microstructure previously stabilized by annealing
- only the <100> out-of-plane oriented grains grow,
- only grains exhibiting surface damage grow
- the growing grains form facets that are parallel to their <110> directions
- the grain facets (and the in-plane grain orientation) have a preferred orientation relative to the line direction

At this time, a comprehensive model for all of these features has not been developed. However, plausible explanations can be proposed that can account for many of them.

The fact that grains grow during fatigue in a microstructure that has previously been stabilized at elevated temperatures, requires that fatigue loading somehow generates large driving forces for grain growth and increases the grain boundary mobility. The enhanced mobility of the boundaries of the deforming grains under fatigue loading, could be explained by an idea often discussed in the literature [Gleiter 1969, Rae and Smith 1980, Sutton and Baluffi 1995], that boundary mobility is significantly enhanced by a flux of dislocations and point defects to and from the grain boundaries. A possible driving force for grain growth under fatigue loading could plausibly come from changes in the elastic strain energy or stored energy of deformation of the deforming grain relative to its neighbors. This might result from cyclic softening of the deforming grain, or from less cyclic hardening than in its neighbors.

The <110> grain boundary facets of the growing grains are consistent with faceting on a {111} plane. <111> faceting is often observed during crystal growth, as for example in several studies of recrystallization of Al, where grains growing into a fine-grained polycrystalline or deformed single crystal matrix have large <111> facets [Gastaldi and Jourdan 1981]. Formation of <111> facets during growth can be explained with models for grain growth [Gleiter 1969, Rae and Smith 1980, Sutton and Baluffi 1995] where the boundary mobility is determined by the motion of defects, such as ledges and kinks, at the surfaces of the grains forming the boundary. For a grain with a boundary almost parallel to its {111} plane, there is only a small number of ledges and kinks where atoms can be added. As a result, the grain boundary mobility is controlled by the number of these sites and is independent of the orientation of the neighboring grain or grains, as long as the neighboring grain boundaries have higher densities of ledges and kinks. FIB cross-sections of the large facetted grain boundaries of the fatigued Cu films, reveal that many of the boundaries have an in-plane inclination deviating from a perfect <111> orientation. Interestingly, such a model for grain growth predicts that a flux of dislocations and point defects to the nearly crystallographically perfect grain boundary would significantly enhance its mobility.

That <100> grains are more susceptible to damage formation than <111> grains has already been discussed (Section 4.4.2.1). One possible explanation for this is that damage is initiated in the highly stressed <212> twins initially present in the <100> grains. However, not every <100> grain grows under fatigue loading – only those that experience extensive deformation. Insight into which <100> grains deform and grow, comes from the preferred in-plane orientation of these grains, as evidenced by the inclination of their facets to the line direction (Fig. 4.9). The facets are preferentially inclined at angles between 35° and 40° to the line direction, which corresponds to an in-plane inclination between 5° and 10° of the <001>

direction to the line direction. As discussed in Section 4.4.1, non-equibiaxial strains are expected in finite width lines. To account for this, a small uniaxial strain component was introduced in the calculation of the resolved shear stresses (Appendix B). The results show, that the twins of the <100> out-of-plane oriented grains experience the largest resolved shear stress when the in-plane <100> direction of a <100> grain is rotated 8.2° away from the line direction. This is consistent with the preferred orientation of the facets (Fig. 4.9) and further supports the idea that damage formation in <100> grains is initiated by the twins.

4.5 Summary and Implications

The evolution of damage in the individual grains of thermally fatigued Cu thin films has been investigated as a function of microstructure and crystallographic orientation. Complex damage processes have been observed which depend strongly on grain orientation and have been discussed in terms of mechanisms involving dislocation glide and the interaction of dislocations with twin and grain boundaries. The observations and results of these considerations can be summarized as follows:

1. Fatigue testing of 200 and 300 nm thick Cu films results in damage formation in both <100> and <111> out-of-plane oriented grains. The <100> grains are more susceptible to damage formation than the <111> grains, which is attributed to the easy initiation of damage at the highly stressed twins in the <100> grains. Both orientations develop surface wrinkles, but otherwise the damage evolution and morphology is distinct for the two orientations.
2. The <111> oriented grains develop surface wrinkles that are likely formed by repetitive dislocation slip and dislocation interaction on a primary slip system. This mechanism is also active in fatigued bulk Cu and room temperature fatigued Cu films. However, due to the small crystal volume, no extended dislocation structures are formed in the thin films. The surface wrinkles are similar to the extrusions and intrusions observed in bulk Cu and room temperature fatigued Cu films, except that they are smoother, presumably due to surface and interface diffusion at the somewhat elevated temperatures.
3. The <100> oriented grains exhibit extremely complex behaviour, including twin dissolution, the formation of surface wrinkles along <100> directions, and facetted grain growth. Such behaviour is novel and has not been observed in bulk Cu fatigued at any temperature or in Cu films fatigued at room temperature. A consistent picture of

these diverse phenomena is obtained by considering the influence of boundaries and interfaces on dislocation glide: Due to the large shear stresses in the twins of the <100> grains, the twin boundaries act as nonregenerative sources for dislocations. The surface wrinkles are formed by dislocation reaction products left behind by multiple slip. The facetted grain growth is made possible by enhanced grain mobility caused by the fatigue-induced flux of dislocations and point defects to the boundaries. And the driving force for grain growth comes from changes in the stored energy in the deforming grains relative to their neighbors during fatigue.

4. The differences between the damage evolution in the <100> and <111> grains are best explained by considering the active slip systems for dislocation glide. These reveal that the transmission of dislocations through twin boundaries is possible in <100> grains but not in <111> grains.

In summary, this study of thermal fatigue in Cu thin films has revealed new types of fatigue damage. The novel damage formation is attributed to the increased interaction of dislocations with boundaries and interfaces, and is presumably caused by the higher density of interfaces and the absence of extended dislocation structures in the thin films. In future studies, careful TEM investigations of dislocations in the fatigued films and their relation to the surface damage could be very fruitful and might serve as a test of the damage evolution models proposed here.

5 Size Effects in High Cycle Thermal Fatigue Failure of Cu Thin Films

5.1 Introduction

Fatigue is one of the most common failure mechanisms in metals. During fatigue, damage forms, propagates, and eventually causes mechanical failure of the sample, even at cyclic loads below those causing yield under monotonic loading. In order to optimise performance and assess the reliability of various metal components, tests to determine the number of cycles to failure – the so-called "fatigue life" – are performed. The study of fatigue life has lead to the identification of trends in fatigue and helped in the development of phenomenological descriptions for fatigue failure. In particular, it has been found that grain size refinement is a very effective method to extend the fatigue life of bulk metals. This improvement in fatigue life is attributed to the inhibition of fatigue damage formation in small dimensions: the small volume of the grains leads to increased interaction of dislocations with the grain boundaries and decreased interaction with the extended dislocation structures formed during fatigue loading [Thompson and Backofen 1971, Lukáš and Kunz 1987].

Fatigue studies have recently been extended to thin metal films [Read 1998, Kraft et al. 2001, Kraft et al. 2002, Zhang et al. 2003] and ultra-fine-grained metals [Agnew et al. 1999, Vinogradov and Hashimoto 2001, Höppel et al. 2000, Thiele et al. 2002]. Small scale metal structures and ultra-fine-grained metals are presently in use or planned for use in applications such as microelectronic and microelectromechanic devices, where they often experience extreme thermomechanical conditions during use. It is well-known that dislocation activity is inhibited by small grain sizes (Hall-Petch effect) and small film thicknesses [Nix 1989, Arzt 1998, Keller et al. 1998, Baker et al. 2001]. Thus, there are two reasons to expect changes in fatigue life with decreasing length scale: first, yield stresses are increased [Nix 1989, Arzt 1998, Keller et al. 1998, Baker et al. 2001] so that the plastic strain is decreased for a given applied total strain or stress load, and second, the formation of characteristic, fatigue-induced, extended dislocation structures does not occur in small crystal volumes [Thiele et al. 2002, Zhang et al. 2003].

In this work, a new method has been used to perform thermal high cycle fatigue (*HCF*) tests on thin metal films. Detailed information about the experimental method can be found in Chapter 3. Briefly, alternating currents are used to periodically heat a metal structure on top of a thick substrate. Because of the difference in thermal expansion coefficients between the metal and the underlying substrate, strain cycles occur in the metal at twice the frequency of the electrical current. The experiments were performed *in-situ* in an SEM for two different Cu film thicknesses and the damage evolution is described in detail in Chapter 4. This chapter concentrates on the analysis of the number of cycles to electrical failure of the line. It was found that both the fatigue life and the damage morphology depended strongly on the film thickness. The results are critically compared with life data from mechanically fatigued Cu films and from bulk Cu with a wide range of grain sizes.

5.2 Experimental

Cu line structures with contact pads suitable for electrical connections were fabricated on both Si and sapphire substrates. The lines had widths between 8 and 14 µm, thicknesses of 100, 200, and 300 nm, and lengths of 800 µm. The Cu line structures on Si chips were produced by electron beam lithography, sputter deposition, and subsequent lift-off. The Cu lines on sapphire were produced by sputter deposition of blanket films, patterning of the structures by optical lithography and wet etching. Details about the sample fabrication can be found in Section 4.2.2.

Focused ion beam imaging was performed on the samples to measure line widths and grain sizes. The Cu on Si samples had line widths between 8 and 10 µm, while the Cu on sapphire samples had 14 µm wide lines with considerable roughness (~1 µm) of the edges. Channeling contrast in the focused ion beam images showed that the Cu films on Si were heavily twinned and that the mean grain sizes were roughly 0.3 µm for the 100 nm thick films, 1.0 µm for the 200 nm thick films, and 1.5 µm for the 300 nm thick films. The Cu on sapphire samples had grains with diameters between roughly 2 µm and 7 µm, mostly without twins. Details about the microstructure can be found in Section 4.2.3.

After their production and storage in vacuum, the samples were mounted in the SEM with the lower side of the substrate attached with thermal cement to the SEM stage. The samples were then electrically contacted using a motorized needle probe station in the SEM (Raith). An alternating voltage with a frequency of 100 Hz was applied to produce periodic heating in the lines. The resistance of the structures was determined during the cycles by a

four point measurement. Using the measured temperature coefficient of the resistivity of the structures, the temperature oscillations in the lines were calculated from the resistance measurements, as described in Chapter 3. Fatigue tests were performed using temperature ranges between 80 and 300 K. The minimum temperature depended somewhat on the electrical power but was within the range of 80 to 120°C for all of the experiments. The evolution of the damage was recorded by SEM pictures and the number of cycles to failure was defined by an electrical open. Further details about the testing method can be found in Chapter 3 including evidence that electromigration-induced damage is negligible.

5.3 Results

Thermal fatigue tests were performed on both the Cu on Si and Cu on sapphire samples *in-situ* in the SEM. The thermal cycles in the lines generated cyclic strains due to the difference

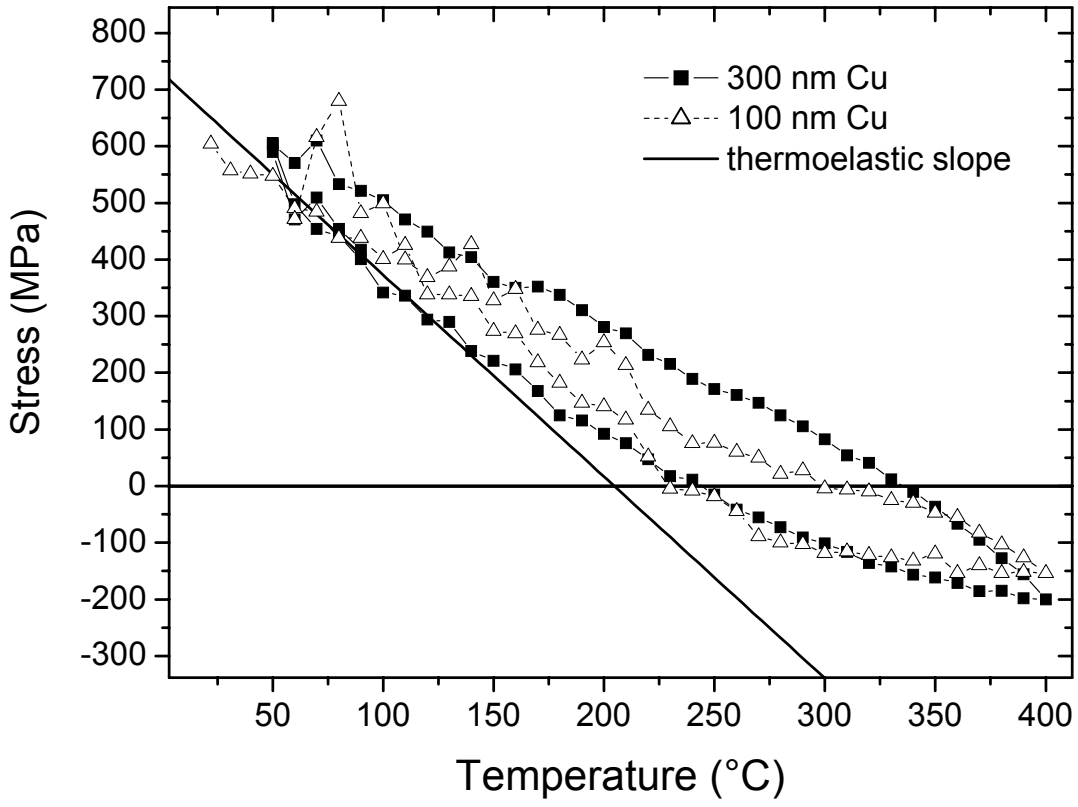

Fig. 5.1 Wafer curvature measurements for 100 nm (Δ) and 300 nm (■) thick Cu films on Si. The solid line shows the calculated thermoelastic slope for polycrystalline Cu with a <111> out-of-plane orientation.

between the coefficients of thermal expansion of the film and the substrate. Assuming temperature independent coefficients of expansion of 1.7×10^{-5}/K for Cu, 3×10^{-6}/K for Si, and 5×10^{-6}/K for sapphire, a temperature variation of 100 K would lead to a strain variation of 0.14% for Cu on Si and 0.12% for Cu on sapphire.

The amount of plastic strain produced in a film by an imposed temperature change can be determined from measurements of the stress in the film during thermal cycling. Fig. 5.1 shows the stress in the 100 and 300 nm films on Si obtained from wafer curvature measurements [Keller et al. 1999, Baker et al. 2001, Chapter 3] during cycling between room temperature and 400°C. Heating to 400°C produces a total strain of roughly 0.56% in the Cu film on Si and drives the stresses in the films from tensile to compressive. The total change in stress was about 800 MPa for the 300 nm thick film and about 750 MPa for the 100 nm film. For temperatures below 150°C, the slopes of the heating curves for both films agreed roughly with the thermoelastic value for a polycrystalline film with purely <111> texture (solid line in Fig. 5.1), suggesting that the films behaved predominately elastically over this temperature range. Deviations of the measured stress-temperature curves from the expected elastic slope are an indication of anelasticity or plasticity in the film. The stresses measured in Cu films on sapphire using the wafer curvature method were significantly smaller than those in the Cu on Si samples [Dehm et al. 2003], suggesting that the anelastic or plastic strains are larger in

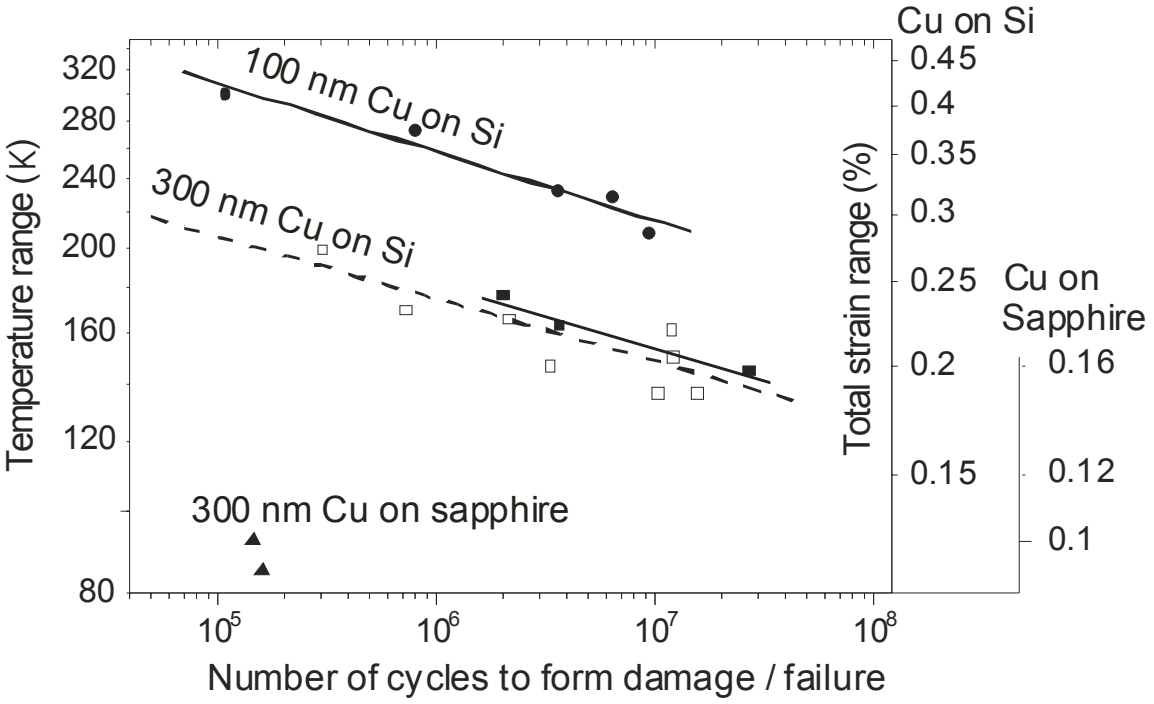

Fig. 5.2 Number of cycles to failure (filled symbols) or to formation of extensive damage (open symbols) for the 100 nm thick Cu on Si (●), the 300 nm thick Cu on Si (■/□), and 300 nm thick Cu on sapphire (▲). The temperature range is plotted on the left-hand axis and the total strain range on the right-hand axis.

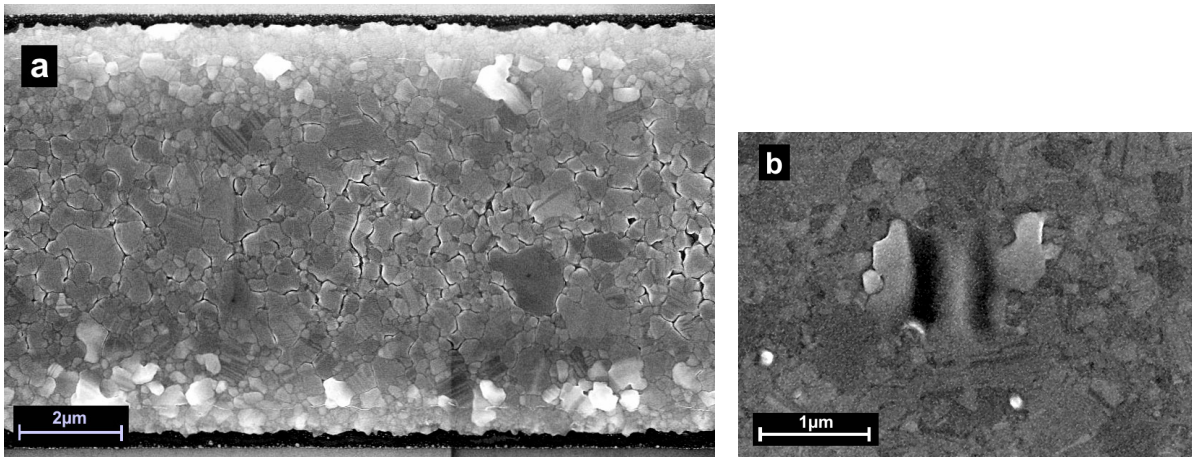

Fig. 5.3 Fatigue damage in 100 nm thick lines on Si showing (a) grain boundary grooves and hillocks after 7.9×10^5 cycles at $\Delta T = 274$ K, and (b) surface wrinkles, which were occasionally observed in the larger grains, after 2.5×10^5 cycles at $\Delta T = 210$ K.

these samples.

During fatigue testing, damage formed along the Cu lines and grew in extent and severity until electrical failure occurred. Fig. 5.2 shows a summary of the dependence of the temperature range on the number of cycles to failure (filled symbols) for all of the samples. The corresponding total strain range (which is different for the films on Si and sapphire substrates) is shown on the right-hand axis. In some cases, the samples were not tested to failure but only until extensive damage had formed. These samples are also included in Fig. 5.2 (open symbols). All samples show a decrease in cycle number with increasing strain range, as expected for fatigue. However, the different sample sets show markedly different failure behaviour. The 100 nm thick Cu on Si samples are the most fatigue resistant and can sustain significantly higher loads for a given number of cycles than the 300 nm thick Cu samples. For

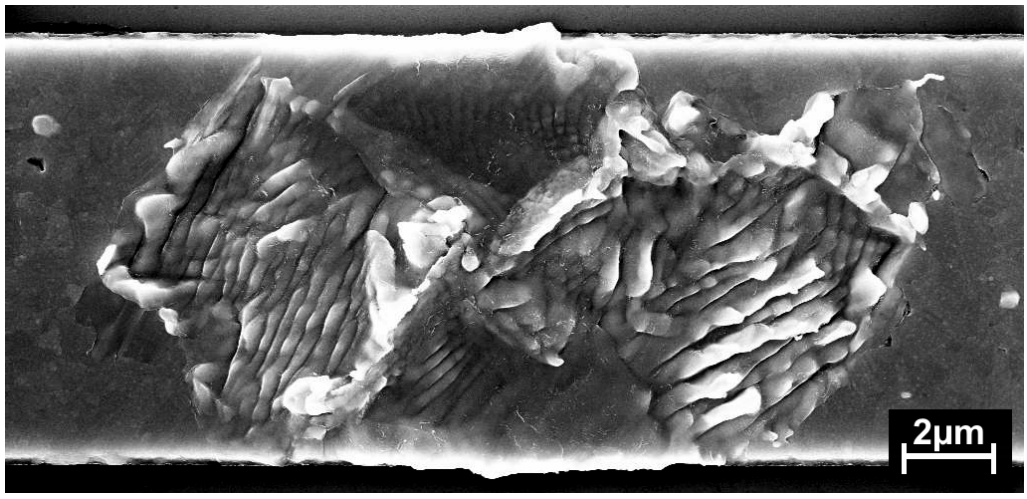

Fig. 5.4 Fatigue damage in 300 nm thick Cu on Si showing isolated damage patches consisting of regions of parallel wrinkles after 8×10^5 cycles at $\Delta T = 186$ K.

example, no damage was found in the 100 nm thick lines after 10^7 cycles at a temperature range of 200 K, although this temperature range is sufficient to cause extensive damage in the 300 nm thick lines within as few as 10^6 cycles. In contrast, the Cu on sapphire samples were extremely susceptible to fatigue and formed extensive damage after only $2x10^5$ cycles at a temperature range of 90 K. An additional test on the Cu on sapphire samples with ΔT of around 50 K did not lead to damage within $1.4x10^7$ cycles (20 h at 100 Hz).

In addition to clear differences in the number of cycles to failure, the different sample sets also showed markedly different damage morphologies. The typical damage in the 100 nm thick lines consisted of grain boundary grooves and grain thinning (Fig. 5.3(a)). The grooves were evenly distributed along the whole length of the line and were often accompanied by hillocks close to the line edges. According to focused ion beam cross-sections and imaging of the samples after testing, the groves often extended almost to the film/substrate interface. Surface wrinkles were only occasionally observed and then only in the larger grains (Fig. 5.3(b)).

In contrast, the 300 nm thick Cu on Si developed isolated damage patches consisting of regions of parallel wrinkles (Fig. 5.4) similar to the wrinkles observed in the largest grains of the 100 nm thick samples. Fewer damage patches were found at the ends of the lines near the contact pads, presumably due to the fact that the temperature ranges are somewhat smaller there (Chapter 3). During testing, the damage patches grew in number and size and eventually led to failure. Fig. 5.5 shows the area of a single patch as a function of cycle number. Fig. 5.6 shows the number and total area of damage patches, obtained from images of some of the 300 nm thick Cu on Si samples shown in Fig. 5.2. Both the total number and total area of damage patches increase strongly with the temperature range, while the ratio, i.e. the average area of a damage patch, is roughly constant as a function of temperature range. Microscopic and microstructural details about the evolution of these damage patches can be found in Chapter 4. The damage evolution in the 200 nm thick films was very similar to that in the 300 nm thick films.

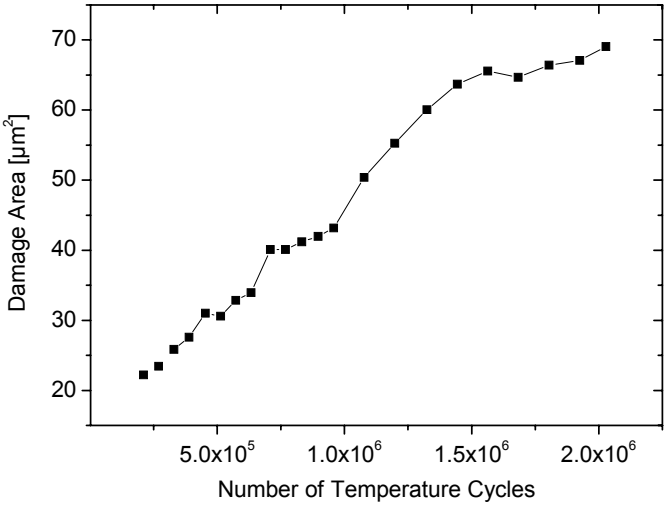

Fig. 5.5 Area of a single damage patch in 300 nm thick Cu on Si as a function of cycle number for $\Delta T = 178$ K.

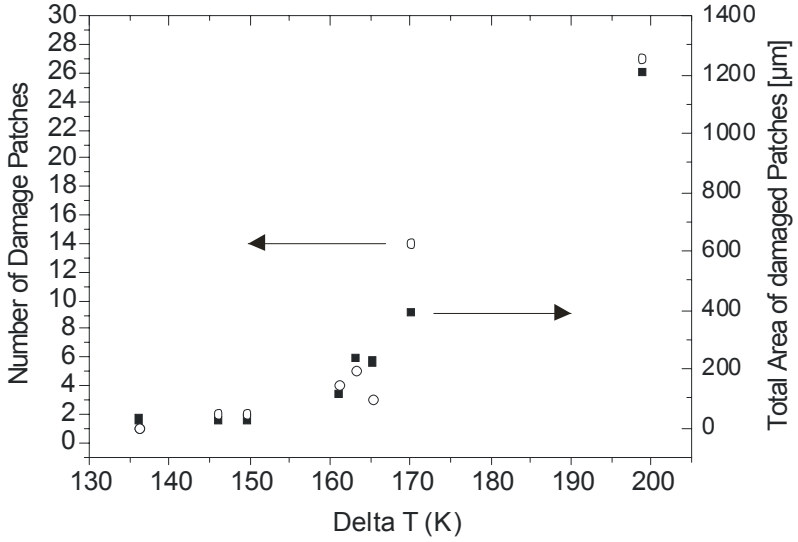

Fig. 5.6 Number (○) and total area (■) of damage patches in 300 nm thick Cu on Si as a function of temperature range.

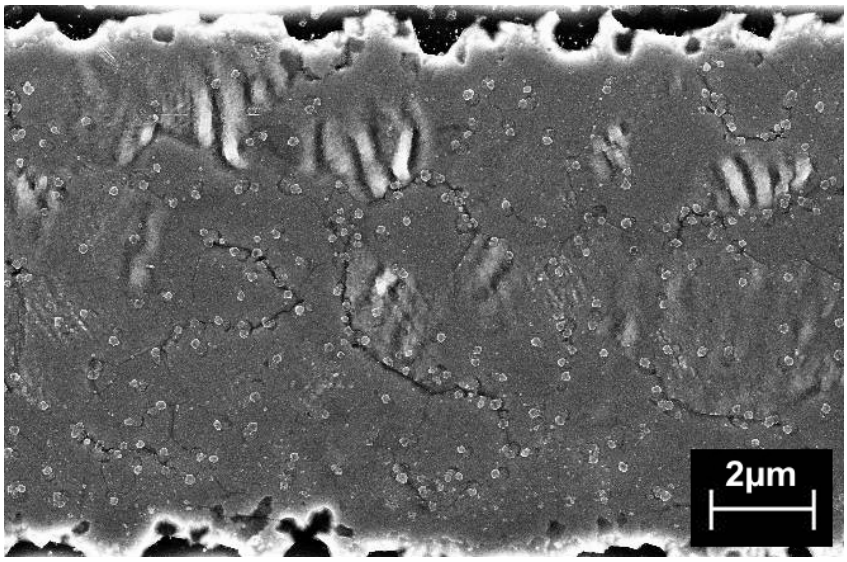

Fig. 5.7 Fatigue damage in 300 nm thick Cu on sapphire showing damage patches consisting of regions of fine and coarse parallel wrinkles. The small particles on the sample surface are artefacts of the preparation process. $\Delta T = 85$ K ($\Delta\varepsilon = 0.10\%$), 1.6×10^5 cycles.

The 300 nm Cu on sapphire samples also developed surface wrinkles during testing (Fig. 5.7 and Chapter 4). Both coarse surface wrinkles, similar to the ones observed in the 300 nm thick Cu lines on Si, and finer surface wrinkles were found. In comparison with the 300 nm Cu on Si samples, the damage patches in the Cu on sapphire were more uniformly and densely distributed along the line and the wrinkles were less severe in amplitude. Grain boundary grooves were occasionally observed in the 300 nm thick Cu films on sapphire. They were formed during the deposition process, presumably due to the elevated temperatures, and did not noticeably evolve during the short tests that were performed on these samples.

Grain boundary grooves were also observed in the 200 and 300 nm Cu on Si samples. However, these grooves only appeared after several hours of testing. An example is shown in Fig. 5.8 where small grooves first appeared at many of the grain boundaries of a 200 nm thick sample after $3x10^6$ cycles of testing (4 hours).

Fig. 5.8 shows images of a 200 nm thick Cu line just before failure by an electrical open. A damage patch was first formed (Fig. 5.8(a)) and then a crack nucleated at the damage patch and propagated across the width of the line (Fig. 5.8(b)). From the grain contrast in Fig. 5.8(a)), it can be seen that the crack is transgranular at least in the lower half of the line. This mode of failure, namely initiation of a crack at a damage patch, followed by rapid crack growth across the line, was observed in a 300 nm thick line as well. After failure, all failure sites showed evidence of local melting where the electrical open had formed (Fig. 5.9). Unfortunately, the melting obscured details of the failure site morphology. In addition, since the final stages of damage evolution and failure typically occurred very rapidly, details about the failure mode were only captured for the two samples just described (200 and 300 nm thick Cu on Si). Final stages of damage evolution were not captured in the 100 nm thick films and the failure sites did not look any different than those in the thicker films.

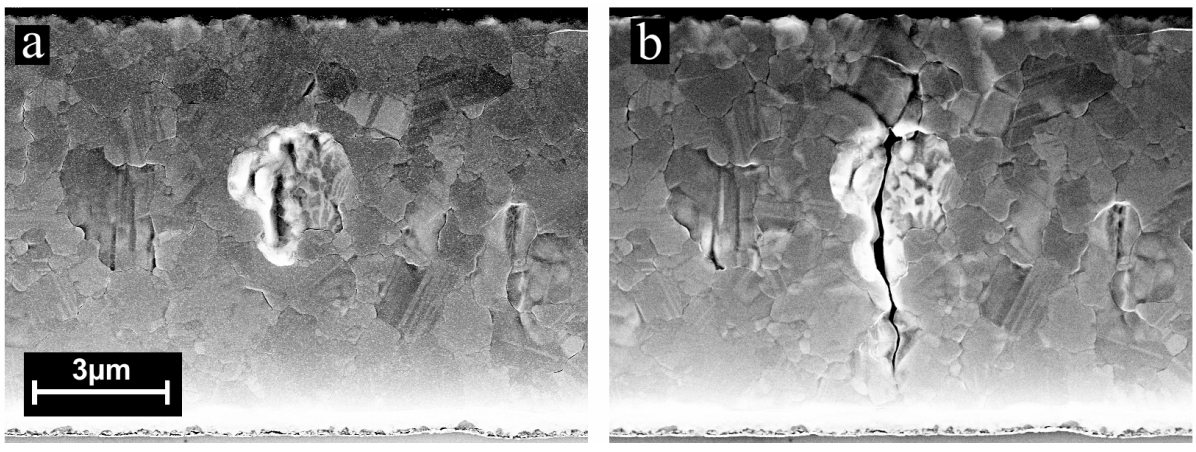

Fig. 5.8 200 nm thick Cu on Si sample cycled at a temperature range of 180 K, (a) after $3.2x10^6$ cycles and (b) $4x10^4$ cycles later, just before failure by an electrical open.

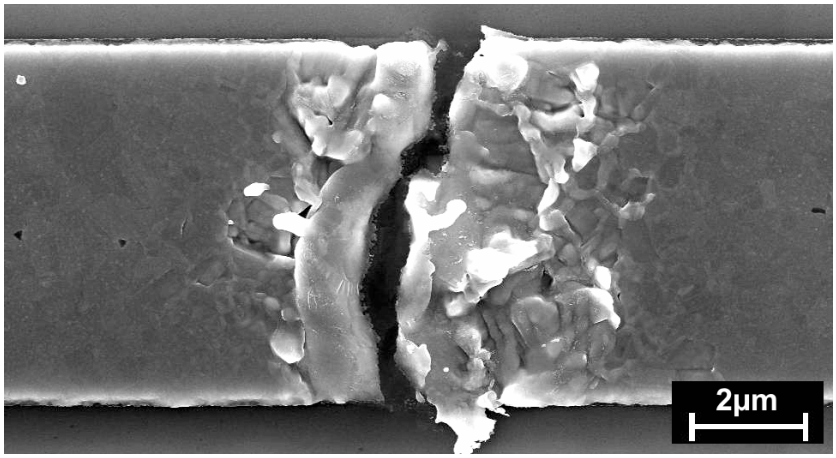

Fig. 5.9 Failure site in a 300 nm thick line on Si showing evidence of local melting where the electrical open had formed after 2.6×10^7 cycles at $\Delta T = 144$ K ($\Delta\varepsilon = 0.2\%$).

5.4 Discussion

The observations presented here show that fatigue damage formation and failure in thin Cu films depend strongly on the film thickness and the grain structure. Since damage formation in *HCF* is driven by local plasticity, the differences in the behaviour of the various samples presumably reflects differences in the plastic strain amplitude and how plastic strain is accumulated in the thin films. In the following, estimates of the plastic strain amplitudes in the samples will be made and then the differences in the damage morphology and cycles to failure of the 100 and 300 nm thick Cu on Si films will be compared and discussed.

5.4.1 Plastic strain range

Plastic strains are best measured using cyclic stress-strain curves. However, in the case of the samples investigated here, cyclic stress-strain curves were not available so the plastic strains were estimated from wafer curvature measurements during single thermal cycles of unfatigued Cu films. A single thermal cycle usually gives only a rough idea of the behaviour during thermal fatigue testing since significant softening or hardening may occur in the first hundred cycles of loading. However, a room temperature fatigue study on 1 µm thick Cu films on polyimide substrates showed little change in the stress-strain curves in the first 1000 cycles and changes that were observed at higher cycle numbers were attributed to cracks in the film [Kraft et al. 2002]. Therefore, the wafer curvature measurements were used here as an estimation of plastic strain in the 100 and 300 nm thick samples. The plastic strain was obtained from the data in Fig. 5.1 by first calculating the difference between the measured stress on heating and the stress expected from purely elastic behaviour, and then converting

this stress difference to a plastic strain using the biaxial modulus (a detailed discussion of the method used to estimate plastic strains is presented in Appendix C). The results are shown in Fig. 5.10 for different temperature ranges starting from a minimum temperature of 100°C. As expected, the plastic strain contribution increases with the total strain. Due to the approximate nature of this method and the similarity between the 100 and 300 nm wafer curvature data, no effort was made to determine different values of plastic strain for the 100 nm thick films. The difference in stress state between the films used for wafer curvature testing and the wide lines used for thermal fatigue testing is expected to be quite small (Chapter 3, Appendix B).

The fact that the wafer curvature measurements on the 100 and the 300 nm thick Cu on Si samples are so similar indicates that, at least in the untested condition, the two films experience the same plastic strain for a given temperature range. Therefore, the differences between the fatigue behaviour of these two film thicknesses likely lie in differences in the mechanisms for plastic strain accumulation, as will be discussed in Section 0. In contrast, wafer curvature measurements on the Cu on sapphire samples show that they experience much more plasticity for a given temperature excursion than the Cu on Si samples [Dehm et al. 2003]. This increased plasticity may be the result of the larger grain size and the absence of

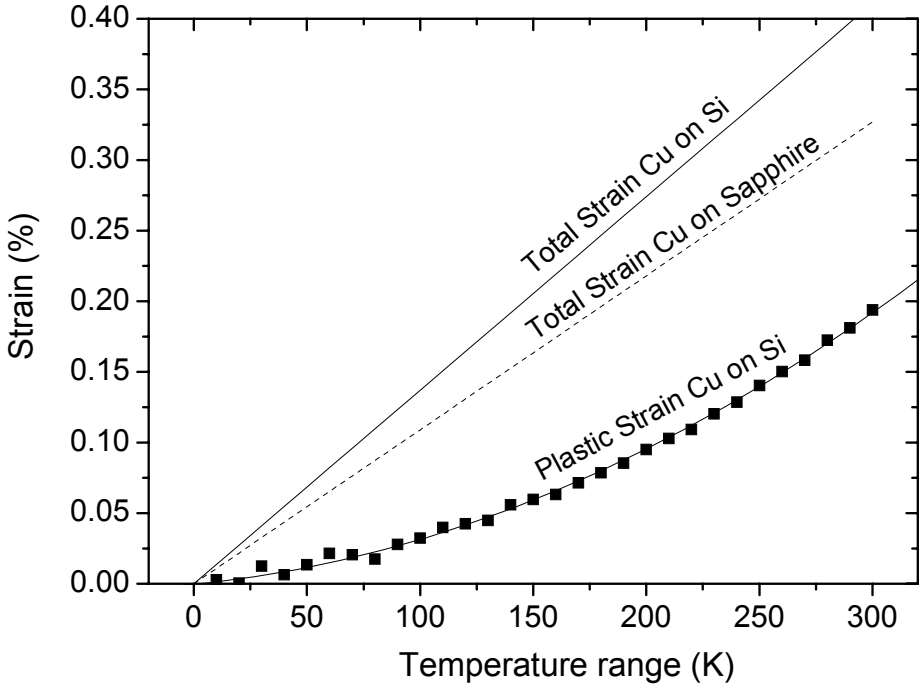

Fig. 5.10 Strain range in Cu thin films as a function of applied temperature range. The two lines show the total strain range, calculated assuming temperature-independent material properties for the Cu on Si (──) and Cu on sapphire samples (----). The data points show the plastic strain range in 300 nm thick Cu on Si samples, estimated using wafer curvature measurements as described in the text.

twins in the Cu on sapphire films (Chapter 4). Therefore, the decreased number of cycles to failure of the Cu on sapphire samples relative to the Cu on Si samples may simply be due to the larger plastic strains in these samples for a given applied temperature range.

5.4.2 Damage morphology

The surface damage in the 300 nm Cu films has been discussed in detail in Chapter 4 and can be understood in terms of dislocation glide and dislocation interactions with twin and grain boundaries in the thin films. The isolated damage patches observed in the 300 nm thick samples are known to be localized within single grains. The growth of the damage patch area with cycle number (Fig. 5.5) is associated with fatigue-induced growth of the damaged grain (Section 4.4.2.4). The size of the individual damage patches does not depend on the applied strain range, but many more damage patches are formed for higher strain ranges (Fig. 5.6). This can be explained by the fact that at higher applied strains, more grains are oriented so that their resolved shear stresses are large enough to cause dislocation glide. The 100 nm thick Cu film on Si (grain size 0.3 μm) showed completely different fatigue damage than the 300 nm thick Cu film on Si (grain size 1.5 μm). The periodic surface wrinkles are absent from the 100 nm thick films (except in the largest grains) suggesting that dislocation motion, which is believed to be responsible for the wrinkles (Chapter 4) is suppressed. From the fact that wrinkles are observed in the largest grains of the 100 nm thick film, it is apparent that both film thickness and grain size must be sufficiently small to hinder wrinkle formation under cyclic loading. Instead, the extensive groove and hillock formation in the 100 nm thick films point to significant boundary and surface diffusion. Diffusion mechanisms have long been considered as important candidates for stress relaxation in thin films [Jackson and Li 1982, Thouless et al. 1993, Gao et al. 1999]. In general, although the basic features remain the same, a wide variety of different stress-temperature curves have been measured in Cu films [Keller et al. 1999, Baker et al. 2001, Vinci et al. 2002, Weiss et al. 2001, Balk et al. 2003]. A number of models based on classic deformation models have been developed to fit the data [Thouless et al. 1993, Keller et al. 1999, Baker et al. 2001, Weiss et al. 2001] and show that some of the data are best described by including diffusion as an active mechanism for stress relief. For example, although an inverse thickness dependence of the yield stress is expected in thin films with dislocation glide-controlled stress relief [Nix 1989, Venkatraman and Bravman 1992], such a dependence has rarely been reported in the literature for films thinner than 400 nm [Baker et al. 2001, Weiss et al. 2001, Balk et al. 2003]. A recent paper has attributed this "plateau" in yield stress in Cu films for thicknesses less than roughly 400 nm, to the onset of

"parallel glide" of dislocations in the <111> plane parallel to the film/substrate interface [Balk et al. 2003]. The generation of parallel glide dislocations is argued to be driven by shear stresses generated by the diffusion of atoms between the surface and the grain boundaries [Gao et al. 1999]. In fact, this mechanism has also been observed in the samples studied here: preliminary plan-view TEM observations of the 200 nm thick thermally fatigued Cu films studied here, show significant numbers of "parallel glide" dislocations in grains with a <111> out-of-plane orientation [Zhang et al. 2004].

Therefore, it seems that there is evidence to support the idea that the difference in fatigue behavior between the 100 and 300 nm thick Cu films is due to the existence of a transition from dislocation-controlled to diffusion-controlled mechanisms with decreasing film thickness and grain size. As the film thickness and grain size decrease, larger and larger stresses are needed to drive dislocation nucleation and motion [Nix 1989, Thompson 1993, Arzt 1998, Keller et al. 1999, Baker 2001, Baker et al. 2001, Hommel and Kraft 2001, v. Blanckenhagen 2002, Balk et al. 2003] and the presence of more interfaces promotes diffusive processes. In addition to the extensive boundary grooves at the surface of the 100 nm thick films, support for the existence of this transition is found in the wafer curvature data for the 100 nm and 300 nm films, which show no effect of film thickness on the yield strength (Fig. 5.1). This indicates that dislocation glide no longer controls deformation and diffusive mechanisms have taken over in the 100 nm thick film. Diffusion is also active during fatigue in the 300 nm thick films, albeit somewhat slower due to fewer boundaries and longer diffusion distances. The reason that surface damage due to boundary and surface diffusion is not so prevalent in the thicker films is simply because they fail by dislocation glide processes before the diffusion mediated processes can lead to noticeable surface damage.

Diffusion or creep under cyclic loading can lead to irreversible behavior and damage accumulation when diffusion is coupled with some other process such as grain boundary sliding [Wigmore and Smith 1971] or dislocation emission [Gao et al. 1999, Balk et al. 2003]. The fact that parallel glide dislocations have been seen in the samples studied here [Zhang et al. 2004], is a strong evidence for this second mechanism. However for the thermally fatigued films, there are many possible additional sources for irreversible behavior during cyclic loading, such as non-zero mean stresses and racheting effects. For example, the thin films experience temperature cycles which are out-of-phase with the stresses (temperatures are high when the films are under compression and low when they are under tension). At the same time, the wafer curvature data on unfatigued Cu films (Fig. 5.1) indicate that the mean stresses in the films are predominately tensile for the temperature ranges used for fatigue

testing. Thus, it is not clear whether diffusive motion occurs predominately under a tensile stress or under a compressive stress. Tensile stresses promote grain boundary grooving by stress gradient-driven atomic diffusion between the sample surface and the grain boundaries [Genin 2001], which could explain the grain boundary grooves observed in the middle of the 100 nm thick lines (Fig. 5.3(a)). Compressive stresses favour the formation of hillocks, such as those that are observed at the edges of the 100 nm thick lines. This suggests that diffusive processes driven by tensile stress dominate at the center of the 100 nm thick lines and diffusive processes driven by compressive stress dominate at the edges of the lines. Plasticity due to interface shear stresses where the line edge meets the substrate can cause ratcheting [Suresh et al. 1994, Huang et al. 2002] which may lead to the formation of compressive stresses at the line edge. Therefore, the damage morphology in the 100 nm thick Cu can be accounted for by assuming that the stresses remain tensile in the middle of the line, leading to groove formation, and are driven compressive by ratcheting at the line edges, leading to the formation of hillocks. Thus, there are plausible explanations for damage formation in the thin films by diffusive mechanisms under cyclic loading.

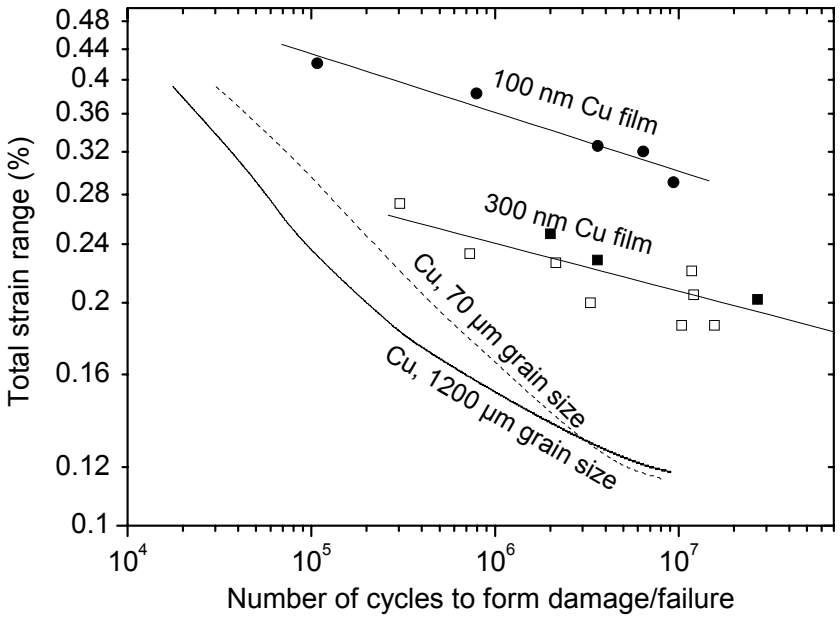

Fig. 5.11 *Total* strain range versus the cycles to failure (filled symbols) or cycles to damage formation (open symbols) for the 100 nm thick Cu films on Si (●), the 300 nm thick Cu films on Si (■/□) and for bulk Cu with 70 (----) and 1200 µm grain sizes (──) [Lukáš and Kunz 1987].

5.4.3 Cycles to failure

Insights into the fatigue behavior of the thermomechanically cycled Cu films can be gained by comparison with fatigue literature for bulk Cu. Fig. 5.11 shows the *HCF* data for the thermally fatigued 100 and 300 nm thick Cu films on Si (0.3 and 1.5 μm grain sizes) plotted in terms of the *total* strain range. These data lie well above *LCF* and *HCF* data for large-grained, bulk Cu (solid lines), also obtained from total strain controlled tests on material with 70 and 1200 μm grain sizes [Lukáš and Kunz 1987]. The thin film data are fit with straight lines, giving a fatigue strength exponent of roughly –0.07. Typical slopes for large-grained bulk metals lie between –0.05 and –0.12 in the *HCF* regime. Thus, although the magnitude of the slope is less than that observed for the bulk Cu plotted in Fig. 5.11, it is well within the

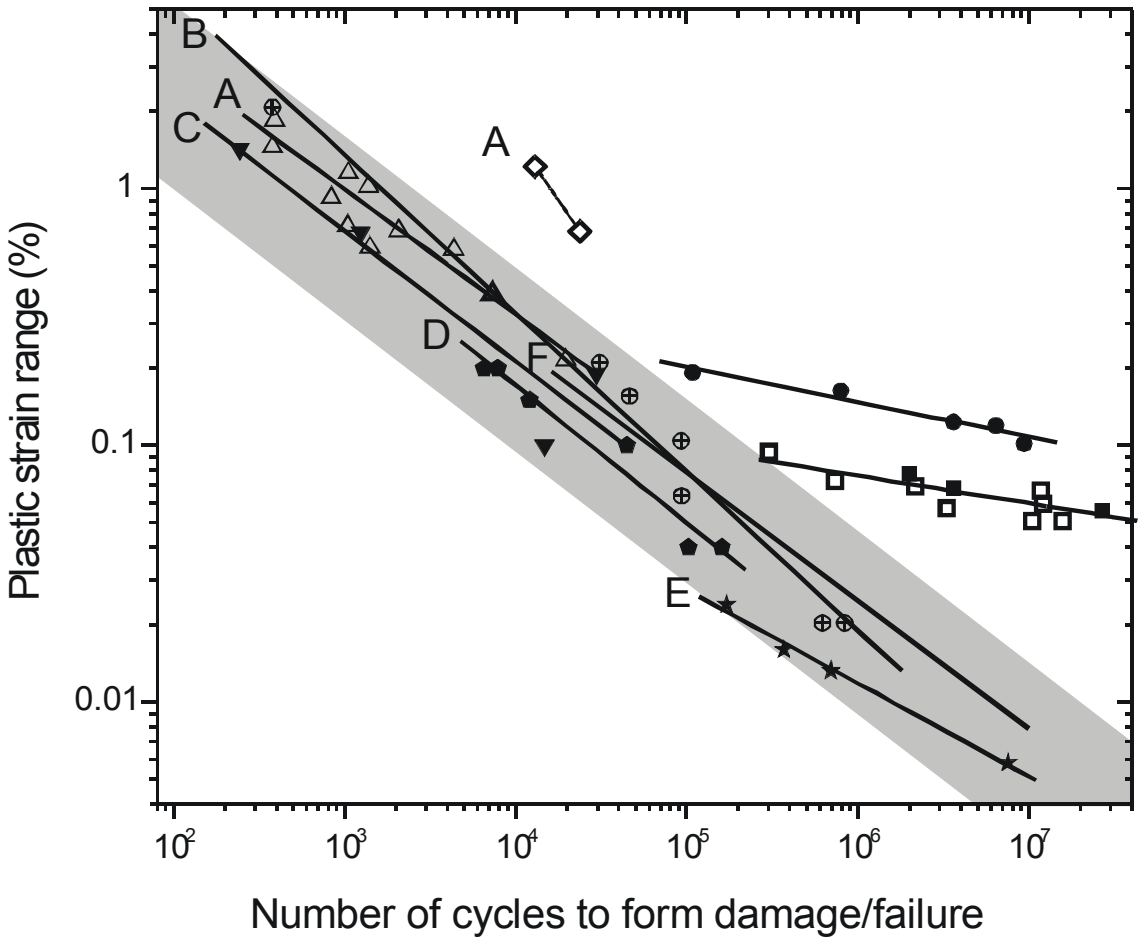

Fig. 5.12 Dependence of the *plastic* strain range on the cycles to failure (filled symbols) or cycles to damage formation (open symbols) for the 100 nm thick Cu films on Si (●), the 300 nm thick Cu films on Si (■/□), Cu films on polyimide substrates (◇ for 0.4 μm thick films, △ for all of the others) [Kraft et al. 2002] and for a number of fine-grained and large-grained bulk Cu samples described in the text. All samples other than films thinner than roughly 500 nm fall in the shaded region.

range of typical values.

The data in Fig. 5.11 all exhibit the trend that the cycles to failure increase with decreasing grain size for a given total applied strain. This trend is at least partly explained by the increase in flow stress with decreasing grain size (Hall-Petch hardening) and film thickness [Nix 1989, Thompson 1993]. An increase in flow stress leads to a decrease in plastic strain range and therefore an increase in the number of cycles to failure. This is likely the explanation for why the thin films survive more cycles than the bulk specimens. However, as shown in Fig. 5.1 and discussed in Section 5.4.2, the two film thicknesses investigated here show no difference in flow stress. Therefore, the difference in cycles to failure for the two film thicknesses must come from a difference in the nature of the plastic strain or how it is accumulated during fatigue.

In order to look more carefully for the effect of plastic strain on cyclic damage accumulation, the number of cycles to failure must be plotted in terms of the plastic strain range. Trends that appear in such a plot can be directly attributed to mechanisms for cyclic plastic strain accumulation, rather than to differences in yield strength. Fig. 5.12 shows a plot of the plastic strain range versus cycles to fail or to form damage for a number of different samples in both *LCF* and *HCF*. The total strains from the thermally fatigue Cu thin films have been transformed to plastic strains with the use of the data in Fig. 5.10. Also included in Fig. 5.12 are literature data sets from Cu films, ultra fine-grained bulk Cu, and large grain bulk Cu:

A) Cu films on polyimide substrates with film thicknesses of 0.4 (open diamonds), 1.1, 1.5, and 3.1 μm (open triangles) [Kraft et al. 2002]. Grain sizes increased from roughly 0.3 to 0.8 μm with film thickness. The *LCF* tests were performed at room temperature under approximate total strain-control. Plastic strains were estimated from single stress-strain cycles performed on similar samples before fatigue testing.
B) Large-grained bulk Cu with an average grain size of 25 μm [Mughrabi and Wang 1988]. The *LCF* and *HCF* tests were performed under plastic strain-control.
C) Ultra-fine-grained bulk Cu with an average initial grain size of 200 nm [Agnew and Weertman 1998]. The *LCF* tests were performed under total strain-control and transformed using plastic strain amplitudes recorded just before failure. This material exhibited grain coarsening and softening during fatigue testing.
D) Ultra-fine-grained bulk Cu with an average initial grain size of 300 nm [Höppel et al. 2002]. The *LCF* tests were performed under plastic strain-control. This material exhibited grain coarsening during fatigue testing.

E) Ultra-fine-grained bulk Cu with an average initial grain size of 300 nm [Höppel et al. 2002]. The *HCF* tests were performed under stress-control and transformed using plastic amplitudes recorded at half the fatigue life. This material exhibited grain coarsening during fatigue testing.

F) Large-grained bulk Cu with an average grain size of 70 μm [Lukáš and Kunz 1987]. The *HCF* tests were performed under total strain-control and transformed using plastic strain amplitudes recorded at half the fatigue life.

It is fairly well accepted that fatigue life is improved by decreasing grain size in bulk Cu, due in part to an increase in yield stress and in part to smaller dislocation pile-ups in fine-grained materials. Therefore, it is surprising that the ultra-fine-grained bulk Cu plotted in Fig. 5.12 has a similar or shorter fatigue life than the coarse-grained bulk Cu. This has been attributed to microstructural changes such as grain coarsening and shear band formation in the ultra-fine-grained Cu during fatigue, which may lead to early failure [Agnew and Weertman 1998, Höppel et al. 2002].

The data sets from the thermally fatigued Cu thin films lie significantly higher than all of the fine-grained and large-grained bulk Cu data. The data from the thinnest (0.4 μm) room temperature fatigued Cu film (data set A) also lie higher than the bulk data. In addition, the magnitude of the fatigue ductility exponent for the thermally fatigued Cu thin films is significantly smaller than for the other samples. The fatigue ductility exponent for the thermally fatigued Cu thin films is given by –0.12, while the other samples plotted in Fig. 5.12 have values of roughly –0.5.

In discussing the trends shown in Fig. 5.12, it is important to consider the many differences in testing conditions. The most important of these include temperature, mean stress, sample geometry, failure criteria, and of course, fundamental differences in the plastic response of the different samples. At first glance, the effect of temperature does not appear to be large in Fig. 5.12. The thermally fatigued Cu thin film data extrapolates reasonably well to that for the thin films cycled at room temperature. Generally, elevated temperatures below half the melting point lead to only modest decreases in fatigue life, especially in vacuum. Nonetheless, the temperature may account for the small magnitude of the fatigue ductility exponent since the number of cycles to failure may be somewhat decreased at large plastic strains due to the increase in average temperature in the sample.

As can be seen from Fig. 5.1, the Cu films have a tensile mean stress during temperature cycling. Depending on hardening/softening and racheting effects, the mean stress

may change during fatigue testing. In any case, based on the wafer curvature cycles on the films, it is reasonable to believe that the mean stress decreases with increasing temperature range (for a fixed minimum temperature). Tensile mean stresses decrease the number of cycles to failure through their enhancement of crack nucleation and growth. Therefore, if the data points in Fig. 5.12 could be corrected to remove the effects of a non-zero mean stress, they would probably lie somewhat higher and have an even smaller slope than they have presently.

The fact that there is a substrate under the films certainly has an effect on fatigue behavior. Basically, the substrate distributes the stresses in the film and reduces strain localisation during fatigue. This will influence both the damage evolution and the failure mode. Before cracks have formed and while damage is still moderate, the substrate is expected to have little effect on damage evolution. Once cracks have formed, the substrate will have a large effect, in particular by slowing down crack propagation [Cook and Suo 2002]. Thus, the substrate is expected to have a large role in *LCF* experiments, where the fatigue life is predominately a measure of crack propagation, and a small role in *HCF* experiments, where cracks only form at the very end of the fatigue life. Particularly in the *LCF* regime, the slowing of crack propagation will prolong the fatigue life and favour a uniform distribution of many small cracks in the film over a single crack that propagates to cause fracture. These considerations suggest that comparisons of fatigue lives of films on substrates with bulk specimens or free-standing films is reasonable in the *HCF* regime, but may be somewhat problematic in the *LCF* regime.

The substrate also clearly has an impact on an appropriate definition for failure. While failure in a bulk specimen in usually defined by structural instability or complete fracture, this is not a practical failure criterion for studying the reliability of a thin film on a substrate. A very reasonable alternative has been proposed by an abrupt decrease in mechanical energy loss of the film/substrate composite, which corresponds to the formation of extensive arrays of extrusions and cracks [Schwaiger 2001, Kraft et al. 2002]. However, as mentioned above, such failure morphology will not be reached in a bulk sample or free-standing film, since they generally fail by propagation of the first crack that exceeds a critical length. Similarly, in the thermally fatigued lines studied here, it is expected that current crowding and local heating effects will lead to failure at the first crack or damaged region that exceeds a critical size. Damage was first observed in the thin films after ~10% of the fatigue life and, in the example shown in Fig. 5.8, evolved until crack formation at ~99% of the fatigue life. Therefore, the

complicated effects of thermomigration and electromigration, which may contribute in the final stages of damage formation, have very little influence on the total measured life.

It is worth noting that failure in bulk Cu occurs even before damage is first observed in the thin films (at 10% of the fatigue life of the thin films). Thus, it appears that even after considering the many differences in the testing conditions, there is a real enhancement in the fatigue life of the thin films, which is presumably due to fundamental differences in mechanisms for plastic strain accumulation. The small magnitude of the fatigue ductility exponent in the thermally fatigued thin films may be caused by heating of the sample at high plastic strains, or by premature failure possibly by current crowding and local heating once a defect of a critical size is formed. But it is also possible that the small slope is fundamental manifestation of the failure mode. The fact that the fatigue ductility exponents are so similar for the 100 and the 300 nm thick films despite their obvious differences in damage morphology supports the idea that failure of the 100 nm thick films occurs in the largest grains by the fatigue mechanisms observed in the thicker films.

The data presented here and the above discussion have served to clarify that there is a fundamental enhancement in fatigue life with decreasing film thickness and grain size which is not simply due to an increase in yield stress. The most likely explanation for this enhancement is that the damage produced by boundary diffusion in the 100 nm thick Cu films is less likely to cause failure than the localized damage regions formed by dislocation motion in the 300 nm thick Cu films. A general concept that might account for this effect is the idea that smaller defects or damage might “heal” more easily under stress reversal than larger defects, which is consistent with classic arguments for nucleation. This would mean that under a given plastic strain amplitude, less damage would accumulate either for very small plastic strain amplitudes (fatigue threshold effect) or in very small structures where the defect size is limited by geometry or microstructure.

5.5 Summary

The high cycle thermal fatigue behavior of thin Cu films on substrates has been studied as a function of film thickness and plastic strain. Results have been obtained for fatigue damage morphology and fatigue lives of 100 and 300 nm thick Cu films and compared with the fatigue lives of bulk Cu and thicker Cu films. A number of conclusions have been reached:

1. The difference in fatigue damage morphology between the 100 and 300 nm thick Cu films is due to the existence of a transition from dislocation-controlled to diffusion-controlled mechanisms with decreasing film thickness. This transition is attributed to the inhibition of dislocation activity and increase in boundary density at small length scales.
2. The thermally fatigued Cu thin films show an enhanced fatigue life relative to bulk Cu of all grain sizes and thicker films. This enhancement is not only due to the increase in yield stress with decreasing grain size and film thickness, but due to a second, new effect which has to do with the nature of the plastic strain and how it is accumulated in the thin films.
3. The 100 nm thick Cu films show an enhanced fatigue life relative to the 300 nm thick films. These films have similar yield stresses so the effect must be due to the difference in fatigue damage morphology. Apparently, the diffusion-induced surface damage does not lead to failure as easily as the more localized dislocation glide-induced damage.

The clear effect of length scale on fatigue damage morphology and fatigue life needs to be considered carefully in the design of reliable microsystems that are subjected to cyclic loads. Motivated by both fundamental interest and technological applications, it is proposed that future studies be extended to even smaller film thicknesses and grain sizes.

6 Summary and Conclusion

The response of metals with micron or submicron dimensions to cyclic mechanical loads is of great importance to the reliability of modern microelectronic and micro-electro-mechanical devices. The behavior of small scale metal structures under constant and monotonic loads has been extensively studied in the literature and the enormous strength of these structures has been explained by the effect of geometric constraints and grain size on dislocation motion. In contrast, only little is known about the behavior of small metal structures under cyclic loads and it is not clear to what extent the increase in strength under monotonic loading improves the fatigue performance. This work presents the results of a first investigation of the behavior of thin Cu films under high cycle thermal fatigue. The aim of this research was to characterize the dominant mechanisms for fatigue damage formation and failure. It has been found that both the mechanisms for damage formation and the fatigue life of these structures is strongly influenced by geometrical and microstructural length scales.

In this work, thermal fatigue experiments were performed on Cu structures with thicknesses of 100 nm, 200 nm, and 300 nm. These structures were fabricated using standard lithographic techniques on Si and sapphire substrates and were tested *in-situ* in a scanning electron microscope using a new experimental method. The method uses alternating currents to periodically heat the Cu structure on a substrate. Because of the difference in thermal expansion coefficients between the Cu and the underlying substrate, strain cycles occur in the metal and lead to the formation of fatigue damage. Fatigue experiments have been carried out in the *HCF* regime and damage was observed in 300 nm thick Cu lines on Si for temperature ranges as low as 140 K after 10^7 cycles. The damage morphology was monitored during testing using scanning electron microscopy images until failure occurred by the formation of an electrical open.

During fatigue testing, Cu films with thicknesses of 200 and 300 nm developed local regions of severe surface damage. *In-situ* observations revealed that the damage started as small wrinkles close to the grain and twin boundaries in a given grain and subsequently spread out through the grain. The exact nature of the damage depended on the grain orientation and was found to be very different for grains with <100> and <111> out-of-plane orientations. In <111> grains, large wrinkles formed and grew in amplitude within the bounds of the original grain boundaries. The spread of damage was often hindered by twin boundaries.

When the twin density was low, periodic surface wrinkles formed along directions parallel to the intersection of slip planes with the grain surface. In <100> grains, wrinkle formation was accompanied by twin dissolution and facetted grain growth. In many cases, the <100> grains grew to be many times their original size. The surface wrinkles in these grains typically lay along <100> directions on the sample surface, which do not correspond to the intersection of a slip plane with the grain surface.

Some of the differences in damage formation between the two grain orientations were explained by dislocation-twin interactions. A calculation of the highest resolved shear stresses in thin Cu films showed that dislocations can be directly transmitted across twin boundaries in <100> grains but not in <111> grains. Thus, the twin boundaries in the <111> grains block dislocation motion whereas the boundaries in <100> grains do not. During transmission of dislocations across the twin boundaries in <100> grains, residual dislocations are created which move under the action of shear stresses at the twin interface and may lead to dissolution of the twin lamella.

The dramatic facetted growth of the <100> grains can be understood by considering the grain boundary mobility. The <100> grains are the minority texture component and are typically surrounded by <111> grains. Differences in stresses or damage accumulation during fatigue due to crystallographic orientation may therefore provide a driving force for grain growth. The grain boundary mobility necessary for rapid grain growth and grain faceting along {111} planes can be understood in terms of classic ideas about the effect of defects, such as steps and kinks, on the boundary mobility. During fatigue, the large plastic strains experienced in the damaged grains lead to a large flux of dislocations and point defects to and from the grain boundaries, which causes an increase in grain boundary mobility.

The complex damage morphology evolution observed in the 200 and 300 nm thick films provides valuable insight into fatigue processes. In bulk materials, surface morphology development during fatigue has been associated with extended dislocation structures. However plan-view TEM observations of the films showed that these dislocation structures are absent in the 200 and 300nm thick films, and despite this, extensive fatigue damage is observed. The nature of the damage in the Cu films is substantially different from that observed in large-grained, bulk Cu and is reasonably well described by gliding dislocations which interact with each other and with twin and grain boundaries. The strong dependence of the damage evolution on grain orientation reveals the importance of the exact details of microstructure and crystallography. In addition, the observation of fatigue-induced grain

growth shows the importance of microstructural instabilities during mechanical loading in samples with small length scales.

The damage observed in the thermally fatigued 100 nm thick films looked completely different from that observed in the thicker films. Surface wrinkles were rarely observed, and then only in the larger grains of these films. Instead, the typical damage in the 100 nm thick films consisted of grain boundary grooves and hillocks. These surface features are believed to form by surface and boundary diffusion, which take over as a stress-relief mechanism at small grain sizes and small film thicknesses when dislocation activation becomes very difficult.

All of the investigated Cu films showed much higher fatigue lives than bulk Cu and in addition, the 100 nm thick films could sustain a significantly higher number of cycles than the 300 nm thick films. In the literature, this increased resistance of small metal structures or fine-grained metals has been related to their higher yield strength. However, for the films tested here, there is another reason for fatigue life enhancement, namely that thinner films can accommodate higher plastic strains before failure. This indicates the presence of a second size effect in the mechanical behavior of small structures. Possible justifications for this size effect are that the damage in thin films is more homogeneously distributed or preferentially healed on load reversal.

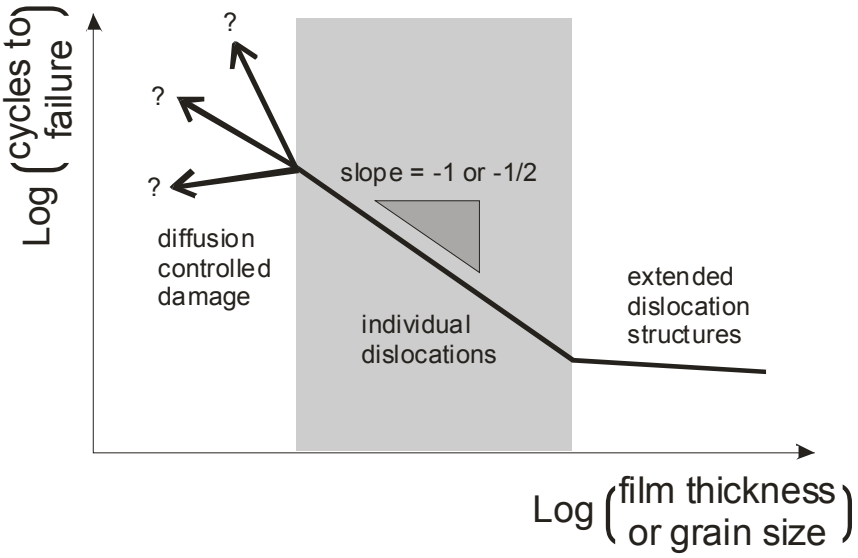

Fig. 6.1
Map of fatigue life as a function of film thickness or grain size, showing the effect of length scale on the mechanisms for fatigue failure.

A summary of the expected dependence of high cycle fatigue life for easy cross-slip metals as a function of film thickness or grain size is shown in Fig. 6.1 for a fixed plastic strain amplitude. At large length scales, where fatigue is mediated by extended dislocation structures, the weak dependence on length scale comes from changes in the ease of crack nucleation and crack propagation. At length scales which are too small for the formation of

extended dislocation structures, the failure is presumably controlled by the constrained motion of individual dislocations. TEM investigations of Cu films reveal, that extended dislocation structures cease to exist for film thicknesses and grain sizes below 3 μm [Zhang et al. 2003]. Below this critical thickness, the effect of grain size and film thickness on dislocation nucleation and motion may be expected to lead to an inverse dependence of fatigue life on length scale. Finally, at length scales where diffusion takes over as the vehicle for plastic strain accumulation, the work presented here has shown that fatigue lives will further increase. However, the exact dependence of fatigue life on length scale has not yet been explored. The transition between individual dislocation activity and diffusion mediated fatigue occurs in Cu for film thicknesses between 100 nm and 200 nm and grain sizes between 0.3 μm and 1 μm.

The results from this work have served to clarify that both the damage mechanism and the fatigue life are changed as film thickness decreases. The formation of fatigue damage is a ubiquitous phenomenon even at length scales where the characteristic dislocation structures – which have long been considered the vehicle for fatigue damage formation – can no longer form. As the length scale is decreased, it is found that new dislocation mechanisms take over and eventually are altogether replaced by interface diffusion-controlled processes. Although these phenomena are influenced by the well-known constraint of dislocations in small dimensions, the effects cannot simply be explained by an increased yield stress. Instead, it is found that new ideas about how plastic strain is accumulated in small structures need to be considered. It is concluded that future research in fatigue of small metal structures, aimed at achieving highly reliable materials, should carry these investigations to even smaller length scales and focus on the effect of interfaces and details of plastic strain accumulation.

Literature

Ackermann, F., Kubin, L. P., Lepinoux, J., and Mughrabi, H. (1984). "The dependence of dislocation microstructure on plastic strain amplitude in cyclically strained copper single crystals." *Acta metall.*, 32(5), 715.

Agnew, S. R., Vinogradov, A. Y., Hashimoto, S., and Weertman, J. R. (1999). "Overview of Fatigue Performance of Cu Processed by Severe Plastic Deformation." *J. electron. mater.*, 28(9), 1038.

Agnew, S. R., and Weertman, J. R. (1998). "Cyclic softening of ultrafine grain copper." *Mat. sci. eng.*, A244, 145-153.

Arzt, E. (1998). "Size effects in materials due to microstructural and dimensional constraints: a comparative review." *Acta mater.*, 46(16), 5611-5626.

Baker, S. P. (2001). "Plastic deformation and strength of materials in small dimensions." *Mat. sci. eng.*, A319-321, 16.

Baker, S. P., Kretschmann, A., and Arzt, E. (2001). "Thermomechanical behaviour of different Texture Components in Cu thin Films." *Acta mater.*, 49(12), 2145.

Balk, T. J., Dehm, G., and Arzt, E. (2003). "Parallel glide: unexpected dislocation motion parallel to the substrate in ultrathin copper films." *Acta mater.*(51), 4471.

Basinski, Z. S., and Basinski, S. J. (1992). "Fundamental Aspects of low Amplitude cyclic Deformation in face-centered cubic Crystals." Progress in Materials Science, B. Contor and P. B. Hirsch, eds., Pergamon Press plc, 89.

Basquin, O. H. (1910). "The exponential law of endurance tests." *Proc. of the ASTM*, 10, 625.

Bastawros, A.-F., and Kim, K.-S. (1998). "Experimental study on electric-current induced damage evolution at the crack tip in thin film conductors." *J. electron. packag.*, 120(4), 354.

Blech, I. A., and Herring, C. (1976). "Stress generation by electromigration." *Appl. phys. lett.*, 29, 131.

Cahill, D. G. (1990). "Thermal conductivity measurements from 30K to 750K: the 3ω method." *Rev. sci. instrum.*, 61(2), 802.

Carslaw, H. S., and Jaeger, J. C. (1959a). "Conduction of Heat in Solids." p. 67, Clarendon Press, Oxford

Carslaw, H. S., and Jaeger, J. C. (1959b). "Conduction of Heat in Solids." p. 263, Clarendon Press, Oxford

Chaudari, P. (1979). "Plastic properties of polycrystalline thin films on a substrate." *Philos. mag. A.*, 39(4), 505.

Cheng, A. S., and Laird, C. (1981). "The high cycle fatigue life of copper single crystals tested under plastic-strain-controlled conditions." *Mat. sci. eng.*, 51(1), 55.

Chokshi, A. H., Rosen, A., Karch, J., and Geiter, H. (1989). "On the validity of the Hall-Petch relationship in nanocrystalline materials." *Scr. metall.*, 23, 1679.

Coffin, L. R. J. (1954). "A study of the effects of cyclic thermal stresses on a ductile metal." *Trans. ASME*, 76, 934.

Cook, R. F., and Suo, Z. (2002). "Mechanisms active during fracture under constraint." *MRS Bulletin*, 27(1), 45.

Dehm, G., and Arzt, E. (2000). " In situ transmission electron microscopy study of dislocations in a polycrystalline Cu thin film constrained by a substrate." *Appl. phys. lett.*, 77(8), 1126.

Dehm, G., Balk, T. J., Edongué, H., and Arzt, E. (2003). "Small-scale plasticity in thin Cu and Al films." *Microelectron. eng.*, 70(2-4), 412.

Dehm, G., Wagner, T., Balk, T. J., Arzt, E., and Inkson, B. J. (2002). "Plasticity and interfacial dislocation mechanisms in epitaxial and polycrystalline Al films constrained by substrates." *J. Mater. Sci. Technol.*, 18(2), 113.

Essmann, U., Gösele, U., and Mughrabi, H. (1981). "A model of extrusions and intrusions in fatigued metals." *Philos. mag. A.*, 44(2), 405.

Flinn, J. E., Field, D. P., Korth, G. E., Lillo, T. M., and Macheret, J. (2001). "The flow stress behaviour of OFHC polycrystalline Copper." *Acta mater.*, 49, 2065.

Gao, H., Zhang, L., Nix, W. D., Thompson, C. V., and Arzt, E. (1999). "Crack-like grain-boundary diffusion wedges in thin metal films." *Acta mater.*, 47(10), 2865.

Gastaldi, J., and Jourdan, C. (1981). "Observation by synchrotron x-ray tomography of faceting evolution of grain boundaries during recrystallization." *J. cryst. growth*, 52, 949.

Genin, F. Y. (2001). "Surface morphological evolution of thin films under stress and capillary forces." *Interface Science*, 9(1), 83.

Gleiter, H. (1969). "Theory of grain boundary migration rate." *Acta metall.*, 17, 853.

Gui, X., Haslett, J. W., Dew, S. K., and Brett, M. J. (1998). "Simulation of Temperature Cycling Effects on Electromigration Behavior under pulsed Current Stress." *IEEE trans. electron devices*, 45, 380.

Hadrboletz, A., Weiss, B., and Khatibi, G. (2001). "Fatigue and fracture properties of thin metallic foils." *Int. j. fract.*, 107, 307.

Hommel, M., and Kraft, O. (1999). "A new method to study cyclic deformation of thin films in tension and compression." *J. mater. res.*, 14(6), 2373.

Hommel, M., and Kraft, O. (2001). "Deformation behavior of thin copper films on deformable substrates." *Acta mater.*, 49(19), 3935.

Hong, S., and Weil, R. (1996). "Low cycle fatigue of thin copper foils." *Thin solid films*, 283, 175.

Höppel, H. W., Brunnbauer, M., Mughrabi, H., Valiev, R. Z., and Zhilyaev, A. P. (2000). "Cyclic Deformation Behaviour of Ultrafine Grain Size Copper Produced by Equal Channel Angular Extrusion." *Materials Week - Proceedings*.

Höppel, H. W., and Valiev, R. Z. (2002). "On the possibiliets to enhance the fatigue properties of ultrafine-grained metals." *Z. Metallkd.*, 93, 641.

Höppel, H. W., Zhou, Z. M., Mughrabi, H., and Valiev, R. Z. (2002). "Microstructural study of the parameters governing coarsening and cyclic softening in fatigued ultrafine-grained copper." *Philos. mag. A.*, 82, 1781.

Hu, C. M. (1998). "Reliability Phenomena under AC Stress." *Microelectron. reliab.*, 38(1), 1.

Huang, M., Suo, Z., and Ma, Q. (2002). "Plastic racheting induced cracks in thin film structures." *J. mech. phys. solids*, 50, 1079.

Jackson, M. S., and Li, C.-Y. (1982). "Stress relaxation and hillock growth in thin films." *Acta metall.*, 30(11), 1993.

Jin, N. Y., and Winter, A. T. (1984). "Cyclic deformation of Copper Single Crystals oriented for Double Slip." *Acta metall.*, 32(7), 989.

Judlewicz, M. (1993). "Cyclic deformation of 100µm thin polycrystalline copper foils." *Scr. metall. mater.*, 29, 1463.

Judlewicz, M., Künzi, H. U., Merk, N., and Ilschner, B. (1994). "Microstructural development during fatigue of copper foils 20-100µm thick." *Mat. sci. eng.*, A186, 135.

Keller, R.-M., Baker, S. P., and Arzt, E. (1998). "Quantitative Analysis of Strengthening Mechanisms in Thin Cu Films: Effects of Film Thickness, Grain Size, and Passivation." *J. mater. res.*, 13(7), 1307.

Keller, R.-M., Baker, S. P., and Arzt, E. (1999). "Stress-temperature behavior of unpassivated thin copper films." *Acta mater.*, 47(2), 415.

Keller, R. R., Mönig, R., Volkert, C. A., Arzt, E., Schwaiger, R., and Kraft, O. (2002). "Interconnect Failure due to Cyclic Loading." *Stress-Induced Phenomena in Metallizations: 6th Int'l. Workshop*, Ithaca, NY,AIP, Melville, NY, 119-132.

Klesnil, M., and Lukáš, P. (1980). *Fatigue of metallic materials*, Materials science monographs, Vol. 7, ed. C. Laird, Elsevier, Amsterdam.

Kraft, O., and Arzt, E. (1996). "Electromigration mechanisms in conductor lines: void shape changes and slit-like failure." *Acta mater.*, 45(4), 1599.

Kraft, O., Schwaiger, R., and Wellner, P. (2001). "Fatigue in Thin Films: Lifetime and Damage Formation." *Mat. sci. eng.*, A319-321, 919.

Kraft, O., Wellner, P., Hommel, M., Schwaiger, R., and Arzt, E. (2002). "Fatigue behavior of polycrystalline thin copper films." *Z. Metallkd.*, 93, 392.

Kuan, T. S., and Murakami, M. (1982). "Low temperature strain behavior of Pb thin films on a substrate." *Metall. trans. A*, 13A, 383.

Laird, C. (1983). Dislocations in solids, F. R. N. Nabarro, ed., p. 1, North Holland Publishing Co.

Legros, M., Elliott, B. R., Rittner, M. N., Weertman, J. R., and Hemker, K. J. (2000). "Microsample tensile testing of nanocrystalline metals." *Philos. mag. A.*, 80(4), 1017.

Lukáš, P., and Kunz, L. (1987). "Effect of Grain Size on the High Cycle Fatigue Behaviour of Polycrystalline Copper." *Mat. sci. eng.*, A85, 67.

Ma, B.-T., and Laird, C. (1989). "Overview of fatigue behavior in copper single crystals - I.Surface morphology and stage I crack initiation sites for tests at constant strain amplitude." *Acta metall.*, 37(2), 337.

Manson, S. S. (1954). "Behavior of materials under conditions of thermal stress."National advisory comission on aeronautics, *Report 1170*, Lewis Flight Propulsion Laboratory, Cleveland, OH.

Merchant, H. D., Minor, M. G., and Liu, Y. L. (1999). "Mechanical Fatigue of Thin Copper Foil." *J. electron. mater.*, 28(9), 998.

Mughrabi, H. (1979). "Fatigue Mechanisms." *ASTM STP*, 675, 69.

Mughrabi, H. (1980). "Microscopic mechanisms of metal fatigue." Strength of Metals and Alloys, P. Haasen, V. Gerold, and G. Kostorz, eds., p. 1615-1638, (Proc. of the 5th Intl. Conf. Pergamon Press, Oxford)

Mughrabi, H. (2000). "On the grain-size dependence of metal fatigue: outlook on the fatigue of ultrafine-grained metals." Investigations and Applications of Severe Plastic Deformation, NATO science Series, T. C. Lowe and R. Z. Valiev, eds., p. 241-253, Kluwer Academic Publisher, Dordrecht/Boston/London

Mughrabi, H., and Wang, R. (1988). "Cyclic stress-strain response and high-cycle fatigue behaviour of copper polycrystals." Basic Mechanisms of Fatigue of Metals, P. Lukáš and J. Polák, eds., p. 1-13, Elsevier, Amsterdam

Nix, W. D. (1989). "Mechanical Properties of Thin Films." *Metall. trans.*, 20A, 2217.

Philofsky, E., Ravi, K., Hall, K., and Black, J. (1971). "Surface Reconstruction of Aluminum Metallization - a New Potential Wearout Mechanism." *9th Annual Proceedings of Reliability Physics, IEEE*, 120.

Rae, C. M. F., and Smith, D. A. (1980). "On the mechanisms of grain boundary migration." *Philos. mag. lett.*, 41(4), 477.

Read, D. T. (1998). "Tension-tension fatigue of copper thin films." *Int. j. fatigue*, 20(3), 203.

Schiøtz, J., and Jacobsen, K. W. (2003). "A Maximum in the Strength of Nanocrystalline Copper." *Science*, 301(5), 1359.

Schwaiger, R. (2001). "Fatigue Behavior of Sub-Micron Silver and Copper Films," Ph.D. dissertation, Universität Stuttgart, Institut für Metallkunde.

Schwaiger, R., Dehm, G., and Kraft, O. (2003). "Cyclic deformation of polycrystalline Cu films." *Philos. mag. A.*, 83(6), 693.

Schwaiger, R., and Kraft, O. (1999). "High Cycle Fatigue of Thin Silver Films Investigated by Dynamic Microbeam Deflection." *Scr. mater.*, 41, 823.

Schwaiger, R., and Kraft, O. (2003). "Size effects in the fatigue behavior of thin Ag films." *Acta mater.*, 51(1), 195.

Sekiguchi, A., Koike, J., Kamiya, S., Saka, M., and Maruyama, K. (2001). "Void formation by thermal stress concentration at twin interfaces in Cu thin films." *Appl. phys. lett.*, 79, 1264.

Snowden, K. U. (1981). "The formation of boundary serrations and cavities during high-temperature fatigue." *Met. forum*, 4(1-2), 106.

Snowden, K. U., Stathers, P. A., and Hughes, D. S. (1976). "Grain-boundary migration in metals fatigued at high temperatures." *Nature*, 261(5558), 306.

Subramanian, K. N., Lee, A., Choi, S., and Sonje, P. (2001). "Material issues in electronic interconnects and packaging." *J. electron. mater.*, 30(4), 372.

Suresh, S. (1998). *Fatigue of materials*, 1st edition, Cambridge University Press, New York, NY.

Suresh, S., Giannakopoulos, A. E., and Olsson, M. (1994). "Elastoplastic analysis of thermal cycling: layered materials with sharp interfaces." *J. mech. phys. solids*, 42, 979.

Sutton, A. P., and Baluffi, R. W. (1995). *Interfaces in Crystalline Materials*, Clarendon Press, Oxford.

Thiele, E., Holste, C., and Klemm, R. (2002). "Influence of size effect on microstructural changes in cyclically deformed polycrystalline nickel." *Z. Metallkd.*, 93(7), 730.

Thompson, A. W., and Backofen, W. A. (1971). "The effect of grain size on fatigue." *Acta metall.*, 19, 597.

Thompson, C. V. (1993). "The Yield Stress of Polycrystalline Thin Films." *J. mater. res.*, 8(2), 237.

Thouless, M. D., Gupta, J., and Harper, J. M. E. (1993). "Stress development and relaxation in copper films during thermal cycling." *J. mater. res.*, 8(8), 1845.

v. Blanckenhagen, B. (2002). "Versetzungen in dünnen Metallschichten," Ph.D. dissertation, Universität Stuttgart, Institut für Metallkunde.

Valiev, R. Z., Krasilnikov, N. A., and Tsenev, N. K. (1991). "Plastic deformation of alloys with submicron-grained structure." *Mat. sci. eng.*, A137, 35.

Venkatraman, R., and Bravman, J. C. (1992). "Separation of film thickness and grain boundary strengthening effects in Al thin films on Si." *J. mater. res.*, 7(8), 2040.

Vinci, R. P., Forrest, S. A., and Bravman, J. C. (2002). "Effect of interface conditions on yield behavior of passivated copper thin films." *J. mater. res.*, 17(7), 1863.

Vinogradov, A. Y., and Hashimoto, S. (2001). "Multiscale phenomena in fatigue of ultra-fine grain materials-an overview." *Mater. trans.*, 42(1), 74.

Weertman, J. R. (1993). "Hall-Petch strengthening in nanocrystalline metals." *Mat. sci. eng.*, A166(1-2), 161.

Weiss, D., Gao, H., and Arzt, E. (2001). "Constrained diffusional creep in UHV-produced copper thin films." *Acta mater.*, 49(13), 2395.

Wigmore, G., and Smith, G. C. (1971). "The low-cycle fatigue behaviour of copper at elevated temperatures." *Met. sci. j.*, 5, 58.

Williams, H. D., and Corti, C. W. (1968). "Grain-boundary migration and cavitation during fatigue." *Met. sci. j.*, 2, 28.

Zhang, G. P. (2003) private communication

Zhang, G. P., Schwaiger, R., Volkert, C. A., and Kraft, O. (2003). "Effect of film thickness and grain size on fatigue-induced dislocation structures in thin Cu films." *Philos. mag. lett.*, 83(8), 477.

Zhang, G. P., Volkert, C. A., Schwaiger, R., Arzt, E., and Kraft, O. (2004). "Damage Behaviour of 200 nm thick Cu Films under cyclic Loading." *To be published*.

Appendices

Appendix A.

Active glide systems in thin films on thick substrates

an analytical calculation for the stresses in grains with different orientations.

------Original Mathematica notebook can be obtained from author.

In order to discuss the fatigue damage in thin films on substrates, the stress state in the thin films needs to be understookd in detail. Despite the need for this information, such a calculation is not available in the literature, probably because it is complex and complicated. Below is a brief description of a Mathematica notebook that was written to calculate Schmid factors (A1) and the stress state in a film under biaxial strain (A2). The last three sections (A3-A5) are spent in calculating the resolved shear stresses on the slip systems and developing tools to visualize the active slip systems. These calculations are essential for discussing details of dislocation interactions with other dislocations and with grain and twin boundaries.

A1. Schmid factors for grains with different orientations in fcc metals under equibiaxial stress

```
<< LabelContour.m
```

The simple stress state

If the stress state of a sample is given, the resolved shear stresses can be easily calculated.

$$\text{Ssample} = \begin{pmatrix} 1 & 0 & 0 \\ 0 & 1 & 0 \\ 0 & 0 & 0 \end{pmatrix};$$

"Ssample" is the assumed stress in the film coordinate system. The film is under equibiaxial stress. There are no stresses perpendicular to the film plane (z direction). Since this problem is linear, the components of Ssample will be set to "1".

$$\text{Rot}[\alpha\_, \beta\_, \gamma\_] = \begin{pmatrix} \text{Cos}[\gamma]\,\text{Cos}[\alpha] - \text{Sin}[\gamma]\,\text{Cos}[\beta]\,\text{Sin}[\alpha] & \text{Cos}[\gamma]\,\text{Sin}[\alpha] + \text{Sin}[\gamma]\,\text{Cos}[\beta]\,\text{Cos}[\alpha] & \text{Sin}[\gamma]\,\text{Sin}[\beta] \\ -\text{Sin}[\gamma]\,\text{Cos}[\alpha] - \text{Cos}[\gamma]\,\text{Cos}[\beta]\,\text{Sin}[\alpha] & -\text{Sin}[\gamma]\,\text{Sin}[\alpha] + \text{Cos}[\gamma]\,\text{Cos}[\beta]\,\text{Cos}[\alpha] & \text{Cos}[\gamma]\,\text{Sin}[\beta] \\ \text{Sin}[\beta]\,\text{Sin}[\alpha] & -\text{Sin}[\beta]\,\text{Cos}[\alpha] & \text{Cos}[\beta] \end{pmatrix};$$

```
Sigmagrain[α_, β_, γ_] =
  Simplify[{(Rot[α, β, γ]).Ssample.Transpose[Rot[α, β, γ]]}];
```

"Sigmagrain" is the stress in the (coordinate system of the) grain, which is rotated by the Euler angles α, β and γ relative to the sample coordinates.

The resolved shear stresses on the glide systems in the fcc metal -> Schmid factors

Typically Schmid factors are calculated by a product of two cosines. Here the Schmid factors will be determined by calculating the traction of the stress on the slip systems. The use of vector operations has the advantage that all of the geometric considerations will be done intrinsically. The method is

therefore more flexible and can be applied to complicated stress states (more about that will be shown in section A3).

For the calculation of the Schmid factors, all possible independent slip systems will be considered. The glide planes and the Burgers' vectors are displayed as columns of the matrices below.

```
plane = {{1, 1, 1, -1}, {1, -1, 1, 1}, {1, 1, -1, 1}} / Sqrt[3];

burgers = {{1, 1, 1, 1, 0, 0}, {1, -1, 0, 0, 1, 1}, {0, 0, 1, -1, 1, -1}} / Sqrt[2];
```

During this section, the resolved shear stress equals the Schmid factor, because the components of the stress tensor "Sigmasample" have been set to "1". The calculation of the resolved stress on a single slip system (traction) is performed with the function "trakt[pl,bu]" defined below. A list of all resolved shear stresses (=Schmid factors) "T[α,β,γ]" on the 12 slip systems will be calculated.

```
T[α_, β_, γ_] := Module[{grainstress, pl, bu},
  grainstress = Sigmagrain[α, β, γ];
  trakt[pl_, bu_] := (grainstress.plane[[All, pl]]).burgers[[All, bu]];
  Flatten[{trakt[1, {2, 4, 6}], trakt[2, {1, 4, 5}], trakt[3, {2, 3, 5}],
    trakt[4, {1, 3, 6}]}]]

 Tm[α_, β_, γ_] := Max[Abs[T[α, β, γ]]]
```

"Tm[α,β,γ]" provides the maximum absolute value of the 12 resolved shear stresses for a particularly oriented grain. Absolute value function "Abs" is used because the sign of the shear stress should not matter - the dislocations just move in opposite directions. Because of symmetry, the results only depend on the out-of-plane orientation of the grains (the angles β and γ) and not on the in-plane orientation (angle α). Therefore the results can be plotted onto a stereographic projection. For this projection, Euler angles are not useful and Euler angles will be transformed to vector components (x,y) of the out-of-plane (oop) orientation of the grains. This is performed by "ArcSin" and "ArcCos" functions below.

The function "Tm1" contains the highest absolute value of all Schmid factors (=shear stress) and "T1" gives a list (12 elements) of the Schmid factors (or shear stresses) of all glide systems for a given out-of-plane orientation of (x,y,u). The (x,y,u) vector is required to lie on the unit sphere. Therefore only x and y need to be provided and u is implicitly chosen so that x^2+y^2+u^2=1 is fulfilled.

```
Tm1[x_, y_] := Tm[0, ArcSin[Sqrt[x^2 + y^2]], ArcCos[y / Sqrt[x^2 + y^2]]];

T1[x_, y_] := T[0, ArcSin[Sqrt[x^2 + y^2]], ArcCos[y / Sqrt[x^2 + y^2]]]
```

To go from the spherical projection defined above to a stereographic projection, a coordinate transform will be made. x,y are the coordinates on the unit sphere and x1,y1 are coordinates on the z=0 plane of the stereographic projection :

```
x = x1 * (1 + (1 - x1^2 - y1^2) / (1 + x1^2 + y1^2));
y = y1 * (1 + (1 - x1^2 - y1^2) / (1 + x1^2 + y1^2));
```

Plots of the Schmid factor

"Unittriang" is a function that restricts a function "F" onto the standard orientation triangle (<001>, <101>, <111>). Outside the unit triangle Unittriang is zero.

```
Unittriang[x_, y_, F_] :=
 Module[{}, If[(UnitStep[x - y] * UnitStep[Sqrt[1 - (x^2 + y^2)] - x]) == 1,
   F[x, y], 0]]
```

Pltstrgrph[T] is a Module that plots Function T on a labelled contour plot.

```
<< Statistics`DescriptiveStatistics`

Pltstrgrph[T_] := Module[{Mx}, Dat = Table[If[(x^2 + y^2) < 1, T[x, y], T[0.001, 0.001]], {x, 0.001, .99, .02}, {y, 0.001, .99, .02}];;
  Print["Minimum :", Min[Dat], "      Maximum: ", Max[Dat], "       Mean value:", Mean[Flatten[Dat]]];
  plopt = {Min[Dat] * 0.64, Max[Dat] * 1.042}; x = x1 * (1 + (1 - x1^2 - y1^2) / (1 + x1^2 + y1^2)); y = y1 * (1 + (1 - x1^2 - y1^2) / (1 + x1^2 + y1^2));
  aaa = ContourPlot[Unittriang[x, y, T], {x1, 0.0001, Sqrt[2.] - 1}, {y1, 0.0001, Sqrt[2.] - 1}, Contours → 30, PlotPoints → 200,
    ContourShading → False, ContourStyle -> {{GrayLevel[0.5]}}, DisplayFunction → Identity];
  LabelContourLines[aaa, LabelPlacement → Automatic, DisplayFunction -> $DisplayFunction, PointFactor → 2];]
```

```
Pltstrgrph[Tm1]
```

Minimum :0.278182 Maximum: 0.499886 Mean value:0.441928

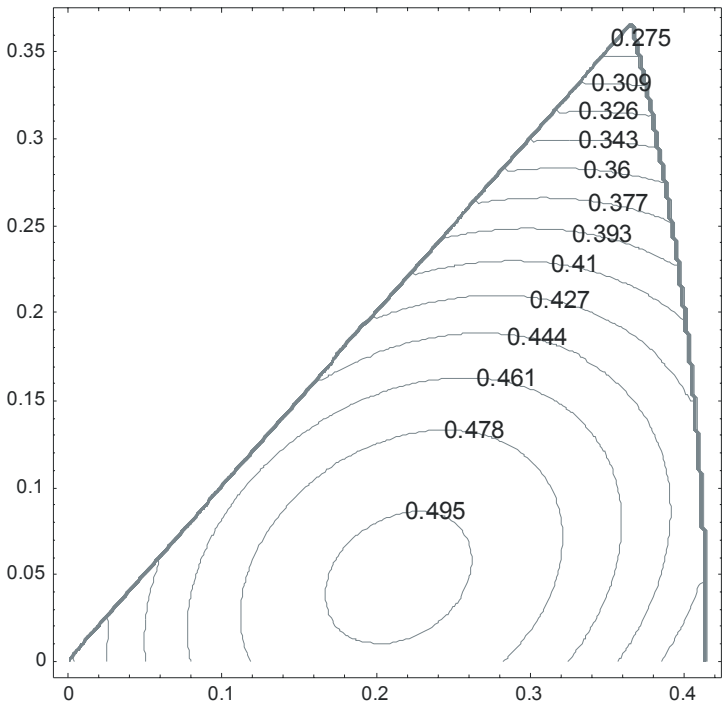

This is a stereographic projection of the dependence of the highest Schmid factors on the out-of-plane grain orientation of a film under equibiaxial stress.

A2. Calculation of the Stress state of a thin film for given equibiaxial strain and zero out-of-plane stress

The film is on a substrate that is thick compared to the film itself. Strains in the film will occur, when the substrate is bend or during heating/cooling because of the mismatch in the thermal expansion coefficients between film and substrate. All stresses that occur lie in the plane of the film. Generally the stresses in the individual grains of a polycrystalline film cannot be calculated analytically because of the variation in the elastic moduli between different grains. The strain in the grains is determined by the substrate and different grain orientations will have different stresses depending on the elastic

anisotropy of the material. Because the stresses are required to be continuous, complicated elastic interactions between the grains will occur. There are two limiting cases where simplifications can be made and the mean stress in a film can be calculated without help from finite element analysis.

First, if the grain size is much smaller than the thickness of the film, then all of the grains can be considered to be under the same stress. This case was calculated in section A1 and its results are proportional to the Schmid factor plot.

Second, if the grain size is large compared to the thickness of the film, all grains can be considered to have the same strain state. This case is very important for this work and occurs typically in annealed films which typically have large grains compared to the film thickness. The inner part of the grains (more than the length of the film thickness apart from the grain boundary) can be assumed to be under biaxial strain and the stress in this region can be analytically calculated just from the strain and the elastic constants. The higher the ratio of grain size to film thickness, the better is the agreement of the calculation that follows with the mean stresses in a thin film.

Elastic constants of Cu (unit GPa) (the metal can be changed by changing the elastic constants, e.g. Al: c11=108; c12=61; c44=29 which is more isotropic and will give a completely different behaviour):

```
c11 = 168; c12 = 121; c44 = 75;
```

Strain: The strain in-plane is given by the substrate and the strain out-of-plane is not controlled by the substrate and is not known at this time.

Stress: For the thin film there is no stress is acting perpendicular to its surface -> the z components of the stress are zero. The remaining part of the stress tensor is not known at this point.

Everything is elastic (linear) and the strain of the film will be set to 1 (equibiaxial in x and y; out-of-plane (z) strain components: "ar" are not known at the moment). The Stress in z direction is 0, remaining stress components "br" are not known. (strain and stress are symmetric tensors and therefore maximum allowed number of components of ar and br together are 6.)

```
ar = {ar1, ar2, ar3}; br = {br1, br2, br3};
```

$$\text{Strain} = \begin{pmatrix} 1 & 0 & ar1 \\ 0 & 1 & ar2 \\ ar1 & ar2 & ar3 \end{pmatrix};$$

$$\text{Stress} = \begin{pmatrix} br1 & br2 & 0 \\ br2 & br3 & 0 \\ 0 & 0 & 0 \end{pmatrix};$$

To calculate the stresses in the grains, the coordinate system of the sample needs to be rotated into the coordinate system of the grain.

As in section A1, "Rot" is a rotation matrix for coordinate transformation (Euler angles are in Bunge notation: α, β and γ. The coordinate system of the grain is rotated relative to the sample system by this matrix. Euler angle "α" (is related to in-plane orientation of grain) and is not necessary for the film, because of the symmetry (equibiaxial strain). "α" will be set to zero in the following calculation. ("α"

is still there, because this notebook is designed for general calculations (3D stress-strain) and in principle three Euler angles can be used for other stress and strain constraints. – Appendix B)
"sa" stands for "Sin[α]" and "ca" stands for "Cos[α]" and are only introduced to gain speed in the extensive tensor transformations that will follow.

```
Rot[ca_, sa_, cb_, sb_, cc_, sc_] =
 ( cc*ca - sc*cb*sa  |  cc*sa + sc*cb*ca  |  sc*sb
  -sc*ca - cc*cb*sa  | -sc*sa + cc*cb*ca  |  cc*sb
       sb*sa         |       -sb*ca       |   cb   );
```

The stiffness tensor of the material in the film (cubic symmetry):

```
MatrixForm[
 stiffntens =
  Table[KroneckerDelta[i, j]*KroneckerDelta[k, l]*
     (c12 + KroneckerDelta[i, k] (c11 - c12)) +
    c44*(KroneckerDelta[i + j, 3]*KroneckerDelta[k + l, 3] +
       KroneckerDelta[i + j, 5]*KroneckerDelta[k + l, 5] +
       KroneckerDelta[i + j, 4]*KroneckerDelta[k + l, 4] *
        KroneckerDelta[Abs[i - j], 2]*KroneckerDelta[Abs[k - l], 2]),
   {i, 3}, {j, 3}, {k, 3}, {l, 3}]]
```

$$\begin{pmatrix} \begin{pmatrix} 168 & 0 & 0 \\ 0 & 121 & 0 \\ 0 & 0 & 121 \end{pmatrix} & \begin{pmatrix} 0 & 75 & 0 \\ 75 & 0 & 0 \\ 0 & 0 & 0 \end{pmatrix} & \begin{pmatrix} 0 & 0 & 75 \\ 0 & 0 & 0 \\ 75 & 0 & 0 \end{pmatrix} \\ \begin{pmatrix} 0 & 75 & 0 \\ 75 & 0 & 0 \\ 0 & 0 & 0 \end{pmatrix} & \begin{pmatrix} 121 & 0 & 0 \\ 0 & 168 & 0 \\ 0 & 0 & 121 \end{pmatrix} & \begin{pmatrix} 0 & 0 & 0 \\ 0 & 0 & 75 \\ 0 & 75 & 0 \end{pmatrix} \\ \begin{pmatrix} 0 & 0 & 75 \\ 0 & 0 & 0 \\ 75 & 0 & 0 \end{pmatrix} & \begin{pmatrix} 0 & 0 & 0 \\ 0 & 0 & 75 \\ 0 & 75 & 0 \end{pmatrix} & \begin{pmatrix} 121 & 0 & 0 \\ 0 & 121 & 0 \\ 0 & 0 & 168 \end{pmatrix} \end{pmatrix}$$

The stiffness tensor is rotated from the sample system into coordinate system of the grain (by the Euler rotation).

From here on the results of individual steps will not be plotted (";" at the end of expressions is used) since the equations and tensors are too long (many pages of mainly cosines and sines).)

```
stiffntensrot[ca_, sa_, cb_, sb_, cc_, sc_] =
  Simplify[
   Inner[Times,
    Inner[Times,
     Simplify[Inner[Times,
       Simplify[Inner[Times, stiffntens, Rot[ca, sa, cb, sb, cc, sc],
         Plus, 4]], Rot[ca, sa, cb, sb, cc, sc], Plus, 3]],
     Rot[ca, sa, cb, sb, cc, sc], Plus, 2], Rot[ca, sa, cb, sb, cc, sc],
    Plus, 1]];
```

The stress tensor in the sample coordinates is the product of the stiffness tensor and the strain tensor The stress depends on the 3 Euler angles and the three strain components "ar", which are still not known at this point.

```
Sigmasample[ca_, sa_, cb_, sb_, cc_, sc_] =
  Simplify[
   Sum[Sum[stiffntensrot[ca, sa, cb, sb, cc, sc][[o, p]] Strain[[o, p]],
     {p, 3}], {o, 3}]];
```

Both matrices (Strain and Stress) have to be fulfilled by the solution.

It follows a calculation of missing strain components ar1 to ar3. "Solution1" contains the three "ar" values in terms of the 3 Euler angles *(very long (20-30 pages) and can be simplified for a much faster calculation). This process needs some computation time (equation with an 81 component tensor, each component containing many sine and cosine functions has to be solved (~2 min at CPU with 1GHz)).*

"Sigmasampleplanestress" is the solution and contains the stress tensor in the sample coordinate system as a function of the Euler angles.

```
<< LinearAlgebra`MatrixManipulation`

Solutionstrain =
  Simplify[
   Solve[
    UpperDiagonalMatrix[
      (Sigmasample[ca, sa, cb, sb, cc, sc] - Stress)[[#1, #2]] &, 3] == 0,
    ar, br, InverseFunctions → True]];

Sigmasampleplanestress[ca_, sa_, cb_, sb_, cc_, sc_] =
  Simplify[(Sigmasample[ca, sa, cb, sb, cc, sc] /. Solutionstrain)[[1, All]]];

sa = Sin[α]; ca = Cos[α]; sb = Sin[β]; cb = Cos[β]; sc = Sin[γ];
cc = Cos[γ];
```

The definitions made before in section A1 will be removed and the stress is set to the result just obtained. "Sigmasample" is the stress in the film and depends on the Euler angles of the grain.

```
Clear[Sigmasample, Sigmagrain];
Sigmasample[α_, β_, γ_] =
 Simplify[Sigmasampleplanestress[ca, sa, cb, sb, cc, sc], Trig → True];
```

"Sigmagrain" is the stress in the (coordinate system of the) grain; coordinate system is rotated by the Euler angles.

```
Sigmagrain[α_, β_, γ_] =
  Simplify[(Rot[ca, sa, cb, sb, cc, sc]).Sigmasample[α, β, γ].
    Transpose[Rot[ca, sa, cb, sb, cc, sc]], Trig → True];
```

"Sigmagrain" is the time limiting calculation of this notebook and needs to be highly optimized for speed (computation time was decreased by optimization by a factor of ~10^3 from 14s to ~5ms on a 1GHz CPU).

Stress in the film -> Hydrostatic stress and biaxial Modulus

From the results above, a plot of the hydrostatic stress for different out-of-plane orientations can be made. The Hydrostatic stress is 1/3 of the trace of the stress tensor. The biaxial modulus is only

defined for <100> and <111> out-of-plane orientations, where there is in-plane isotropy. Since The z components of the stress tensor are zero and the strain was set to 1, 3/2*Hydstress gives the biaxial modulus for <100> and <111>.

Because of symmetry, the results do not depend on Euler angle "α" and "α" is set to zero.

For spherical projection, Euler angles are not suitable. Again the components of the out-of-plane orientation (x, y, u) of the grain will be used ("ArcSin","ArCos").

```
Hydstress[x_, y_] :=
 Module[{spng1},
  spng1 = Sigmasample[0, ArcSin[Sqrt[x^2 + y^2]], ArcCos[y / Sqrt[x^2 + y^2]]];
  (spng1[[1, 1]] + spng1[[2, 2]]) / 3]
```

Since strain was set to 1, the values of the plot are proportional to the hydrostatic stress (=Modbi*2/3): In general: hydrostatic stress in a film= 2/3* effective modulus * strain. The values below are in GPa because the strain was set to 1. Everything can be divided by 10^3: strain is the 0.1% and the plot belo is in MPa.

```
Pltstrgrph[Hydstress]
```

Minimum :76.4685 Maximum: 173.219 Mean value:119.092

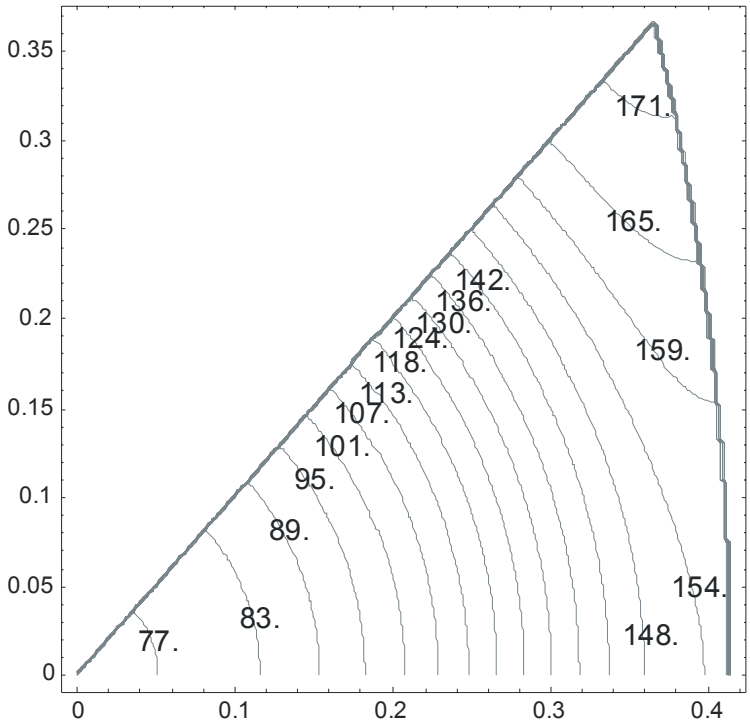

Values for the biaxial modulus <100>(isotropy) and <111>(isotropy) in GPa:

```
Print["<100> ", 3 / 2 * Hydstress[0.00001, 0.00001], "          <111> ",
 3 / 2 * Hydstress[.5773502691896258`, 0.5773502691896258`]]
```

<100> 114.702 <111> 259.859

Effective modulus for an untextured film (3/2*mean value): 178.6

A3. The Resolved shear stresses on the glide systems for Cu

Now the stresses of the individual grains are known and the shear stress on the slip systems can be calculated. Therefore the method developed for the Schmid factors in section A1 can be used. The only difference is that the stress tensor "Sigmasample" and "Sigmagrain" were changed to the results from section A2.

```
Pltstrgrph[Tm1]
```

Minimum :46.874 Maximum: 86.4535 Mean value:69.6736

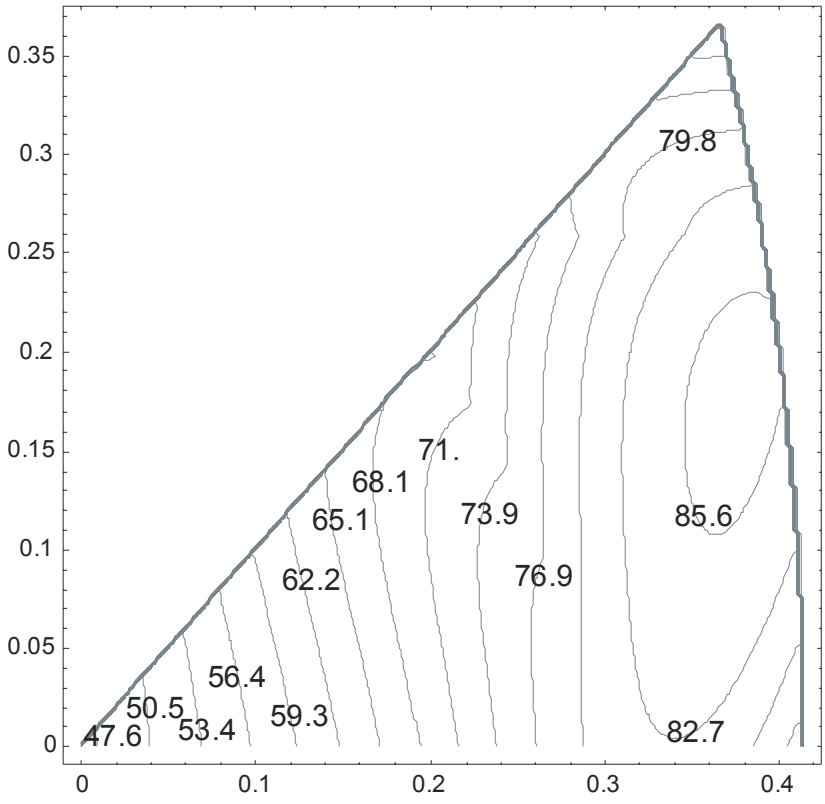


```
anisotropy = (c11 - c12) / 2 / c44
```

$$\frac{47}{150}$$

This plot differs significantly from the plot of the Schmid factors because of the large anisotropy in the elasticity of Cu. If the elastic constants of Al were used in section A2, the shape of these plots would have agreed fairly well with the Schmid factor plot from section A1.

A4. A Map of the active slip systems in Cu

This section was developed to detect changes in the active slip system for different grain orientations. In the calculation each slip system is identified by a fixed number (between 1 and 12). The position of the slip system with the highest resolved shear stresses in the list of all glide systems is detected and used as an identification number.

```
ListofPositionsExact[x_, y_] :=
 Module[{trakt}, trakt = T1[x, y];
  Flatten[Position[Abs[trakt], Max[Abs[trakt]]]]]

IdentSlipExact[x_, y_] := Apply[Plus, Flatten[ListofPositionsExact[x, y]]]
```

It follows a stereographic plot of the change in the active slip system. The horizontal axis corresponds to the direction between <001> and <101> and the vertical axis corresponds to directions from <001> to <011> of the out-of-plane orientation of the grain. (*This plot consumes same computation power as plots above: decrease PlotPoints if necessary*)

```
Exakt =
  ContourPlot[IdentSlipExact[x1 * (1 + (1 - x1^2 - y1^2) / (1 + x1^2 + y1^2)),
    y1 * (1 + (1 - x1^2 - y1^2) / (1 + x1^2 + y1^2))], {x1, 0.0001, Sqrt[2.] - 1},
   {y1, 0.0001, Sqrt[2.] - 1}, Contours → 15, PlotPoints → 300,
   ContourShading → False];
```

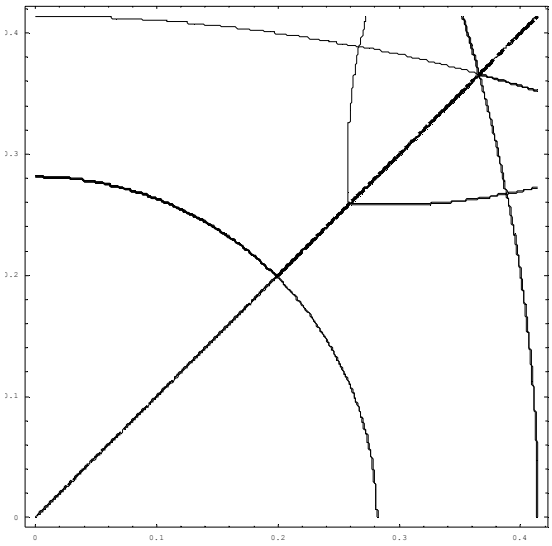

Again the plot is strongly influenced by elastic anisotropy. For Cu 3 different slip systems are active within the unit triangle. For Al just one slip system is active.

A5. Plots of data for particular orientations (Module)

Here a module is set up to print values of the resolved shear stress and corresponding glide system(s) for a particular orientation and to visualize the glide planes and Burgers' vectors in the film to get an idea of the different slip geometries. This module is about two pages long and only its results will be shown in this Appendix. It can be found in the original Mathematica notebook, which can be obtained from the author.

The module prints data for a given orientation and draws plots with the active glide systems. In these plots the film is seen along its surface normal from above. The crystal axes of the grain are oriented along the axes of a cube that will be plotted as a wireframe. Different glide planes are shown with different grey levels and are not transparent. This helps to identify the grain orientation. The

active Burgers' vectors will be displayed as a black line and during glide the part above the plane in the images glides along the Burgers' vector towards the black point.

Detailed information about every glide system is only printed out when parameter "additionalinfo" is set to "yes".

Module (Tm3[{out-of-plane}{in-plane along line}]) applied to a <111> grain (many active glide systems):

```
additionalinfo = "no"; Info[{1., 1., 1.}, {1., -1., 0.000001}]

In plane direction {0.707107, -0.707107, 4.71405×10^-7} will be used.

Diagram coordinates     x: 0.57735 and  y: 0.57735

Euler angles            α: -7.06824×10^-7     β: 0.955317     γ: 0.785398

{0, 0, 1} -> {0.57735, 0.57735, 0.57735} , {0, 1, 0} -> {0.408248, 0.408249, -0.816497} , {1, 0, 0} -> {0.707107, -0.707106, -5.77119×10^-7}

Resolved shear stresses for this orientation:
 {1.74059×10^-14, -3.48119×10^-14, -5.22178×10^-14,
  -70.7247, 1.00475×10^-14, -70.7247, -2.0095×10^-14,
  -70.7247, -70.7247, -70.7247, -70.7247, 3.01495×10^-14}

Highest resolved shear stress for this orientation: 70.7247

Number of active slip systems with this shear stress: 6

Identification number(s) of active glide system(s): {4, 6, 8, 9, 10, 11}
```

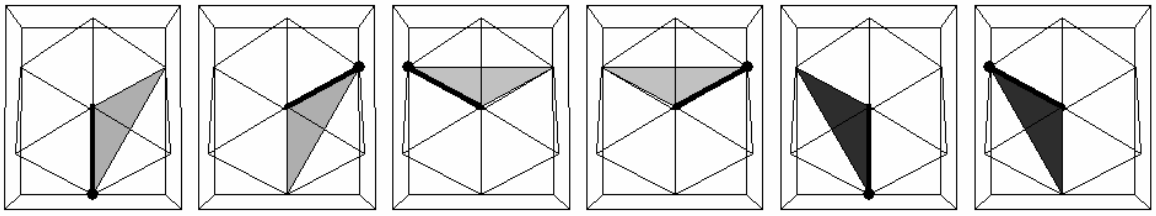

Module applied to a<001>grain (many active glide systems, low resolved shear stress in Cu):

```
additionalinfo = "no"; Info[0., 0., 0.]

Diagram coordinates     x: 0. and  y: 0.

Euler angles            α: 0.     β: 0.     γ: 0.

{0, 0, 1} -> {0., 0., 1.} , {0, 1, 0} -> {0., 1., 0.} , {1, 0, 0} -> {1., 0., 0.}

Resolved shear stresses for this orientation: {0., 46.8271, 46.8271,
  0., 46.8271, -46.8271, 0., 46.8271, 46.8271, 0., -46.8271, 46.8271}

Highest resolved shear stress for this orientation: 46.8271

Number of active slip systems with this shear stress: 8

Identification number(s) of active glide system(s):
 {2, 3, 5, 6, 8, 9, 11, 12}
```

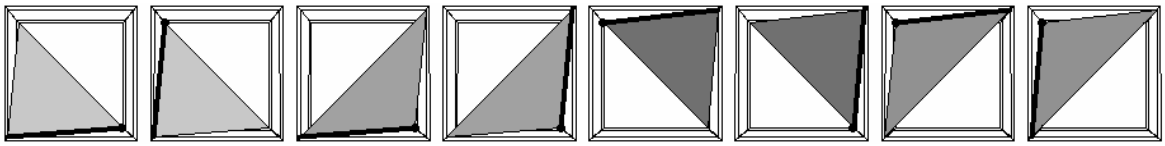

Applied to a twin in a <001> grain (<221> out-of-plane orientation, very high resolved shear stress in Cu, only two slip systems glide parallel to the twining plane (1-11)):

```
additionalinfo = "yes"; Info[{2., 1., 2.}, {2., -2., -1.}]
```

In plane direction {0.666667, -0.666667, -0.333333} will be used.

Diagram coordinates x: 0.666667 and y: 0.333333

Euler angles α: -0.463648 β: 0.841069 γ: 1.10715

$$\begin{pmatrix}0\\0\\1\end{pmatrix} \to \begin{pmatrix}0.666667\\0.333333\\0.666667\end{pmatrix}, \begin{pmatrix}0\\1\\0\end{pmatrix} \to \begin{pmatrix}0.333333\\0.666667\\-0.666667\end{pmatrix}, \begin{pmatrix}1\\0\\0\end{pmatrix} \to \begin{pmatrix}0.666667\\-0.666667\\-0.333333\end{pmatrix}$$

Resolved shear stresses for this orientation:

{-47.6953, 2.51275×10^{-15}, 47.6953, -85.8516, -5.02376×10^{-15}, -85.8516, 18.7011, -38.1563, -56.8574, -56.8574, -38.1563, -18.7011}

Highest resolved shear stress for this orientation: 85.8516

Number of active slip systems with this shear stress: 2

Identification number(s) of active glide system(s): {4, 6}

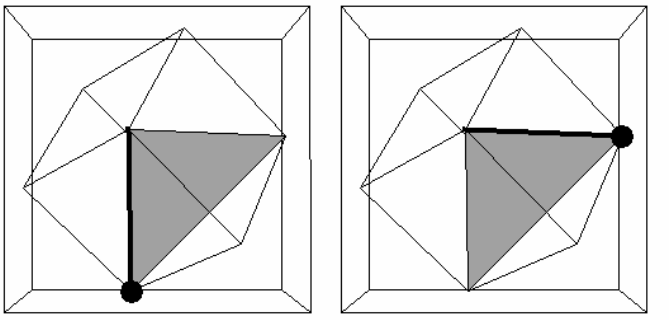

Glide system 4:

resolved shear stress: -85.8516

$$\text{Glide plane}: \begin{pmatrix}\frac{1}{\sqrt{3}}\\-\frac{1}{\sqrt{3}}\\\frac{1}{\sqrt{3}}\end{pmatrix} \quad \text{burgers vektor}: \begin{pmatrix}\frac{1}{\sqrt{2}}\\\frac{1}{\sqrt{2}}\\0\end{pmatrix} \quad \text{dislocation}: \begin{pmatrix}-\frac{1}{\sqrt{6}}\\\frac{1}{\sqrt{6}}\\\sqrt{\frac{2}{3}}\end{pmatrix}$$

Glide system 6:

resolved shear stress: -85.8516

$$\text{Glide plane}: \begin{pmatrix}\frac{1}{\sqrt{3}}\\-\frac{1}{\sqrt{3}}\\\frac{1}{\sqrt{3}}\end{pmatrix} \quad \text{burgers vektor}: \begin{pmatrix}0\\\frac{1}{\sqrt{2}}\\\frac{1}{\sqrt{2}}\end{pmatrix} \quad \text{dislocation}: \begin{pmatrix}-\sqrt{\frac{2}{3}}\\-\frac{1}{\sqrt{6}}\\\frac{1}{\sqrt{6}}\end{pmatrix}$$

Applied to a twin in a<111>grain (<1-15>out-of-plane orientation, twining plane is (-111)):

```
additionalinfo = "yes"; Info[{1., -1., 5.}, {1., -4., -1.}]
In plane direction {0.235702, -0.942809, -0.235702} will be used.
Diagram coordinates     x: 0.19245 and  y: -0.19245
Euler angles            α: -1.0472     β: 0.275643     γ: 2.35619
```

$$\begin{pmatrix}0\\0\\1\end{pmatrix} \text{ -> } \begin{pmatrix}0.19245\\-0.19245\\0.96225\end{pmatrix}, \quad \begin{pmatrix}0\\1\\0\end{pmatrix} \text{ -> } \begin{pmatrix}0.952579\\0.272166\\-0.136083\end{pmatrix}, \quad \begin{pmatrix}1\\0\\0\end{pmatrix} \text{ -> } \begin{pmatrix}0.235702\\-0.942809\\-0.235702\end{pmatrix}$$

```
Resolved shear stresses for this orientation:
 {-21.1459, 34.672, 55.8179, -5.02376×10^-15, 59.2087, -59.2087,
  21.1459, 55.8179, 34.672, -1.00475×10^-14, -38.0627, 38.0627}
Highest resolved shear stress for this orientation: 59.2087
Number of active slip systems with this shear stress: 2
Identification number(s) of active glide system(s): {5, 6}
```

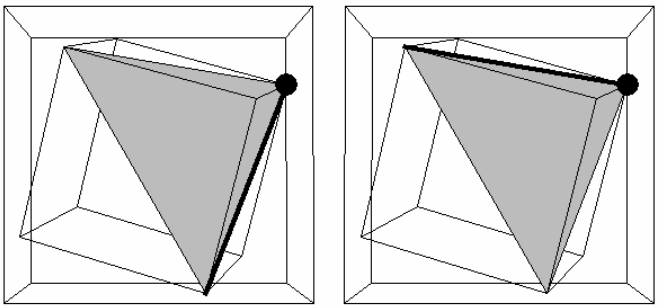

```
resolved shear stress: 59.2087
```

$$\text{Glide plane : } \begin{pmatrix}\frac{1}{\sqrt{3}}\\-\frac{1}{\sqrt{3}}\\\frac{1}{\sqrt{3}}\end{pmatrix} \quad \text{burgers vektor : } \begin{pmatrix}\frac{1}{\sqrt{2}}\\0\\-\frac{1}{\sqrt{2}}\end{pmatrix} \quad \text{dislocation : } \begin{pmatrix}\frac{1}{\sqrt{6}}\\\sqrt{\frac{2}{3}}\\\frac{1}{\sqrt{6}}\end{pmatrix}$$

```
Glide system 6:
     resolved shear stress: -59.2087
```

$$\text{Glide plane : } \begin{pmatrix}\frac{1}{\sqrt{3}}\\-\frac{1}{\sqrt{3}}\\\frac{1}{\sqrt{3}}\end{pmatrix} \quad \text{burgers vektor : } \begin{pmatrix}0\\\frac{1}{\sqrt{2}}\\\frac{1}{\sqrt{2}}\end{pmatrix} \quad \text{dislocation : } \begin{pmatrix}-\sqrt{\frac{2}{3}}\\-\frac{1}{\sqrt{6}}\\\frac{1}{\sqrt{6}}\end{pmatrix}$$

If one considers the active slip systems in the matrix and those of the corresponding twins in the plots above, it can be seen that the active glide planes of the twins of <100> grains lie in the twinning plane and have the same Burgers' vectors. For <111> grains this is not the case and the glide planes of matrix and twins have different glide systems. Therefore dislocations can be transmitted across twin boundaries in <100> grains, whereas in <111> grains this is not possible.

Appendix B.

Deviations from film stresses in the wide and thin Cu lines

The stress state of a metal line on a substrate is different from that of a thin film. To investigate this difference, a two dimensional finite element stress analysis (FEA) was performed. Stresses in the films or lines are caused by the different thermal expansion coefficients of the film or line and the substrate. In order to generate stresses in a Cu metal line on a Si or sapphire substrate, a temperature change of 100 K was applied to an initially stress free state. The values used for the thermal expansion coefficients and elastic constants of the Cu, Si and sapphire are shown in Table B1.

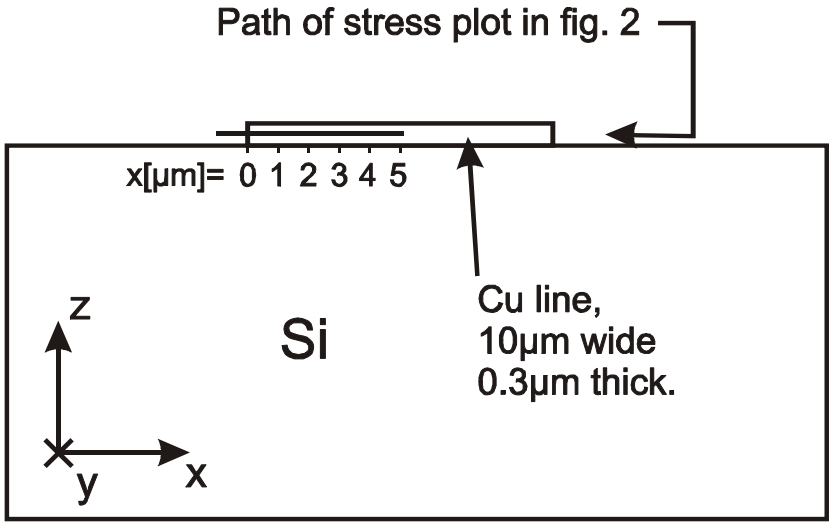

Fig. B.1
Geometry of the 2D plane strain model of the line.

The geometry shown in Fig. B.1 was used for the FEA calculations (Cu line is 10 µm wide and 0.3 µm thick). The values of the three principal stresses along the path indicated in Fig. B.1 are displayed in Fig. B.2. The highest stresses occur for the y component (along line length). The stresses decrease dramatically near the line edge. The x component of the stress (across line width) is somewhat smaller and follows the same trend. The stresses are not completely biaxial in the middle of the lines and become even less biaxial at the line edges. No significant stresses in the z-direction were found.

	Cu	Si	sapphire
A (1/K)	1.65×10^{-5}	2.8×10^{-6}	5×10^{-6}
E (GPa)	110	110	375
ν	0.34	0.27	0.27

Table B1. Material constants used the FEA calculations.

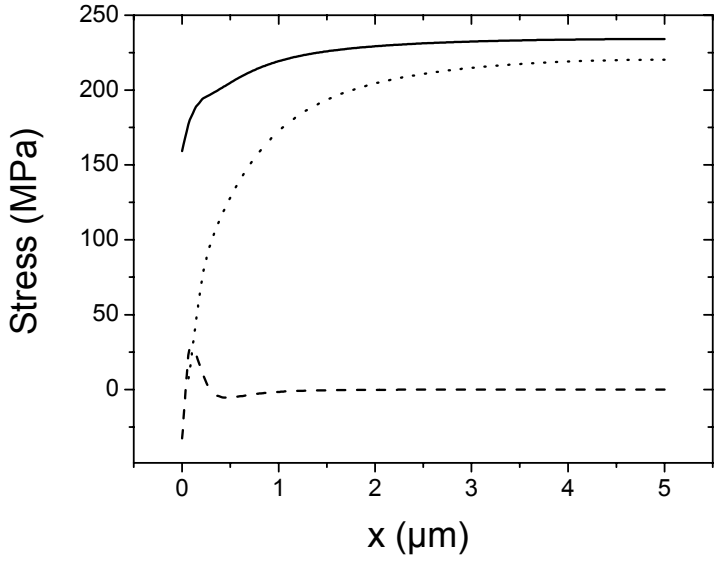

Fig. B.2
Calculated Stresses components in x direction (dotted line), in y direction (solid line) and in z direction (dashed line).

FEA calculations were also performed for Cu lines with the same geometry on sapphire. It was observed, that the stresses were closer to equibiaxial in the Cu lines on sapphire. Presumably, the stress across the line (x-direction) is relaxed to some extent by deformation of the substrate. Since the Youngs modulus of sapphire is higher than that of Si, the sapphire substrate deforms less than Si and the stresses in the Cu line on sapphire are closer to biaxial..

The fact that the stresses in the 10 μm wide and 0.3 μm thick line are not exactly equibiaxial has important consequences on the determination of the glide systems with the maximum resolved shear stress. calculated in Appendix A. The stress state in the line can be viewed as the superposition of an equibiaxial stress and a small uniaxial stress component along the length of the line. For an equibiaxial stress or strain state, the maximum resolved shear stresses depend only on the out-of-plane grain orientation (Appendix A). However, in a metal line, the presence of the small uniaxial component leads to a dependence on the in-plane grain orientation.

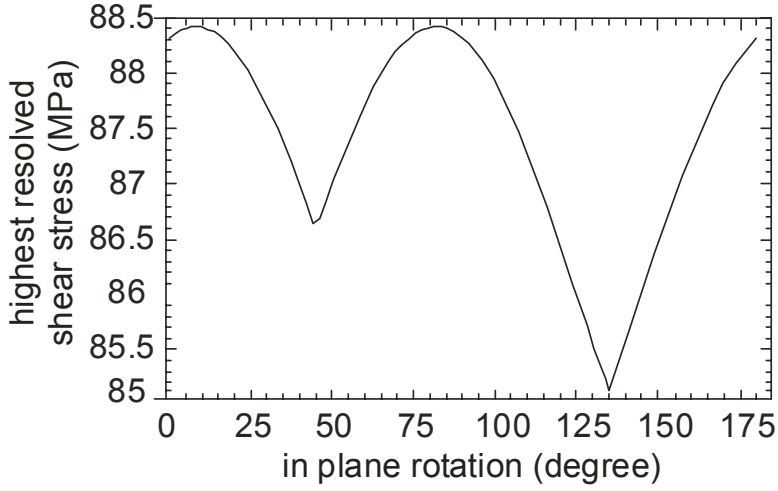

Fig. B.3
The resolved shear stress in a twin of a <100> grain as a function of in-plane grain orientation.

A Mathematica notebook very similar to the one presented in Appendix A has been developed to calculate the effect of a small uniaxial component in an applied biaxial strain state. A strain of 0.105% along x and 0.095% along y was applied and the resolved shear stresses for different grain orientations were calculated. Just as in the case of a pure biaxial strain (Appendix A), the highest resolved stress occurs in <212> out-of-plane oriented crystals (this is the first generation twin orientation of the <100> grains). The variation in stress with the in-plane orientation of a <212> out-of-plane oriented crystal is shown in Fig. B.3. The highest stress is obtained for grains where the <010> direction is rotated +/- 8.2° in-plane relative to the line direction (y-direction).

Appendix C. Plastic Strain during Thermal Fatigue of Cu Films

During thermal fatigue testing, the Cu line and the underlying substrate experience cyclical temperature excursions due to Joule heating. This leads to an imposed *total biaxial strain* range in the line which can be calculated directly from the temperature range. What is not known is the *plastic strain* experienced in the Cu as a function of the applied temperature range.

An estimate of plastic strain experienced in the Cu lines for a given temperature range can be obtained from wafer curvature measurements of the stress versus temperature in Cu films. However, this method is only approximate due to some important differences between the conditions during wafer curvature testing and the thermal fatigue tests:

1) During a fatigue experiment, it is well-known from the behavior of bulk materials, that significant changes in the stress-strain curves occur during the first several hundred cycles. These are mostly attributed to affects of work hardening/softening and racheting effects. Therefore, measurements of initial or early stress-strain curves may either overestimate or underestimate the plastic strain experienced during fatigue. Nonetheless, they can be used to look for trends such as the change in plastic strain with temperature range.
2) Temperature is uniform in the wafer during a wafer curvature experiment but is not uniform during an thermal fatigue test using Joule heating. Estimates of the differences in strain due to this effect are very small.
3) The wafer curvature experiments are performed much more slowly than the thermal fatigue tests. So if strain rate effects are present, this will lead to discrepancies.
4) The wafer curvature experiments are performed on films rather than lines. There will be stress relaxation near the edge of the lines in the thermal fatigue tests. Therefore, the plastic strain will also be somewhat different due to sample geometry effects.
5) Wafer curvature gives only an average stress in the sample. Effects from local variations in stress and local plasticity can only be inferred.

The most serious of these concerns are the first and the last. Based on comparisons with the extent of work hardening in annealed bulk Cu and work softening in work hardened bulk and nanocrystalline Cu, one can expect a change in plastic strain range during a test of roughly a factor of two.

The stress in a thin film as a function of temperature range (ΔT) can be easily measured using wafer curvature measurements. For comparison with the thermal fatigue tests, cycles should be performed between To and To + ΔT (the minimum and maximum temperatures experienced during a thermal fatigue test). For a material that has homogeneous stresses, the plastic strain is easily determined from the "temperature" width of the hysteresis in the stress-temperature curve (this parallels the method used for determining plastic strains from standard stress strain curves). This is illustrated in Fig. C.1. However, this calculation not so simple for the Cu films studied here. A schematic illustration of the stress-temperature behavior of one of the Cu films in shown in Fig. C.1. The Cu films do not exhibit a large hysteresis during temperature cycling for small ΔT although these is evidence of extensive "plastic behavior" in that the curves deviate substantially from the elastic slope. This is presumably because, (1) we are in a *HCF* regime where the applied strains do not lead to macroscopic plasticity, so there is no clear yielding, (2) it is known from other measurements that extremely non-uniform strains are present which lead to non-uniform plasticity in the thin films. Thus it is only possible to estimate the plastic strains from the average response of the film measured with wafer curvature.

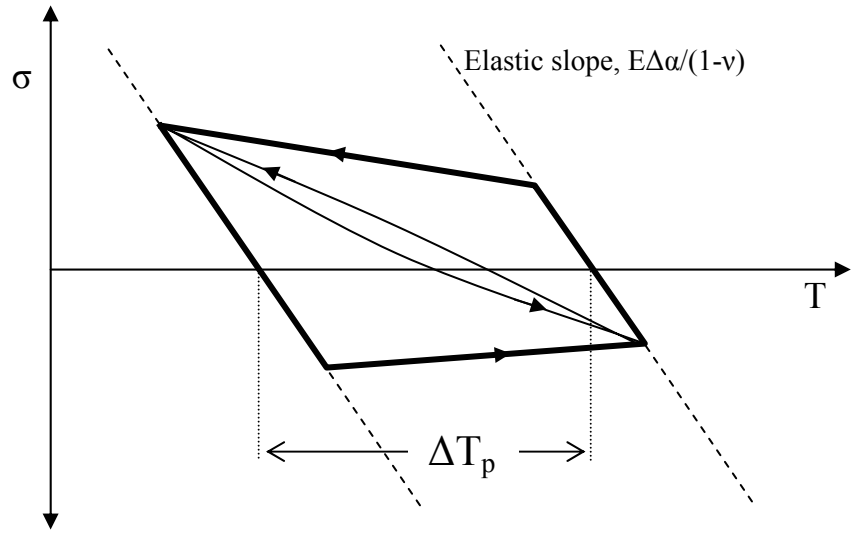

Fig. C.1 Schematic stress-temperature behavior for a Cu films on a substrate. The heavy line shows a perfectly elastic-plastic material. The light line shows behavior representative of the Cu films studied here. EΔα/(1-ν) is the thermal-elastic slope. ΔT_{pl} is a measure of the plastic strain in both materials.

Fig. C.1 shows schematic wafer curvature data. The heavy line shows the behavior of a perfectly elastic-plastic material. By analogy with the definition of plastic strain from isothermal stress-strain curves, ΔT_{pl} is often used as the measure of plastic strain from wafer

curvature data ($\Delta\varepsilon_{pl} = \Delta\alpha\ \Delta T_{pl}$). The light line shows schematic behavior of the Cu films. Assuming the same elastic modulus (same elastic slope) for both samples, one sees that the same plastic strain has been applied to both samples for the case illustrated here. Whether some of the plastic behavior is locally reversed on unloading can not be determined from the wafer curvature data for either sample. It is possible that some of the dislocations that have moved or atoms that make diffusive steps on loading move back on unloading.

This is the method that has been used to estimate plastic strain from wafer curvature data. For ease of caclulation, the equivalent definition $\Delta\varepsilon_{pl} = \Delta\sigma\ (1-\nu) / E$ has been used, where $\Delta\sigma$ is the difference between the stress expected from purely elastic behavior and the measured stress at the maximum temperature. It is certainly the case that the values that are obtained for the plastic strain depend critically on the value of the elastic slope that is used. In this case, a slope has been used that fits the data reasonably well in the low temperature regime and agrees with the theoretical value for a (111) out-of-plane textured polycrystal.

The fact that the thin films have such good fatigue behavior when plotted against the *applied plastic strain* may be because (1) they exhibit more reversible behavior on plastic loading and unloading than other samples or (2) they accumulate plastic strain in such a way during fatigue that it does not lead so quickly to failure. It would of course be interesting to know which it is. But in either case it is still clear evidence of a new length scale effect.

Appendix D.

Determination of the temperature ranges during *in-situ* AC fatigue testing.

------Original notebook can be obtained from author.

The following calculation (Mathematica notebook) was used to determine the temperature ranges experienced in 300 nm thick Cu lines of Si due to Joule heating with alternating currents.

C1. Modules for data interpretation

This section contains modules that will be used later in the book.

```
<< Statistics`NonlinearFit`
```

This Module finds the zeros in a list. Zeros are only counted if they lie at least 100 elements apart from each other and at least 300 elements away from the ends of the array

```
FindZeroinList[lis_] :=
 Module[{ind, zli = {},}, len = Length[lis];
  For[ind = 1, ind < len, ind++,
   If[(Sign[lis[[ind + 1]]] != Sign[lis[[ind]]]) && (ind + 300 < len) &&
     (ind > 300), zli = Flatten[{zli, ind}],]]; zerlis = {zli[[1]]};
  For[ind = 1, ind < Length[zli], ind++,
   If[(Abs[zli[[ind]] - zli[[ind + 1]]] > 100),
    zerlis = Flatten[{zerlis, zli[[ind + 1]]}],]]; zerlis]
```

The signals are periodic and the slope (absolute values) at the zeros will be determined by a linear fit to a region around each zero. All slopes will be averaged

```
FindavSlopeZeros[lis_] :=
 Module[{slps, len, slo, zeros, A, B, x, ZeroVal, spe, i}, slps = {};
  len = Length[FindZeroinList[lis]];
  For[i = 1, i < len + 1, i++,
   ZeroVal = Take[lis, {(FindZeroinList[lis])[[i]] - 300,
      (FindZeroinList[lis])[[i]] + 300}];
   spe =
    A /. First[BestFitParameters /.
       NonlinearRegress[ZeroVal, A * x + B, x, {{A, 1}, {B, 0}},
        MaxIterations → 30, RegressionReport → BestFitParameters]];
   slps = Flatten[{slps, spe}]]; slo = {0}; slo[[1]] = slps[[1]];
  For[i = 1, i < len, i++, If[Sign[slps[[i]]] != Sign[slps[[i + 1]]],
    slo = Flatten[{slo, slps[[i + 1]]}],]];
  VoltMeanslp = Tr[Abs[slo]] / Length[slo]]
```

The maximums in absolute value between the zeros will be averaged by the following module:

```
FindavMax[lis_] := Module[{partlist = {}, Mx, Mxlist = {}, i},
  zeros = FindZeroinList[lis]; len = Length[zeros];
  For[i = 1, i < len, i++, partlist = Take[lis, {zeros[[i]], zeros[[i + 1]]}];
   If[Abs[Max[partlist]] < Abs[Min[partlist]], Mx = Abs[Min[partlist]],
    Mx = Abs[Max[partlist]]]; Mxlist = Flatten[{Mxlist, Mx}]];
  Tr[Mxlist] / (len - 1)]
```

This is the average value of all zeros. The result is related to the phase of a signal.

```
Phaselist[lis_] := Tr[FindZeroinList[lis]] / Length[FindZeroinList[lis]]
```

C2. Measured Data

This section defines data and constants:

The initial resistance "R0" of the line is measured at a temperature "T0". The measured temperature coefficient of the resistivity of the line is "a". The value of the constant resistor for the current measurement is 0.1 Ohm:

```
R0 = 6.22; T0 = 26.8; a = 0.0036;
Resistor = 0.1;
```

Voltage

This module reads files stored by the Tektronix TDS4XX oscilloscope (".dat" file format). The files consist of 2^15 (32768) sequential measurements, each with 16 bit voltage resolution.

```
Readfile[Lis_, File_, From_, To_] :=
 Module[{AF, i, Xv, Yv, c1, c2}, AF = OpenRead[File]; Clear[Lis];
  Lis = Table[0, {To - From - 1}];
  Skip[AF, {Number, Character, Number, Character}, From];
  For[i = 1, i < To - From, i++,
   {Xv, c1, Yv, c2} = Read[AF, {Number, Character, Number, Character}];
   Lis[[i]] = Yv]; Close[AF];]
```

The experiment runs under voltage control and the applied voltage was sinusoidal as can be seen in the plots that follow.

```
Readfile[Volt, "STR6_517mA1.dat", 1000, 25000]
VoltData = ListPlot[Volt, PlotStyle -> {PointSize[0.001], Hue[.6]},
   DisplayFunction → Identity];
```

Current

An oscilloscope cannot measure currents, therefore a shunt "Resistor" was used and the voltage across the resistor was measured.

The following commands read the measured voltage (=Resistor*current) from a file stored by the oscilloscope on the computer.

```
Curr = VoltCurr / Resistor;
CurrData = ListPlot[Curr, PlotStyle -> {PointSize[0.001], Hue[.4]},
    DisplayFunction → Identity];
```

Below are typical plots of voltage (left) in Volt and current (right) in Ampere:

```
Show[GraphicsArray[{VoltData, CurrData}]];
```

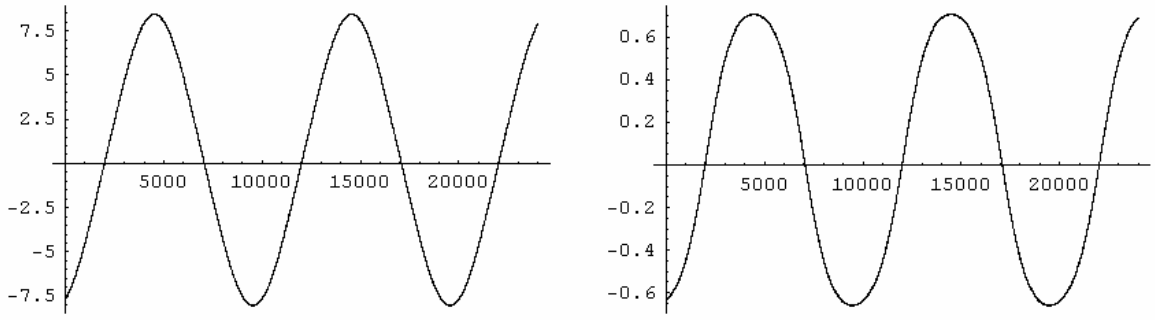

The shape of the current is not sinusoidal, as expected since the experiment runs under voltage control and the temperature in the conductor line varies during a period. The resistance is high when the voltage is high and low when the voltage is low and therefore the current is not proportional to the voltage. This variation will be used to determine the temperature oscillations in the line in the rest of this notebook.

C3. Resistance of the line

Data correction

First, the data needs be corrected for a small DC offset on the measurements:

```
CurrNoDC =
  Curr - ((Max[Curr] - FindavMax[Curr]) - (-Min[Curr] - FindavMax[Curr])) / 2;
VoltNoDC =
  Volt - ((Max[Volt] - FindavMax[Volt]) - (-Min[Volt] - FindavMax[Volt])) / 2;
```

Quite often there is also a small phase difference between the voltage and current signals. The Module "Phaselist" shifts the data in time so that this phase shift is eliminated.

```
Ofst = Round[Phaselist[Curr] - Phaselist[Volt]]
```

```
-3
```

```
Voltnodcnoof = Join[Table[1, {Ofst}], VoltNoDC, Table[1, {-Ofst}]];
Currnodcnoof = Join[Table[1, {-Ofst}], CurrNoDC, Table[1, {Ofst}]];
```

Resistance

Now the resistance can be calculated:

```
Resis = Voltnodcnoof / Currnodcnoof;
```

This is a plot of the Resistance versus the element number, which is proportional to the time.

```
DataRes = ListPlot[Resis, PlotStyle → {PointSize[0.001], Hue[.8]}];
```

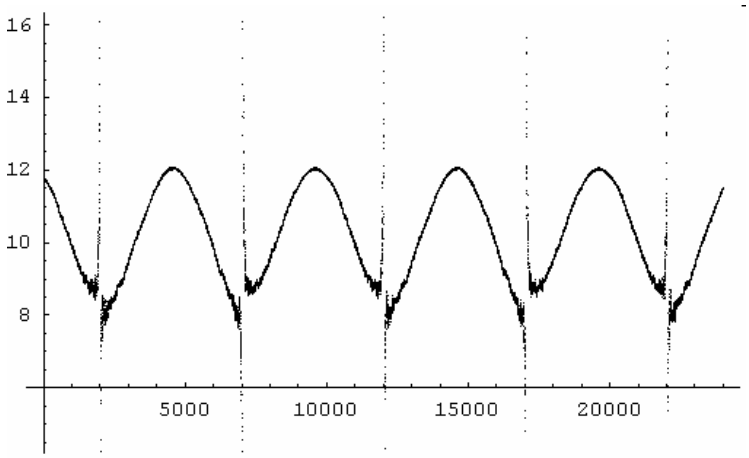

The positions where the voltage and current are zero cause singularities in the resistance.

The maximum resistance during the tests can be easily determined from the amplitudes of voltage and current:

```
Rmax = FindavMax[Volt] / FindavMax[Curr]
```

```
12.0305
```

Determination of the minimum resistance during a cycle is not straight forward, because the voltage and current are zero when the resistance is in its minimum (plot shown above). In order to determine the minimum resistance, the derivatives of the voltage and current curves as they pass through zero can be used. The voltage is a trigonometric function and the derivative is simple to calculate as the voltage passes through zero (Module "FindavSlopeZeros"). The current is not sinusoidal, but as it passes through zero it behaves approximately like a sine function. Deviationsare only observed for higher voltages. If one divides the derivatives of voltage and current, the effect of the frequency cancels out and one obtains the minimum resistance during the temperature cycles (rule from de l'Hospital).

```
Rmin = FindavSlopeZeros[Volt] / FindavSlopeZeros[Curr]
```

```
8.48155
```

C4. The Temperature in the Line

Temperature

This is the temperature dependence of the resistance which was measured before the test:

```
R[t_] := R0 (1 + a * (T[t] - T0));
```

From the resistance, the temperature can be calculated and is plotted below,

```
T := (Resis / R0 - 1) / a + T0
```

```
Tempplot = ListPlot[T, PlotStyle → {PointSize[0.001], Hue[.7]}];
```

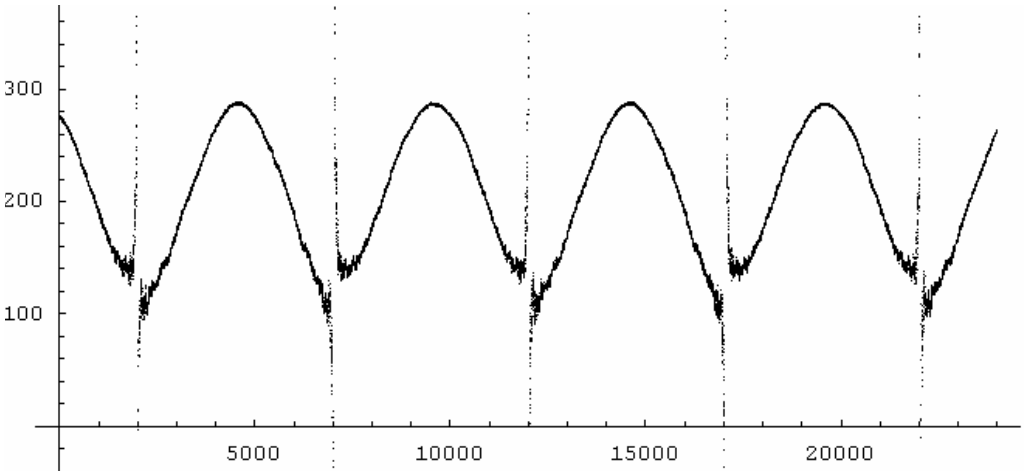

A list with the minimum temperature, the maximum temperature and the temperature amplitude (difference) in the line during the cycles is given here:

```
Temperature = {Temperatmin = (Rmin / R0 - 1) / a + T0,
   Temperatmax = (Rmax / R0 - 1) / a + T0, Temperatmax - Temperatmin}
```

{127.798, 286.29, 158.492}

The temperature depends roughly linearly on the power

Here it will be shown, that the temperature of the line is roughly proportional to the instantaneous electrical power. First a two dimensional list which contains the power and the temperature will be created, then a linear fit is performed and the result is displayed.

```
TempPower =
   Table[{Voltnodcnoof[[n]] * Currnodcnoof[[n]], (Resis[[n]] / R0 - 1) / a + T0},
    {n, Length[Voltnodcnoof]}];
```

```
TPpl = ListPlot[Abs[Select[TempPower, #1[[1]] > .2 &]],
    PlotStyle → PointSize[0.001], DisplayFunction → Identity];
```

```
Param3 = BestFitParameters /.
   NonlinearRegress[Select[TempPower, #1[[1]] > .2 &], A * x + B, x,
    {{A, 80}, {B, 20}}, MaxIterations → 40,
    RegressionReport → BestFitParameters]
```

{A → 26.2619, B → 111.068}

```
TPfitpl = Plot[(A * x + B) /. Param3,
    {x, 0, 1.1 * FindavMax[Volt] * FindavMax[Curr]}, PlotStyle → Hue[.9],
    DisplayFunction → Identity];
```

The following data contains the Temperature of the line (y-axis) and the instantaneous power in the line (V*I) on the x axis.

```
Show[TPpl, TPfitpl, DisplayFunction → $DisplayFunction];
```

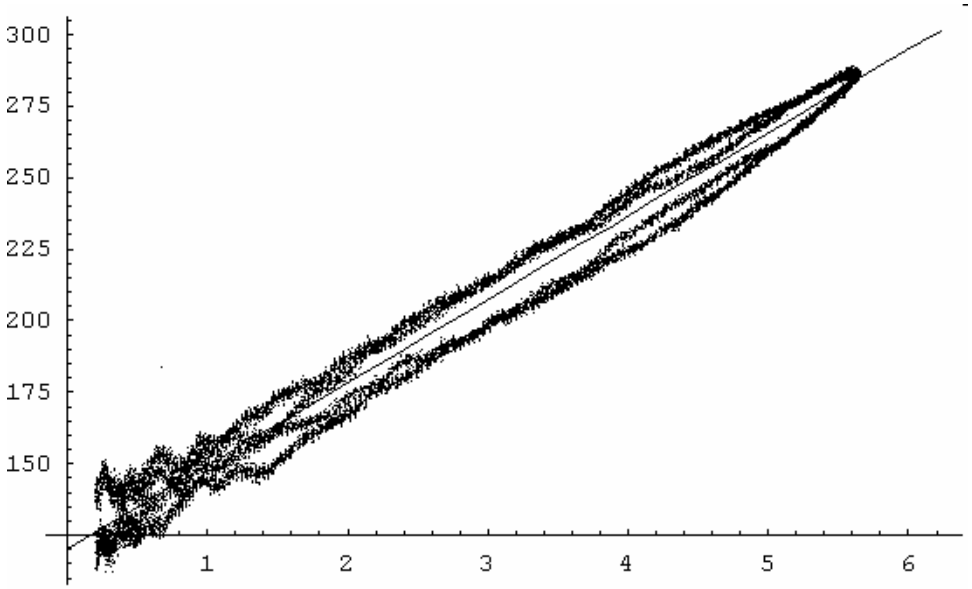

The hysteresis in the plot becomes smaller when the surrounding of the sample is heated sufficiently and less heat is lost in warming up the environment during a cycle. The lower branch corresponds to times when the voltage is increasing, the upper branch to times when the voltage is decreasing.

A list with the minimum temperature, the maximum temperature and the temperature amplitude (difference) in the line during the cycles is given here:

```
Print["Tmin=", Temperature[[1]], "     Tmax=", Temperature[[2]],
  "    Tamplitude=", Temperature[[3]]]
```

```
Tmin=117.926     Tmax=260.927     Tamplitude=143.001
```

C5. An analytical equation to calculate the temperature in the line

```
Clear[R0, T0, a]
```

The applied voltage is sinusoidal:

```
u[t_] := u0 * Sin[2 * Pi * t]
```

And the resistance changes during a cycle according to

```
R[t_] := R0 * (1 + a * (Temper[t] - T0))
```

Under the assumption, that the temperature depends linearly on the instantaneous power (T=A*Power+B with Power=u[t]^2/R; see Section C4 above), a quadratic equation for the dependence of temperature on the voltage can be obtained:

```
Solve[{Temper == A * u[t] ^ 2 / (R0 * (1 + a * (Temper - T0))) + B}, Temper]
```

$$\left\{\left\{\text{Temper} \to \frac{1}{2\,a\,R0}\left(-R0 + a\,B\,R0 + a\,R0\,T0 - \sqrt{(R0 - a\,B\,R0 - a\,R0\,T0)^2 - 4\,a\,R0\,(-B\,R0 + a\,B\,R0\,T0 - A\,u0^2\,\text{Sin}[2\,\pi\,t]^2)}\right)\right\},\right.$$
$$\left.\left\{\text{Temper} \to \frac{1}{2\,a\,R0}\left(-R0 + a\,B\,R0 + a\,R0\,T0 + \sqrt{(R0 - a\,B\,R0 - a\,R0\,T0)^2 - 4\,a\,R0\,(-B\,R0 + a\,B\,R0\,T0 - A\,u0^2\,\text{Sin}[2\,\pi\,t]^2)}\right)\right\}\right\}$$

Only temperatures above absolute zero will be accepted (Solution2):

$$\text{Temper}[t\_] := \frac{1}{2\,a\,R0}\left(-R0 + a\,B\,R0 + a\,R0\,T0 + \sqrt{(R0 - a\,B\,R0 - a\,R0\,T0)^2 - 4\,a\,R0\,(-B\,R0 + a\,B\,R0\,T0 - A\,u0^2\,\text{Sin}[2\,\pi\,t]^2)}\right)$$

Experimental data from above are used in this model:

```
R0 = 6.22; T0 = 26.8; a = 0.00399; u0 = FindavMax[Volt];
```

The frequency and the phase of the experiment are used, therefore the time variable will be changed to t2:

```
t2 = (t - FindZeroinList[Voltnodcnoof][[1]]) /
    (2 * (FindZeroinList[Voltnodcnoof][[1]] -
        FindZeroinList[Voltnodcnoof][[2]]));

Tempfit = Plot[Temper[t2] /. Param3, {t, 0, Length[Voltnodcnoof]},
    PlotStyle → {Thickness[0.003], Hue[1.]}, DisplayFunction → Identity];
```

A comparison of the analytic curve with the experiment gives reasonable agreement:

```
Show[Tempfit, Tempplot, DisplayFunction → $DisplayFunction];
```

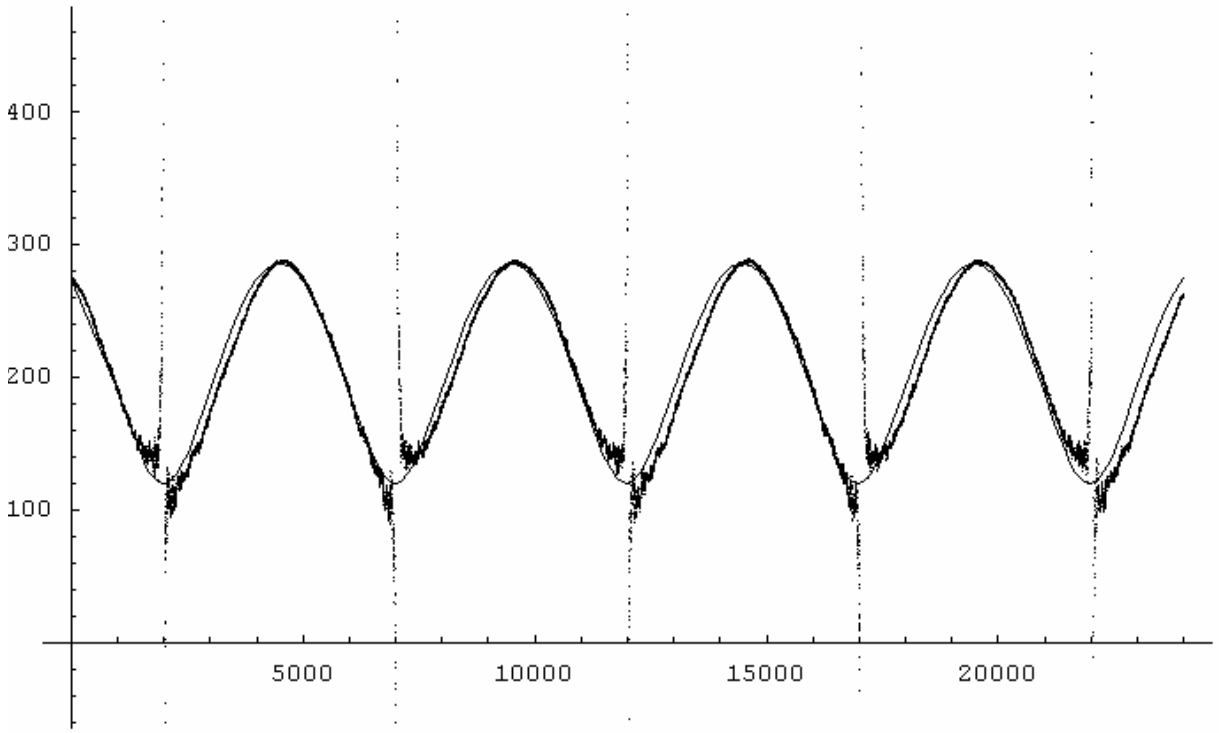

Appendix E. Thermische Ermüdung dünner Kupferschichten

Deutschsprachige Kurzzusammenfassung der Doktorarbeit

Das Verhalten von Materialien unter wechselnden mechanischen Belastungen ist für die Zuverlässigkeit von mikroelektronischen und mikromechanischen Systemen von entscheidender Bedeutung. Obwohl das Phänomen der mechanische Ermüdung in Massivproben bereits intensiv untersucht ist, weiß man bis heute nur wenig über die Ermüdung von Mikromaterialien. Ein Beispiel eines solchen Materials ist die Metallisierung von höchstintegrierten Mikroelektronikbauteilen. Sie besteht aus kleinsten Metallleiterbahnen, deren Breiten und Höhen häufig weniger als ein Mikrometer betragen. Im Betrieb kann sich die Temperatur von Mikroelektronikbauteile um bis zu 100 °C ändern und bedingt durch den großen Unterschied der thermischen Ausdehnungskoeffizienten der Metallleiterbahnen und des darunter liegenden Siliziumsubstrats kommt es damit zu einer Änderung des Dehnungszustands des Metalls. Die grundlegenden Auswirkungen von wiederholten Dehnungs- und Temperaturänderungen auf Kupferleiterbahnen mit kleinen Abmessungen wurden in der vorliegenden Doktorarbeit untersucht. Die aufgebrachten Dehnungszyklen führen zu einer Schädigung, die zwar Gemeinsamkeiten mit der Ermüdungsschädigung von Massivproben hat, aber auch völlig neue Effekte aufweist. Die Widerstandsfähigkeit von Mikromaterialien gegenüber mechanischer Ermüdung ist im Vergleich zu Massivmaterialien erhöht und hängt von deren Schichtdicke und Korngröße ab.

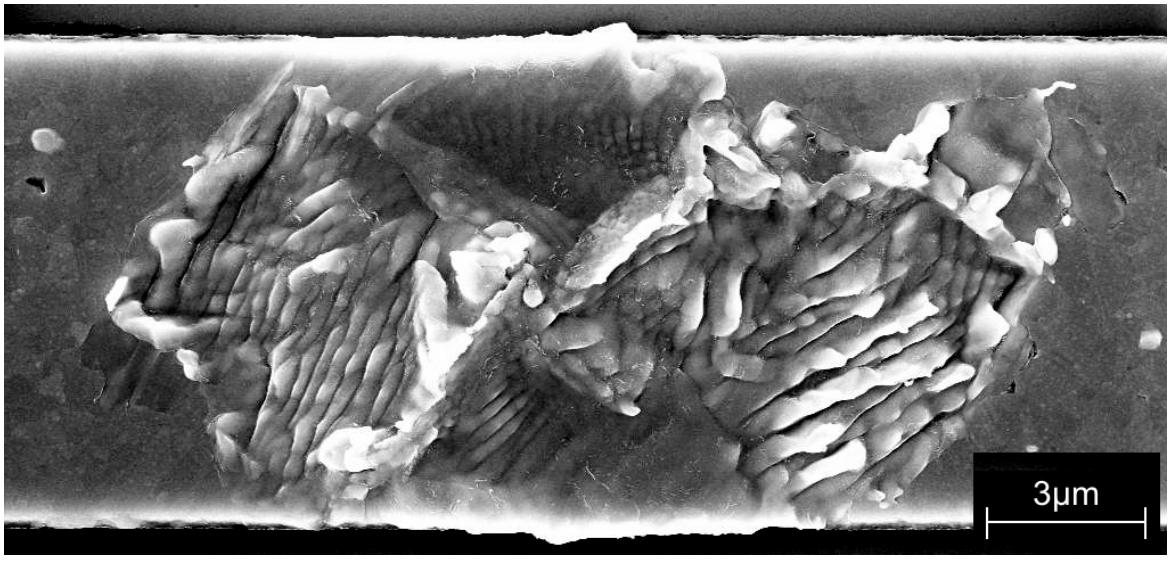

Abbildung 1 Ermüdungsschaden in einer 300nm dicken Cu Leiterbahn auf einem Si Substrat. Die Leiterbahn wurde $7.6x10^5$ mal zwischen 119°C und 305°C bei 200Hz zykliert. Die geschädigten, rechteckigen Körner haben eine <100> Orientierung senkrecht zu der Substratebene.

Eine Methode zur thermischen Ermüdung kleiner Strukturen.

Zu Beginn der Arbeit wurde eine Methode zur Durchführung von thermomechanischen Ermüdungstests an kleinen Kupferstrukturen entwickelt. Zur Einstellung von Temperaturänderungen werden Kupferleiterbahnen mit elektrischem Strom geheizt. Da die Ausdehnungskoeffizienten des dicken Substrats und des dünnen Metallfilms unterschiedlich sind, kommt es während einer Temperaturänderung zu einer Änderung des Dehnungszustands und zu einer Änderung der mechanischen Spannung in den dünnen Kupferleiterbahnen.

Mit Wechselstrom, konnten die Temperatur und Dehnungszyklen kontinuierlich wiederholt und so eine Ermüdungsbeanspruchung aufgebracht werden. Es wurde eine sinusförmige Wechselspannung an die Leiterbahnen angelegt und die eingebrachte periodische Leistung führte zu den gewünschten Temperaturoszillationen in den Leiterbahnen. Die Temperaturoszillationen konnten gemessen werden, denn die mit den Temperaturänderungen verbundenen Widerstandsänderungen während der Zyklen führten zu einer Abweichung des resultierenden Stromsignals von dem sinusförmigen Verlauf der angelegten Spannung (der elektrische Widerstand eines Metalls hängt in guter Näherung linear von der Temperatur ab und diese variierte während der Zyklen). Das Stromsignal wurde gemessen und seine Abweichung von der Sinusform ausgewertet um die Temperatur in den Leiterbahnen zu bestimmen. Abb. E.2 zeigt Strom und Spannung während einer Messung in (a) und die sich daraus ergebenden Widerstands- und Temperaturoszillationen in (b). Der Temperaturbereich einer Schwingung ist definiert als die Differenz zwischen der Minimal- und Maximaltemperatur. Er beträgt in Abb. E.2 ca. 140 K und typische Werte wurden je nach Probe zwischen 120 K und 300 K gewählt. Die Minimaltemperaturen lagen jeweils zwischen 70°C bis 130°C. Da die eingebrachte Leistung auch immer die Probe verlassen muss, ist es

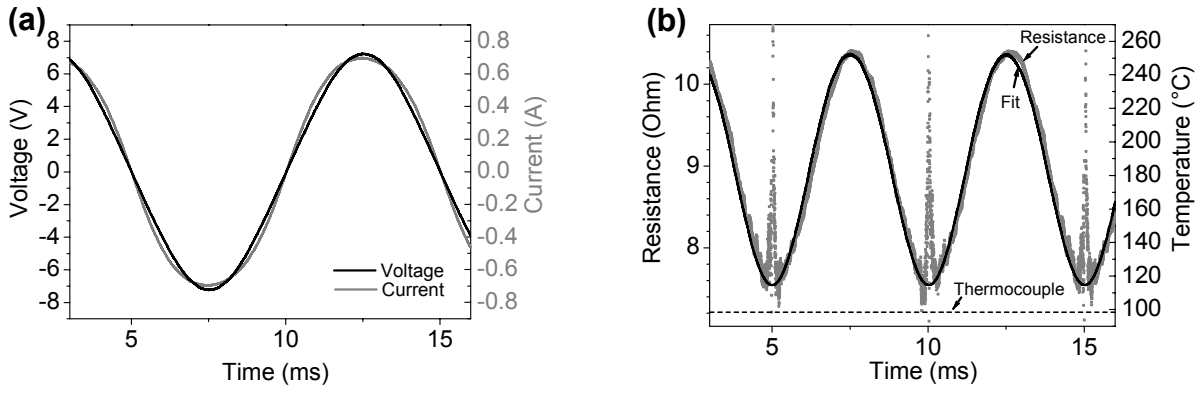

Abbildung E.2 Elektrische Spannung (schwarz) und Strom (grau) in Abhängigkeit der Zeit (a). Elektr. Widerstand (Punkte) und Temperatur bestimmt unter der Annahme, dass Leistung und Temperatur linear voneinander abhängen (Linie) (b). Die Gepunktete Linie gibt die Messwerte eines Thermoelements wieder, dass sich am Rand der Probe befindet.

bei diesem Experiment erforderlich, die Proben mit einem hinreichend gut wärmeleitenden Medium in Kontakt zu bringen, da sonst hohe Minimaltemperaturen auftreten.

Im Vergleich zu herkömmlichen Ermüdungsexperimenten ist die vorgestellte Methode einfach konzipiert und es bedarf statt aufwendiger, präziser mechanischer Bauteile nur elektrischen Stroms, um kontrollierte Temperatur und Dehnungsänderungen aufzubringen. In dieser Arbeit wurden Ermüdungstests innerhalb eines Rasterelektronenmikroskops (REM) durchgeführt. Neben einer Erfassung der Lebensdauern war im REM auch eine Beobachtung der mikroskopischen Vorgänge bei der Ermüdung möglich. Gegenstand dieser Arbeit war die Untersuchung der Ermüdung von Kupferleiterbahnen. Der nächste Abschnitt befasst sich mit ihrer Herstellung und der daraus resultierenden Mikrostruktur.

Die verwendeten Proben

Die verwendeten Kupferleiterbahnen wurden mittels Elektronenstrahllithographie, Abscheidung durch Sputtern und einem nachfolgenden „Lift-off" Schritt hergestellt. Als Substrat kamen einkristalline Si-Wafer mit einer Dicke von 525 µm zum Einsatz. Nach dem Aufbringen eines Photolacks wurde dieser mit Elektronen im REM belichtet und nach seiner Entwicklung besaß der Photolack Lücken an den Stellen, an denen später Leiterbahnen liegen sollten. Nach der Entwicklung wurden zunächst 5 nm Ta und danach 100, 200 oder 300 nm Cu mittels Sputtern im Vakuum bei 10^{-4} Pa abgeschieden. Beim „Lift-off" Schritt, der nach dem Abscheiden der Schicht erfolgte, wurde der unter dem Kupfer liegende Photolack mit Aceton aufgelöst und der Kupferfilm abgehoben. Zurück blieben nur die zuvor in den Lack strukturierten hantelförmigen Bereiche der Teststrukturen. Diese besaßen rechts und links von den Leiterbahnen Flächen zur elektrischen Kontantierung. Die Leiterbahnen selbst waren 800 µm lang und typischerweise zwischen 8 und 10 µm breit. Nach ihrer Herstellung wurden alle Proben 15 Stunden bei 400°C ausgelagert um Kornwachstum und eine Stabilisierung der Mikrostruktur zu erreichen. Aufnahmen mit dem Rasterionenmikroskop (Focused Ion Beam Microscope - FIB) zeigten eine relativ hohe Zwillingsdichte und mittlere Korngrößen von 0.3, 1.0 und 1.5 µm für die 100, 200 bzw. 300 nm dicken Filme. In θ-2θ Röntgenmessungen wurde eine gemischte Fasertextur mit <111> und <100> orientierten Körnern ermittelt.

Neben den Filmen auf Si wurden auch Cu Leiterbahnen auf Saphir hergestellt. Hierzu wurde ein kontinuierlicher, 300 nm dicker Cu film im Ultrahochvakuum (UHV) bei 10^{-8} Pa auf einen Saphirwafer aufgesputtert. Danach wurde dieser mit einem Photolack beschichtet und mit sichtbarem Licht belichtet. Im Gegensatz zu der oben beschriebenen Methode blieb bei diesem Verfahren nach der Entwicklung des Photolacks nur die Geometrie der Strukturen

im Photolack zurück. Sie diente als Ätzmaske bei einem Nassätzvorgang zum Entfernen des nicht benötigten Cu und wurde danach mit Aceton aufgelöst. Die hergestellten Strukturen hatten ähnliche Abmessungen wie die Strukturen auf Si-Wafern, jedoch eine besondere Textur. Es handelte sich um eine sehr scharfe <111> Fasertextur mit zwei Vorzugsorientierungen innerhalb der Filmebene (im Falle eines Bikristalls wären die die Domänen). Anhand einer Polfigur wurde eine Orientierungsunschärfe der beiden Vorzugsrichtungen in der Filmebene von 13° (Volle Breite bei halbem Maximum) ermittelt. In den Proben wurden nur äußerst wenige Zwillinge gefunden, die meisten Körner waren zwillingsfrei.

Entwicklung der Ermüdungsschädigung in 200 und 300 nm dicken Filmen

Nach einiger Zeit unter thermischer Wechselbelastung floss kein elektrischer Strom mehr durch die Leiterbahnen. Es gab dann einen Bereich, in dem Cu und Ta geschmolzen waren. Wie von Ermüdungsexperimenten erwartet, sank die Anzahl von Lastwechseln, die erforderlich war um die Leiterbahnen zum beschriebenen Ausfall zu bringen mit der Erhöhung der Dehnungsamplitude (In den hier vorgestellten thermomechanischen Tests ist die Dehnungsamplitude proportional zur Temperaturamplitude und diese ist gleich der Hälfte des bereits beschriebenen Temperaturbereichs). Nach der Ermüdung zeigten die Proben, wie dies von Massivmaterialien bekannt ist, periodische Extrusionen an ihrer Oberfläche. Sie wurden in einzelnen Bereichen entlang der Leiterbahn gefunden und die Anzahl dieser Bereiche war größer in Tests, die mit höheren Amplituden durchgeführt wurden. Zur besseren Untersuchung der mikroskopischen Vorgänge wurde die Ermüdung *in-situ* im REM beobachtet. Es ergab sich dabei folgendes Bild:

Schädigung tritt zuerst an Korngrenzen und Zwillingen in Form von Extrusionen auf und breitet sich dann weiter ins geschädigte Korn hinein aus. Es gibt wesentliche Unterschiede im Verhalten zwischen <111> und <100> Körnern. Abb. E.3 zeigt die zwei unterschiedlichen Arten der Schädigung. Die rechte untere Schädigung ist typisch für ein <111> Korn. Die Schädigung wird hier von den vorhandenen Zwillingen und Korngrenzen in der anfänglichen Mikrostruktur beeinflusst indem die Schädigung dort anhält. Der geschädigte Bereich weiter links oben entstand in einem <100> Korn. In diesen Körnern können Zwillinge die Schädigung nicht aufhalten. Beobachtungen zu Beginn des <100> Schädigungsvorgangs zeigten, dass sich Wachstumszwillinge auflösen, die Schädigung danach weiter fortschreitet und dabei selbst an Korngrenzen nicht anhält. In Abb. E.3 erkennt

man beim Vergleich eines Rückstreuelektronenbildes vor dem Test Abb. E.3 (a) mit einem Sekundärelektronenbild nach dem Test Abb. E.3 (b), dass Nachbarkörner des <100> Korns ebenfalls geschädigt werden: Das <100> Korn wuchs auf Kosten seiner Nachbarkörner und charakteristisch für die Schädigung in <100> Körnern ist, dass sie in einer facettierten Form auftritt. Wie in Abb. E.1 deutlich zu sehen ist, nehmen die Körner beim ihrem Wachstum häufig eine rechteckige Form an. Die mikroskopischen Untersuchungen ergaben, dass <100> Körner anfälliger für die Schadensbildung sind als <111> Körner und dass geschädigte <100> Körner häufig eine bestimmte Orientierung relativ zur Leiterbahnrichtung haben. Sie sind dabei so orientiert, dass die <010> Richtung um 5 bis 10° gegenüber der Leiterbahnrichtung innerhalb der Filmebene gedreht ist.

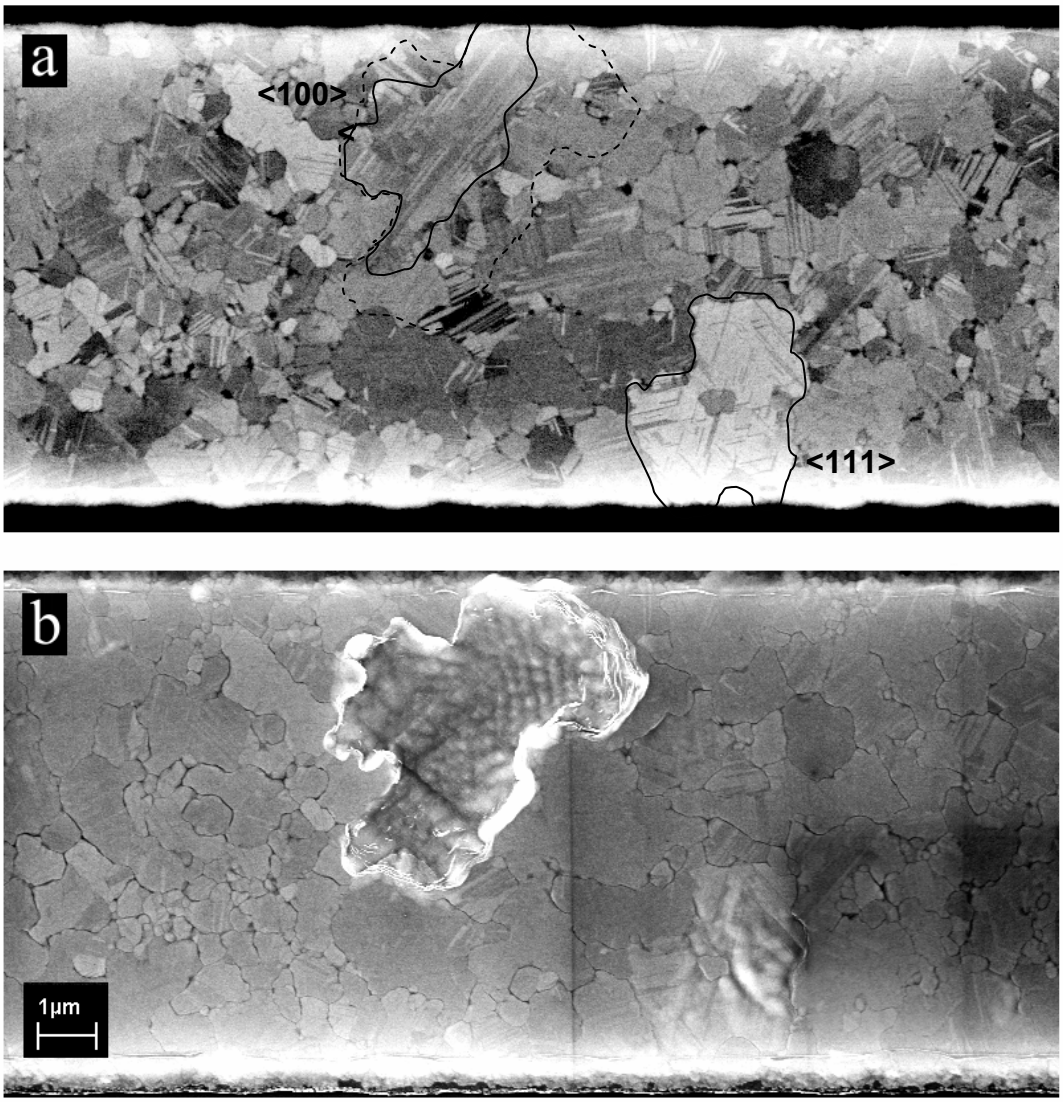

Abbildung E.3 Schadensentwicklung in einem 200 nm dicken Film bei $\Delta T = 220$ °C ($\Delta\varepsilon = 0.31\%$). (a) Rückstreubild bevor dem Test zeigt die Mikrostruktur, (b) Sekundärelektronenbild zeigt die Schädigung nach 3.8×10^5 Zyklen.

Mögliche Ansatzpunkte zum Verständnis der Orientierung der Schäden ergaben Berechnungen des Spannungszustands des Films und der aufgelösten Schubspannungen. Die

höchste Schubspannung auf ein Gleitsystem tritt in einem Zwilling erster Ordnung eines <100> Korns auf. <100> Körner selbst haben nur sehr niedrige Schubspannungen. Die hohe Anfälligkeit der <100> Körner kann so verstanden werden: Schäden sollten sich zuerst in Zwillingen der <100> Körner ausbilden und sich dann weiter in das Korn hinein ausbreiten. Bei Berechnung der aktiven Gleitsysteme in <111> und <100> Körnern sowie deren zugehörigen Zwillingen wurden Hinweise dafür gefunden, dass der Übergang von Versetzungen zwischen Zwilling und Matrix in <100> Körnern relativ einfach möglich ist, wohingegen in <111> Körnern komplizierte Versetzungsreaktionen dazu notwendig sind. Diese Betrachtung könnte erklären warum Zwillinge in <100> Körnern verschwinden und warum die Schädigung an Zwillingsgrenzen im Fall der <111> Körner anhält.

Das Wachstum von <100> Körnern in eine rechteckige Form lässt sich verstehen, indem die Abhängigkeit der Korngrenzenbeweglichkeit von Punktdefekten betrachtet wird. Korngrenzen die aus einem perfekten Versetzungsnetzwerk bestehen haben gegenüber Korngrenzen mit einer hohen Punktdefektdichte eine geringere Beweglichkeit. Die beobachteten Facetten der Körner sind in Richtung <011> auf der Probenoberfläche orientiert. Es scheint daher möglich, dass die Korngrenzen parallel zu <111> Ebenen der geschädigten rechteckigen <100> Körner liegen. Diese Korngrenzen wären dann in den Nachbarkörnern nicht auf kristallographischen Ebenen und ihre Beweglichkeit wäre durch die perfekte <111> Ebene eingeschränkt. Die Bewegung von Versetzungen oder Punktdefekten während der Ermüdung innerhalb des geschädigten Korns hin zu dessen <111> orientierter Korngrenze könnte zu Defekten in dieser und damit zu einer erhöhten Beweglichkeit und zu einem facettierten Wachstum in die rechteckige Form führen.

Ein Ausfall der Leiterbahnen konnte in zwei Fällen im Rasterelektronenmikroskop verfolgt werden. Dabei bildete sich ein Riss in der Probe der innerhalb weniger Minuten die Leiterbahn durchquerte und am Ende der Lebensdauer, wenn nur noch ein Bruchteil des Leiterbahnquerschnitts vorhanden war, zu einer hohen Stromdichte und zum Schmelzen der Leiterbahn führte.

Neben Proben auf Si wurden auch 300 nm dicke Strukturen auf Saphir hergestellt. Diese waren nahezu zwillingsfrei und hatten Korngrößen von mehreren Mikrometern. Einer Schädigung dieser Proben wurde schon bei verhältnismäßig kleinen Dehnungsamplituden erreicht und war nur wenig lokalisiert im Vergleich zu den weniger texturierten Leiterbahnen auf Si. Schäden wurden entlang der ganzen Leiterbahn gefunden und bestanden aus Rillen ähnlich den Rillen von <111> Körnern auf Si. Daneben wurden auch feinere Rillen gefunden.

Eine EBSD Analyse dieser Körner zeigte, dass sie im Gegensatz zu den gröberen Rillen in <110> Richtungen liegen und es sich bei ihnen um Gleitstufen handeln könnte.

Im Vergleich zu dem gerade beschriebenen Ermüdungsverhalten der Proben mit 200 und 300 nm Schichtdicke auf Si oder Saphir zeigten 100 nm dicke Filme ein völlig anderes Verhalten.

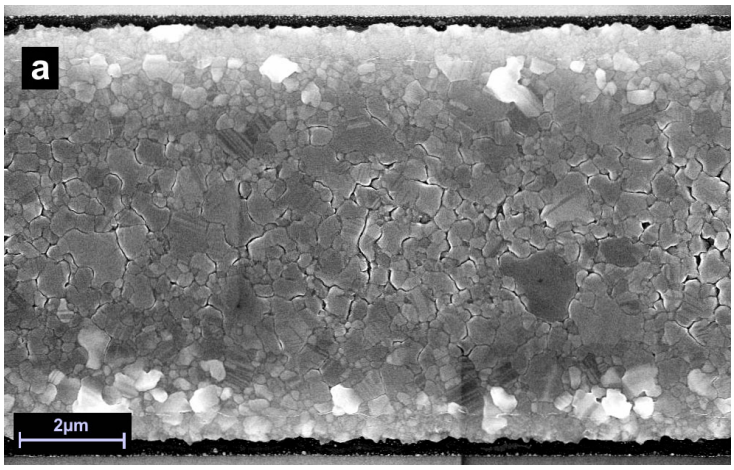

Abbildung E.4
Typische Ermüdungsschädigung in 100 nm dicken Strukturen nach 7.9×10^5 Zyklen bei $\Delta T = 274$ K.

Ermüdete Proben und Lebensdauern im Vergleich

In den 100 nm dicken Cu Strukturen auf Si wurden Oberflächenrillen nur in wenigen Fällen gefunden. Die Tatsache, dass alle der wenigen beobachteten Rillen in überdurchschnittlich großen Körnern lagen ist ein Hinweis dafür, dass neben der Filmdicke auch die Korngröße für das Ermüdungsverhalten entscheidend ist. Abb. E.4 zeigt einen typischen Schaden in einer 100 nm dicken Leiterbahn. Die dünnen Leiterbahnen enthielten nach der Ermüdung Poren in der Leiterbahnmitte sowie Hügel am Rande der Leiterbahn. Die beobachtete Form dieser Schädigung legt nahe, dass es sich um einen diffusionsbasierten Mechanismus und nicht wie bei den 200 und 300 nm dicken Proben um Versetzungsaktivität handelt. Möglicherweise wird die Versetzungsaktivität in den kleinen Körnern der 100 nm dicken Filme stark unterdrückt und es kommt durch Diffusion zu Poren- und Hügelbildung. Verbunden mit dieser andersartigen Schädigung der dünnen Filme wurde auch ihre erhöhte Lebensdauer nachgewiesen. Abb. E.5 zeigt die Lebensdauern verschiedener Proben in Abhängigkeit des Temperatur- bzw. Gesamtdehnungsbereichs. Größenabhängigkeiten sind sofort zu erkennen: Die Cu Proben auf Saphir hatte vergleichsweise große (Korngrößen im Bereich von 2 bis 6 µm) und zwillingsfreie <111> Körner. Sie zeigten Schädigung schon bei kleinen Temperaturamplituden, während die 100 nm dicken Cu Schichten am widerstandsfähigsten gegenüber Schädigung waren. Insgesamt interessant ist die Beobachtung, dass der Prozess der

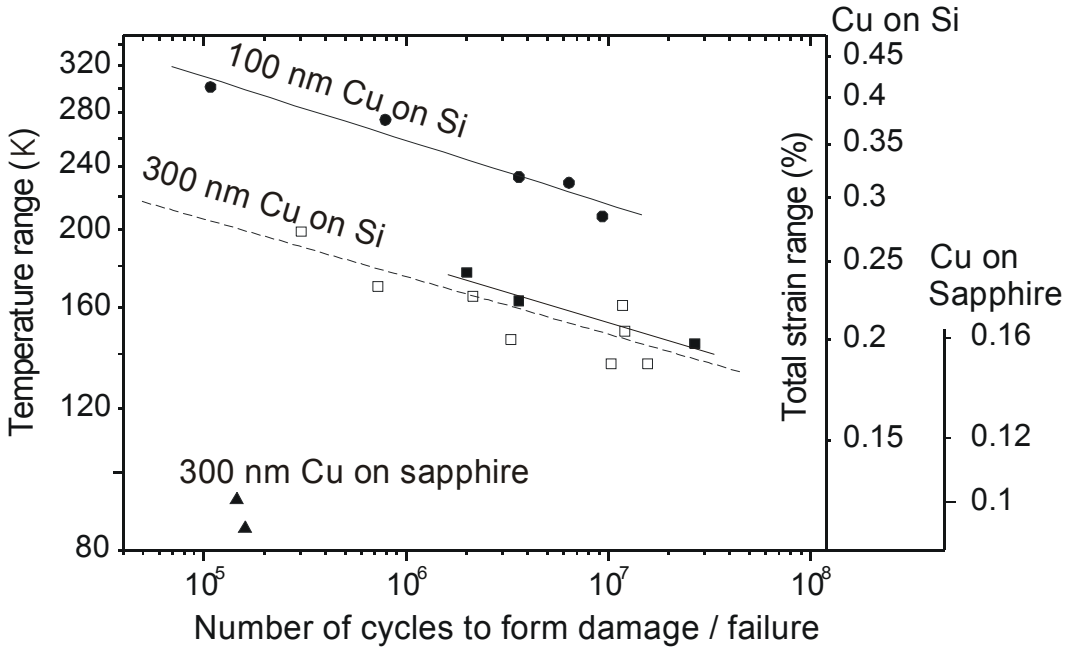

Abbildung E.5 Zyklenzahl bis zum Ausfall (gefüllte Symbole) oder bis zur Bildung schwerwiegender Schädigung (offene Symbole) für die 100 nm dicken Cu auf Si (Kreise), die 300 nm dicken Cu auf Si (Quadrate) und 300 nm dicke Cu auf Saphir (Dreiecke). Temperaturbereich befindet sich auf der linke Achse und Dehnungsbereich auf den rechten Achsen.

Ermüdung in diesen Proben immer noch auftritt obwohl es sich bei den dünneren Filmen dabei um einen völlig anderen Mechanismus als bei den dickeren Proben handelt.

Neben den strukturierten Proben wurden bei jeder Filmherstellung auch immer ganze Cu Filme auf Si produziert. An diesen wurden Substratkrümmungsmessungen durchgeführt und anhand der Ergebnisse die plastische Dehnung während der Oszillationen abgeschätzt. Abb. E.5 zeigt ein Coffin-Manson Diagramm der getesteten Filme. Es enthält weitere Daten von Experimenten von Cu Filmen auf Polyimid Substraten (A) und Daten von Experimenten mit verschiedenen Cu Massivproben (B bis F) mit Korngrößen von 200 nm bis 70 µm (Details über die Datensätze A bis F können in der Arbeit gefunden werden). Anhand Abilldung 5 erkennt man, dass die Lebensdauern der dünnen Filme für eine gegebene plastische Dehnungsamplitude deutlich über den Lebensdauern der anderen Proben liegen. Die hohe Ermüdungsbeständigkeit von feinkörnigen oder klein dimensionierten Proben wurde bisher in der Literatur der hohen Festigkeit dieser Systeme zugeschrieben. Abb. E.5 zeigt jedoch, dass selbst wenn man diese Effekte berücksichtigt und die Daten in Form eines Coffin-Manson Diagramms in Abhängigkeit der plastischen Dehnung aufträgt, immer noch eine erhöhte Zuverlässigkeit von kleinen Strukturen gegenüber Massivmaterial zu finden ist. Hieraus folgt, dass es einen Größeneffekt bei der Verarbeitung von wiederholter plastischer Dehnung in den kleinen Materialien gibt. Kleine Strukturen können bis zu ihrem Ausfall deutlich höhere kumulative plastische Dehnungen aufnehmen als Massivmaterialien. Möglicherweise sind die

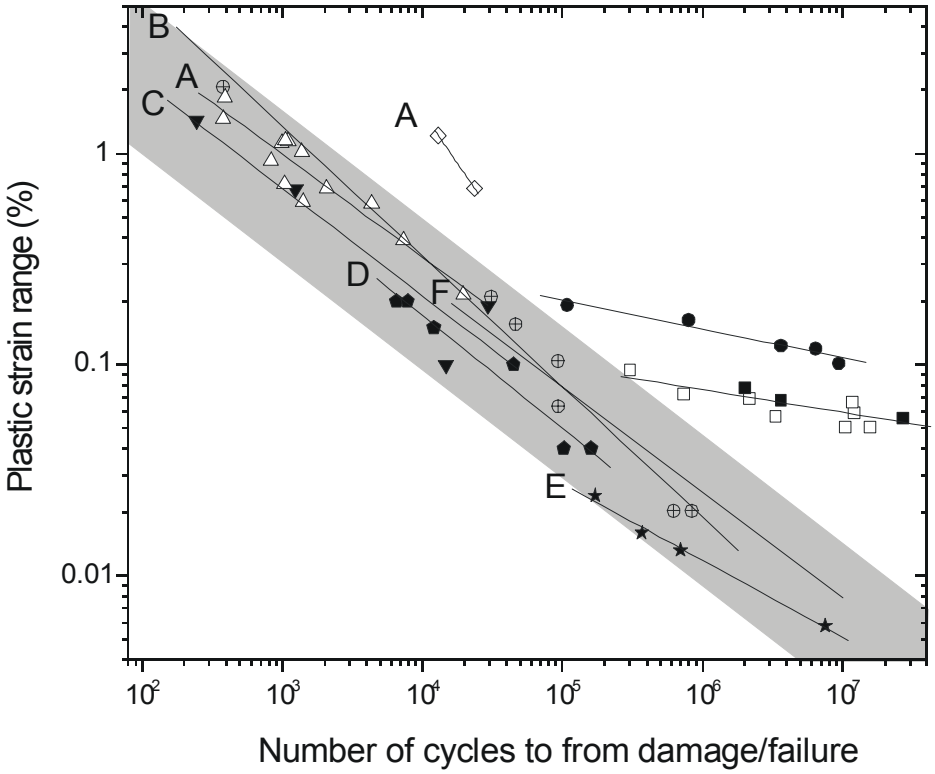

Abbildung E.6 Abhängigkeit des plastischen Dehnungsbereichs auf die Anzahl der Zyklen bis zum Ausfall (zur Schädigung) für die 100 nm dicken Cu auf Si (Kreise), die 300 nm thick Cu auf Si (Quadrate), Cu Schichten auf Kapton (Rauten für 0.4 μm dicke Filme, Dreiecke für alle weiteren Filme) [Kraft] sowie für weitere grob- und feinkörnige Cu Proben. Herkunft der Daten des grauen Bereichs kann aus der Doktorarbeit entnommen werden.

plastischen Veränderungen während einzelner Zyklen zu einem höheren Maße reversibel in den dünneren, feinkörnigeren Filmen.

Mechanische Ermüdung ist ein Effekt der selbst in feinkörnigen (0.3 μm) und dünnen (100 nm) Filmen beobachtet werden kann. Vergleicht man das Verhalten dieser Systeme mit dem von Massivproben, so zeigt sich, dass eine Reduzierung der Abmessungen, wie dies bei kleiner werdender Filmdicke und Korngröße der Fall ist, zu einer Erhöhung der Lebensdauern führt. In diesen dünnen Filmen laufen gegenüber Massivproben unterschiedliche und neuartige Effekte ab. In 200 nm und 300 nm dicken Cu Filmen gibt es einen modifizierten Versetzungsmechanismus, denn bei ihrer Ermüdung werden keine räumlich periodischen Versetzungsstrukturen mehr gebildet. Es kommt jedoch nach wie vor zu einer Schädigung, die der von Massivproben in ihrer Form ähnelt. Bei einer weiterer Reduktion der Abmessungen scheinen Versetzungen bei der Ermüdung keine Rolle mehr zu spielen und 100 nm dicke Schichten zeigen in kleinen Körnern nur diffusionsinduzierte Schäden. Zusammengefasst lässt sich sagen, dass das Phänomen der mechanischen Ermüdung selbst in Metallen mit kleinsten Abmessungen existiert und dass die Ermüdung auf verschiedenen Längenskalen in unterschiedlicher Form auftritt.